PNAS
www.pnas.org

Supplementary Information for
Volatile chemical product emissions enhance ozone and modulate urban chemistry

Matthew M. Coggon, Georgios I. Gkatzelis, Brian C. McDonald, Jessica B. Gilman, Rebecca H. Schwantes, Nader Abuhassan, Kenneth C. Aikin, Mark Arend, Timothy Berkoff, Steven S. Brown, Teresa Campos, Russell R. Dickerson, Guillaume Gronoff, James F. Hurley, Gabriel Isaacman-VanWertz, Abigail R. Koss, Meng Li, Stuart A. McKeen, Fred Moshary, Jeff Peischl, Veronika Pospisilova, Xinrong Ren, Anna Wilson, Yonghua Wu, Michael Trainer, Carsten Warneke

Correspondence: Matthew Coggon
Email: matthew.m.coggon@noaa.gov

This PDF file includes:

Supplemental Methods

1. Ground site and mobile laboratory description

Figure S1A shows the locations sampled by the NOAA mobile laboratory (red trace) as well as the ground site located at the City College of New York (CCNY) during US sampling. In addition to sampling in the NYC metropolitan area, the mobile laboratory was driven through Denver, CO, Chicago, IL, and Pittsburgh, PA to sample urban emissions of VCPs and mobile sources.

Figure S2 shows the drive track of the Tofwerk mobile laboratory from Thun, Switzerland to Trecin, Slovakia. Urban regions sampled by the mobile laboratory with population density > 2000 people km^{-2} are shown.

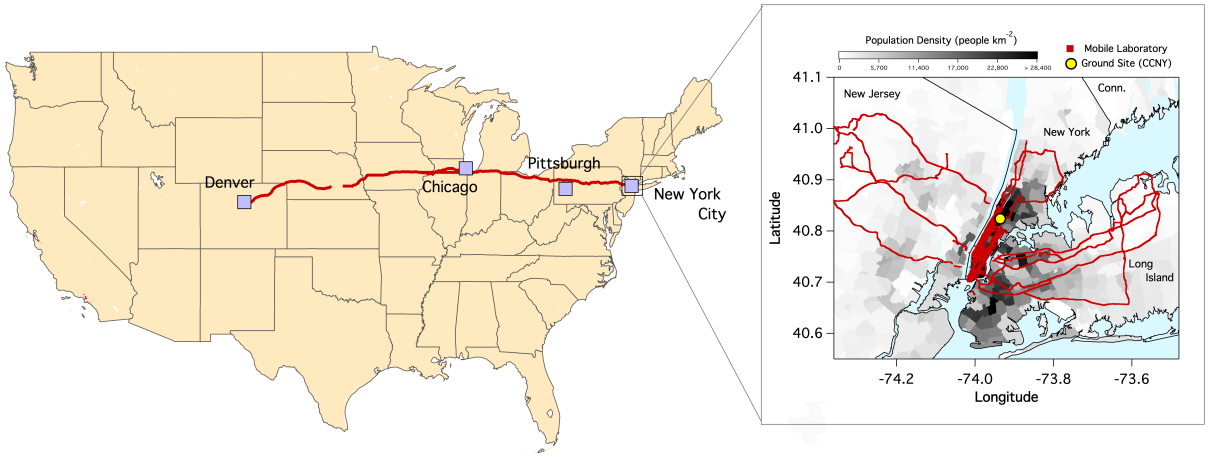

Fig. S1. NOAA mobile laboratory drive track across the U.S. with details showing sampling in New York City. The inset shows the location of the ground site at the City College of New York (CCNY) and a map illustrating the regions of high and low population density.

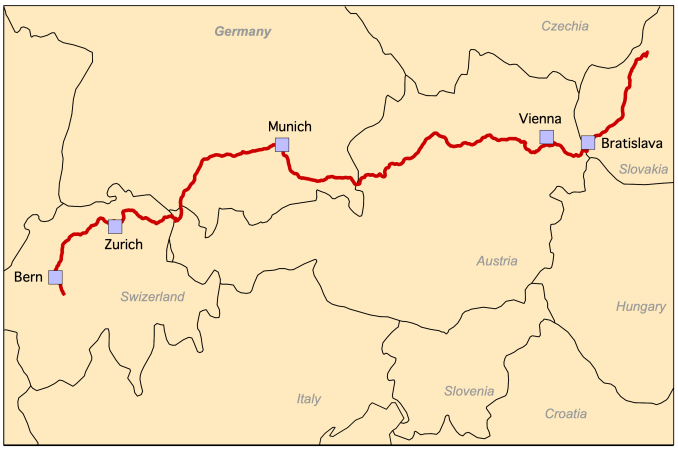

Fig. S2. Tofwerk mobile laboratory drive track across Europe. Urban regions (pop. density > 2000 people km^{-2}) sampled by the mobile laboratory are shown.

2. Instrument sensitivities and intercomparisons

Table S1 summarizes the measured sensitivities, limits of detection, and precision of the NOAA gas-chromatography mass spectrometer (GC-MS), NOAA proton transfer reaction time-of-flight mass spectrometer (PTR-ToF-MS), and Tofwerk PTR-ToF-MS for key measured species. The PTR-ToF-MS measures major monoterpenes (limonene, α-pinene, and β-pinene) with similar sensitivities; consequently, PTR-ToF-MS measurement of total monoterpenes is not dependent on the specific monoterpene distribution. The NOAA PTR-ToF-MS sensitivities are reported based on ion counts normalized to the reagent ion at *m/z* 19 (normalized counts per second, ncps). For species that were not directly calibrated, we estimate sensitivities for the NOAA PTR-ToF-MS following the methods described Sekimoto et al. (1). The Tofwerk PTR-ToF-MS uses a Vocus drift tube, which is tuned to reduce the transmission of ions with m*/z* < 45; consequently, sensitivities are reported based on counts per second.

The GC-MS has well-described, non-linear sensitivities that are specific to each compound for which it is calibrated. The sensitivities are for the selected ion measured (SIM) mass to charge ratio (m/z) at a nominal response of 10 normalized counts. The methods for determining precision and limits of detection (LOD) are described in Lerner et al. (2) and have been updated here using calibrations conducted in summer 2018.

Table S1. Instrument sensitivities, precision, and limit of detection for gas-species reported here.

	NOAA PTR-ToF-MS		**WAS-GC-MS**		**Tofwerk PTR-ToF-MS**	
Species	**Sensitivity (ncps/ppbv)**	**LOD‡ (pptv)**	***at 10 ncts (ncts/ppb)***	**LOD (pptv)**	**Sensitivity (cps/ppbv)**	**LOD (pptv)**
α-pinene	*27 ± 4*	*7*	80 ± 15	0.5	1240	30
β-pinene	*27 ± 4*	*7*	73 ± 8	9	-	-
limonene	*25 ± 3*	*6*	38 ± 6	6	-	-
benzene	*50 ± 7*	*10*	140 ± 20	0.8	2934	50
toluene	*58 ± 8*	*10*	133 ± 12	1.4	-	-
ethanol	*1.35 ± 0.56*	*150*	-	-	-	-
D5-siloxane	*28 ± 3*	*5*	-	-	1800	30
PCBTF	*69 ± 7*	*5*	-	-	-	-

‡ Calculated as the signal + 3 times S/N ratio during background measurements. LOD for NOAA PTR-ToF-MS reported for 30 s measurements during ground site measurements. LOD for Tofwerk PTR-ToF-MS reported for 1 s measurements during mobile sampling

Figure S3 compares WAS-GC-MS measurements of the monoterpene sum (limonene, α -pinene, β-pinene, and lesser abundant monoterpenes), benzene, toluene, and C8 aromatics (ethylbenzene, o-, m-, and p-xylene) with the average NOAA PTR-ToF-MS signal measured during canister filling. For the VOC measurements described in this work, the measured mixing ratios agree to within 10-20% and no significant differences are observed between the two

seasons. Figure S4 shows comparisons of two additional VCP tracers - parachlorobenzotriflouride (PCBTF) and p-dichlorobenzene. The GC-MS was not calibrated for these species and comparisons are shown as normalized counts per second. The two instruments agree with an R^2 of 0.97 for PCBTF and 0.88 for p-dichlorobenzene.

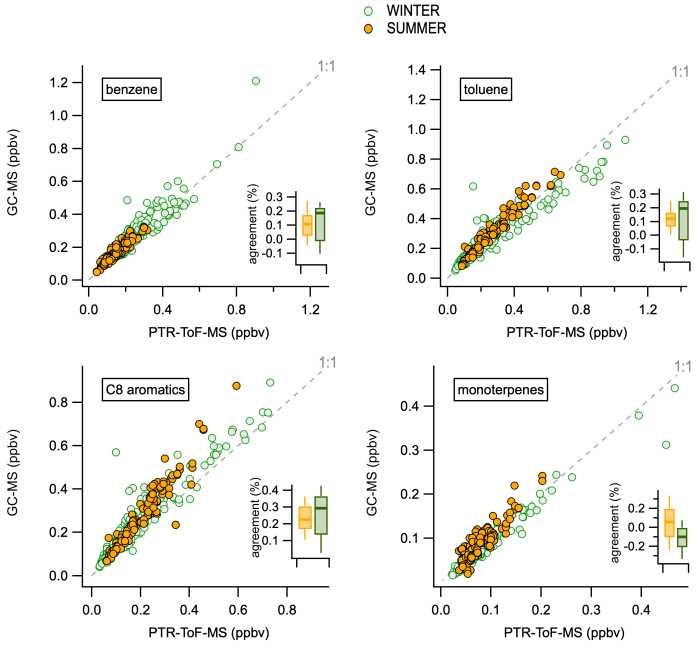

Fig. S3. Inter-comparison of NOAA PTR-ToF-MS and WAS-GC-MS for benzene, toluene, C8 aromatics, and the sum of monoterpenes. Box and whiskers indicate the % difference between the instruments for summer (orange) and winter (green)

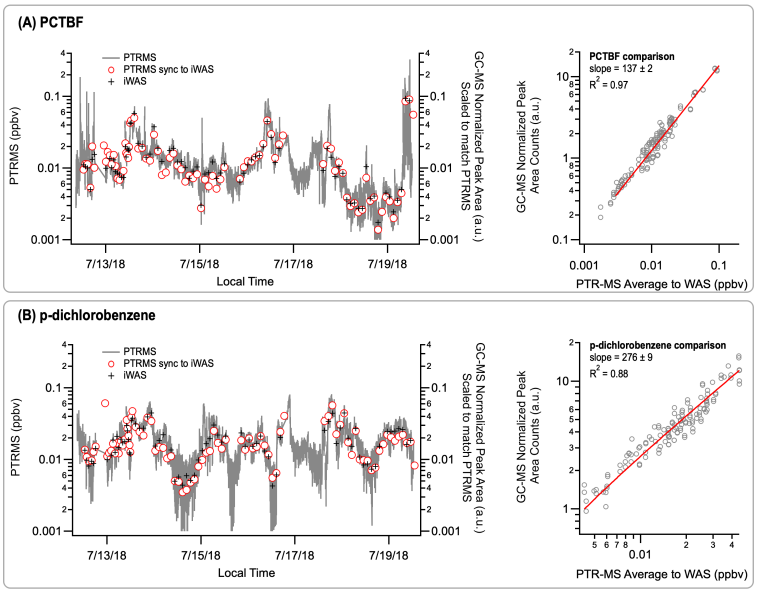

Fig. S4. Intercomparison of NOAA PTR-ToF-MS and WAS-GC-MS for PCBTF and p-dichlorobenzene. GC-MS data are reported as normalized counts because a calibration standard for these two species was not available for this study. The estimated sensitivities of 137 ± 2 and 276 ± 9 are consistent with the sensitivities of calibrated species shown in Table S1.

Other VOCs measured by NOAA PTR-ToF-MS are used to evaluate the bottom-up inventory described in Section 3. Included in this comparison are measurements of common solvents, such as acetone and ethanol, PCBTF from solvent-based coating emissions, p-dichlorobenzene from pesticides, D5-siloxane from personal care products, and D4-siloxane from adhesives and other industrial uses. Alkane measurements from WAS-GC are also compared to constrain inventory sources described in Section 3, which includes both mobile sources and VCPs.

3. Bottom-up anthropogenic emissions inventory and comparison with ambient VOC/CO ratios

For the ozone modeling conducted in this study, we estimate VOC emissions from mobile sources, VCPs, and fugitive leaks from pipeline infrastructure as described below. The emissions are estimated for both winter and summer, though there is little apparent seasonality. The emissions are then evaluated with field measurements of VOC/CO mixing ratios measured at the CCNY ground site located in upper Manhattan. In the following discussion, we describe the VOC/CO measurements conducted at CCNY, describe the development of a bottom-up emission inventory for NYC, then compare the inventory to the observations for NYC.

3.1 Ambient VOC/CO measurements during winter

During the first two weeks sampling period in March, 2018, three winter storms impacted the New York City region. During this period, strong winds transported clean air from the northwest of the CCNY campus. In the last week of the field campaign, stagnant conditions trapped air masses in Manhattan, as evident by rising enhancements in CO and VOCs, such as monoterpenes (Fig. S5). We estimate VOC/CO ratios during the stagnation period (from 3/25 to 3/29), and the ratios are listed in Table S2. We utilize measurements from all hours during the episode, assuming that photochemistry is limited, and that measurements in Manhattan reflect emission ratios. We also estimate VOC/CO ratios for alkanes, cycloalkanes, alkenes, aromatics, and monoterpenes using WAS-GC-MS measurements. During the stagnant pollution period, ~70 canister samples were collected. Species are calculated as an emission ratio if the VOC and CO mixing ratios correlated with $R^2 > 0.30$. Using the NOAA PTR-ToF-MS, we estimate VOC/CO ratios of oxygenates, C9 aromatics, and VCP tracers including D4-siloxane, D5-siloxane, parachlorobenzotriflouride, and p-dichlorobenzene. We first average the high time-resolution measurements of VOCs from the NOAA PTR-ToF-MS and CO to 15 minutes, and then regress the slope during the stagnant pollution period.

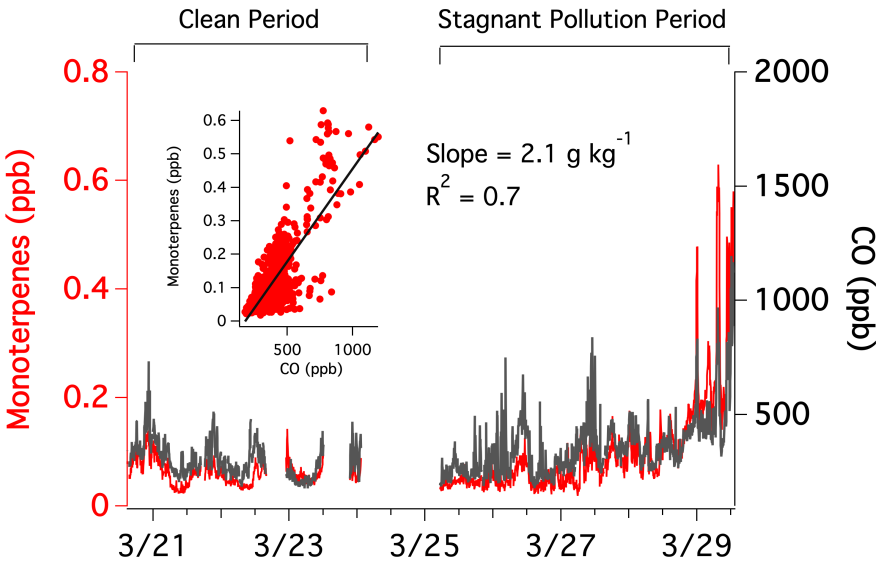

Fig. S5. Time series of monoterpene and carbon monoxide mixing ratios during wintertime measurements. The clean period was affected by a series of winter storms, which were followed by a period of stagnant weather leading to an accumulation of pollutants. The scatter plot inset shows correlations between monoterpene and CO mixing ratios during the stagnation period.

For most species, measured wintertime VOC/CO ratios reported in Table S2 were unaffected by atmospheric chemistry. One exception are the monoterpenes, which are highly reactive towards ozone and the OH radical. During winter 2018, day-time ozone concentrations at CCNY ranged between 10-20 ppb. Figure S6A shows the evolution of limonene under wintertime atmospheric conditions. This simulation was conducted using the Lagrangian box model described in Section 5. In this simulation, ozone is initialized to 20 ppb, background ozone concentrations are set to 20 ppb, biogenic emissions of isoprene are turned off, photolysis rate constants are lower by a factor of 3 from summertime values, and the temperature is held constant at 0ºC. All other meteorological parameters are the same as those described in Section 5. In this simulation, peak OH concentrations are ~1 x 10^6 molecules cm^{-3}, which is an order of magnitude lower than for summertime simulations.

Even under wintertime conditions, over 50% of limonene reacts away within 0.5 hr of emission (Fig. S6). Shown for comparison are the modeled profiles for hydrocarbons (HC8) and small aromatics (TOL). Panel (B) shows the evolution of the same species, but during summertime conditions to highlight seasonal differences. The monoterpene emissions were determined during a stagnation period when wind speeds in NYC were < 5 m s^{-1}. Under these conditions, the air exchange rate over the city amounts to 1.5 - 2 hr^{-1}, and measured monoterpene mixing ratios may have been underestimated by 50%. The monoterpene/CO ratio reported in Table S2 reflects the measured ratio (2.1 g kg^{-1}) adjusted for a 50% loss.

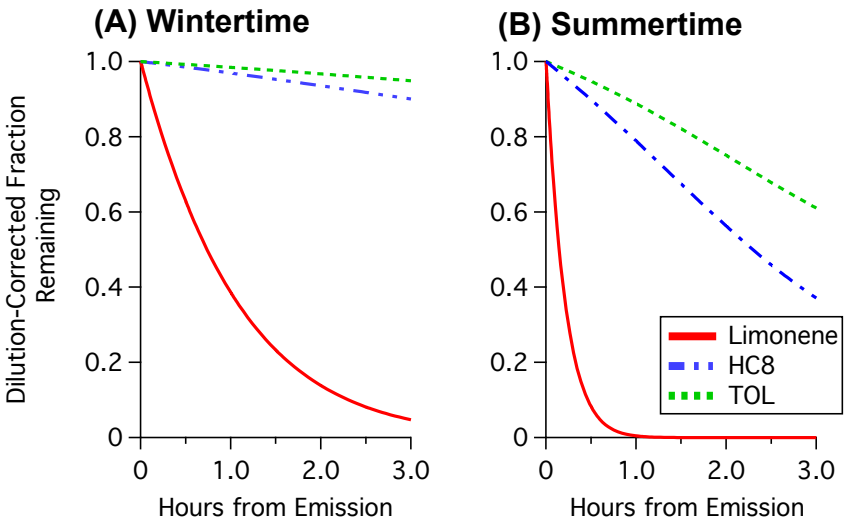

Fig. S6. Evolution of limonene, hydrocarbons (HC8), and aromatic species (TOL) under (A) wintertime and (B) summertime oxidation conditions. Shown is the evolution of the dilution-corrected measurements, normalized to the initial concentrations at time = 0.

3.2 Ambient VOC/CO measurements during summer

One week of ground site sampling was conducted during the three-week sampling period in July, 2018 (7/13 – 7/18). We calculate VOC/CO ratios for the NOAA PTR-ToF-MS and WAS-GC-MS (~50 canisters) in the same manner as for winter (Table S2). Unlike winter, we limit ambient VOC/CO ratios to nighttime hours following Borbon et al. (3) in order to exclude the effects of chemistry (which are greater during summer) on the apparent VOC/CO ratios. In general, the correlations of VOCs with CO were lower in the summer, likely reflecting influence of atmospheric chemistry. A strong seasonal pattern in VOC/CO ratios is not observed, and most measurements agree to within ~10% between winter and summer.

Table S2. Summary of VOC/CO enhancement ratios measured at the CCNY ground site.

VOC Species (WAS-GC-MS)	**Winter VOC/CO** (g/kg)	**Summer VOC/CO** (g/kg)	**VOC Species** (NOAA PTR-ToF-MS)	**Winter VOC/CO** (g/kg)	**Summer VOC/CO** (g/kg)
ethane	23	24	ethanol	53	89
propane	16	14	acetone	8.3	25
n-butane	18	13	methyl ethyl ketone	2.0	5.2
2-methylpropane	9.5	9.3	D4-siloxane	0.73	0.47
n-pentane	9.3	**	D5-siloxane	2.6	1.9
2-methylbutane	14	**	PCBTF	0.97	**
n-hexane	3.7	3.3	p-dichlorobenzene	0.53	**
2-methylpentane	2.5	**	monoterpenes	4.2[a]	**
3-methylpentane	2.5	**			

n-heptane	1.7	1.6			
n-octane	1.2	1.3			
2,2,4-trimethylpentane	2.5	**			
n-nonane	1.6	1.8			
n-decane	1.9	2.2			
methylcyclopentane	1.6	**			
cyclohexane	1.5	**			
methylcyclohexane	1.9	**			
ethene	18	7.9			
propene	3.3	2.0			
1-butene	0.5	0.48			
cis/trans-2-butene	0.64	**			
1,3-butadiene	0.41	0.27			
3-methyl-1-butene	0.14	**			
benzene	3.2	2.7			
toluene	6.3	5.6			
C8 aromatics	9.1	7.2			
C9 aromatics	2.7	3.2			

** VOC/CO has an R^2 less than 0.30.

a. Accounts for estimated ~50% chemical loss rate based on Fig. S6

3.3 FIVE-VCP inventory description

Mobile sources comprise both on-road and off-road gasoline and diesel engines. We estimate nitrogen oxides (NO_x) and CO emissions utilizing the Fuel-based Inventory of Vehicle Emissions, or FIVE (4-6). Briefly, on-road gasoline and diesel fuel sales are reported by state each year (7). Similarly, off-road gasoline (8) and diesel (9) fuel sales are reported by state each year. The most recent reports of mobile source fuels are for 2017, and projected to 2018 based on refinery fuel sales volumes (10, 11). To estimate tailpipe emissions from on-road vehicles, we utilize NO_x and CO emission factors (in g/kg fuel) estimated from tunnel and near-road remote sensing studies described by McDonald et al. (6). The regression analysis is updated to include more recent studies that occurred from 2015-18 for both light-duty (12-14) and heavy-duty (15, 16) vehicles. Cold-start emissions are accounted for by utilizing the EPA MOVES model (17). Tailpipe and non-tailpipe emissions of VOCs are estimated by ratio to CO (5, 18). Off-road gasoline emission factors are based on laboratory testing (19, 20) and remote sensing of recreational boats (21). Off-road diesel emission factors are from the EPA NONROAD model (22). For three-dimensional chemical transport modeling, mobile source emissions are spatially- and temporally-allocated according to the NEI 2014 (23). Seasonal adjustment factors are taken into account between winter and summer. In winter, cold-start emissions from on-road gasoline vehicles are higher (17), but evaporative gasoline emissions lower (24). A summary of mobile source fuel use and emission factors are provided in Table S3 for Manhattan.

Table S3. Summary of fuel use, emission factors, and VOC emissions for mobile source engines in Manhattan, NY during the NY-ICE/LISTOS 2018 field measurements.

Source Category	Fuel Use (t/d)	NO_x EF (g/kg)	CO EF (g/kg)	VOC EF (g/kg)	VOC Emis (t/d)
On-road Gasoline					
tailpipe (winter)	1310 ± 90	2.7 ± 0.4[a]	19 ± 2[a]	1.6 ± 0.2[e]	2.1 ± 0.3
non-tailpipe (winter)	1310 ± 90	--	--	0.88 ± 0.46[f]	0.6 ± 0.3
tailpipe (summer)	1310 ± 90	2.5 ± 0.4[a]	13 ± 1[a]	1.1 ± 0.1[e]	1.4 ± 0.3
non-tailpipe (summer)	1310 ± 90	--	--	1.1 ± 0.6[f]	1.4 ± 0.7
On-road Diesel	740 ± 70	14 ± 2[b]	4 ± 2[b]	0.58 ± 0.29[g]	0.4 ± 0.2
Off-road Gasoline	360 ± 180	16 ± 4[c]	470 ± 80[c]	60 ± 40[c]	21 ± 18
Off-road Diesel	120 ± 10	22 ± 7[d]	11 ± 5[d]	1.8 ± 1.0[d]	0.2 ± 0.1

a. Light-duty gasoline vehicle running exhaust emission factor estimated by regression analysis of tunnel and near-road remote sensing studies, updated from McDonald et al. (6). Scaled to include cold start emissions based on EPA MOVES model (17).
b. Heavy-duty diesel vehicle running exhaust emission factor estimated by regression analysis of tunnel and near-road remote sensing studies, updated from McDonald et al. (6).
c. Based on emission factor testing of two- and four-stroke gasoline engines (19, 20) and recreational boats (21).
d. From EPA NONROAD model (22).
e. Tailpipe VOC EF estimated by ratio to CO from McDonald et al. (18).
f. Tailpipe vs. non-tailpipe VOC EF determined to be 50/50 split in summer based on literature values (24-26) and EPA MOVES model (17). In winter, tailpipe vs. non-tailpipe VOC EF estimated to be 65/35 split based on Rubin et al. (24) and ambient temperature differences between winter and summer in New York City.
g. Tailpipe VOC EF estimate by ratio to CO from Yanowitz et al. (27).

VCP emissions are estimated following McDonald et al. (28). Briefly, a mass balance of the petrochemical industry was performed for the year 2012 where per capita use of coatings, inks, adhesives, personal care products, cleaning agents, and pesticides was estimated. We assume consumer usage of VCPs has not changed significantly between 2012 and 2018. Emission factors were based on a review of indoor air quality literature (28). The only emission factors that have been adjusted here are for architectural/industrial coatings and consumer/industrial adhesives to account for more stringent regulations in New York State relative to federal standards (29), and to account for increasingly stringent VOC standards implemented between 2012 and 2018. Most VCP emissions are found in the area source inventory, with a small fraction of industrial VCP emissions in the point source inventory. For area source VCPs, we allocate emissions spatially according to population density, which is consistent with our mobile laboratory measurements. Point source VCPs are allocated to facilities geo-located in the NEI 2014 (23). We do not account for seasonality in VCP emissions, since seasonality is not evident in our VOC/CO measurements

at the CCNY ground site (Table S2). For diurnal patterns, we utilize those reported by Coggon et al. (30) for personal care products and the NEI 2014 for other VCPs. A summary of VCP use and emission factors are provided in Table S4 for Manhattan.

Table S4. Summary of VCP use, emission factors, and VOC emissions in Manhattan.

Source Category	Use (g/person/d)	VOC EF[c] (mg/g)	VOC Emis[g] (t/d)
Coatings			
Architectural	21 ± 3	270 ± 90[d,e]	9.7 ± 3.5
Industrial	7.8 ± 1.2[a]	250 ± 80[d,e]	3.2 ± 1.1
Printing Inks	1.4 ± 0.5[a]	67 ± 31	0.2 ± 0.1
Adhesives			
Consumer	11.6 ± 5.5	250 ± 140[f]	4.8 ± 3.5
Industrial	8.3 ± 3.9[a]	370 ± 200[f]	5.1 ± 3.7
Personal Care			
Hair Care	6.1 ± 2.9	310 ± 260	3.1 ± 3.1
Perfumes	2.5 ± 1.2	490 ± 270	2.0 ± 1.5
Lotions	6.1 ± 2.9	540 ± 290	5.5 ± 3.9
Other Cosmetics	11.4 ± 5.3	420 ± 250	8.0 ± 6.0
Cleaning Agents			
Surface Cleaners	35 ± 16	78 ± 75	4.6 ± 4.6
Dishwashing	50 ± 22	8.5 ± 4.6	0.71 ± 0.49
Laundry	64 ± 28	1.1 ± 1.0	0.12 ± 0.12
Air Fresheners	1.5 ± 0.7	210 ± 110	0.54 ± 0.38
Polishes	2.7 ± 1.2	420 ± 140	1.9 ± 1.1
Industrial Degreasing	0.70 ± 0.31[a]	120 ± 40	0.1 ± 0.1
Pesticides	4.3 ± 2.0[b]	370 ± 210	2.6 ± 2.0

a. Excludes point source emissions of VCPs, and only includes those found in the area source inventory. Nationally, area sources account for 79%, 74%, 67%, and 100% of industrial adhesives, coatings, inks, and degreasing emissions, respectively. Point sources of VCP emissions are located at industrial facilities. No point source VCP emissions are in Manhattan.
b. Excludes agricultural uses of pesticides.
c. Emission factors are from McDonald et al. (28), except where otherwise denoted.
d. Estimated to be ~25% lower than national emission factors, based on more stringent New York state regulations of architectural and industrial maintenance (AIM) coatings (29).
e. Coating emission factors estimated to be ~20% lower in 2018 than in 2012 (31).
f. Consumer and industrial adhesives estimated to be ~40% and ~10% lower than national emission factors, respectively, based on more stringent New York state regulations (32).
g. Population of Manhattan is ~1.7 million people in 2018.

For other anthropogenic emission sectors (e.g., point and area sources) we utilize emissions from the National Emissions Inventory (NEI) 2014 platform (23). Power plant emissions are updated to 2018 utilizing stack monitors from the Continuous Emissions Monitoring System (CEMS). Fugitive leaks of non-methane VOCs associated with natural gas infrastructure, primarily ethane, is estimated based on recent aircraft measurements over New York City (33). Similar to VCPs, we do not see strong seasonality in fugitive leaks of pipeline natural gas as the ethane/CO ER is relatively similar between winter and summer (see Table S2).

The overall distribution of fossil-VOC emissions for Manhattan, NY are shown in Fig. S7 for the FIVE-VCP (panel A) and NEI 2014 (panel B) inventories. The distribution of VOC emissions in FIVE-VCP (Fig. S7A) is quite similar to the NEI 2014 (Fig. S7B). The main difference is that the per capita emissions in the FIVE-VCP inventory is higher than the NEI 2014 by ~50% for both mobile source engines and VCPs. This is in contrast to McDonald et al. (28), which found that VCP emissions were underestimated by factors of 2.5 and 3 for Los Angeles and the US, respectively. We also estimate higher off-road gasoline emissions relative to on-road engines. Compared to the NEI 2014, FIVE off-road gasoline emissions are higher by a factor of ~2 and on-road gasoline emissions lower by a factor of ~2. Previously, our FIVE off-road gasoline emissions were a factor of ~2 lower than the NEI 2014 across the US (28). The lower FIVE on-road gasoline emissions are consistent with our prior results (28). This highlights that methodological differences exist in how the NEI 2014 is constructed across different regions of the country. Hence, a single nationwide scaling factor for VOC emissions is likely not appropriate. Here, we construct mobile source and VCP emissions from first principles for each state separately.

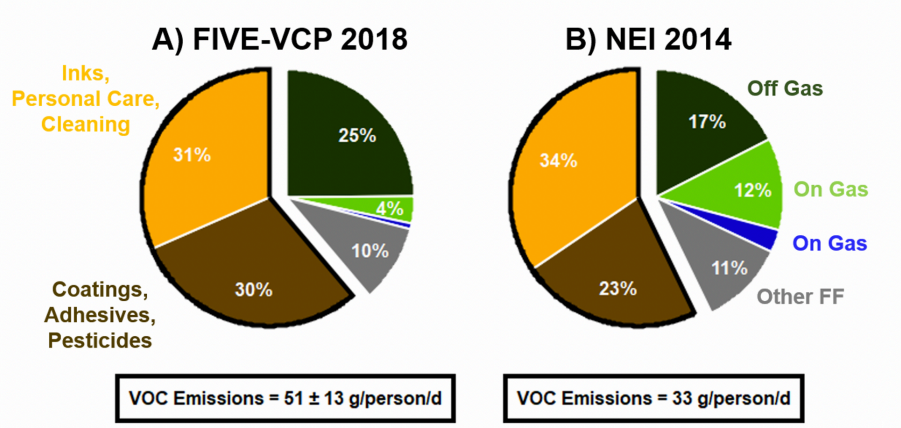

Fig. S7. Distribution of VOC emissions in Manhattan from the (A) FIVE-VCP 2018 and (B) NEI 2014 inventories. The pie charts show the contribution of VCPs (outlined in black), mobile sources (on-road + off-road engines), and other fossil fuel sources. A further emissions breakdown of VCP sources can be found in Table S4.

3.4 Evaluation of FIVE-VCP with measurements

To be able to evaluate our FIVE-VCP VOC inventory with ambient measurements, we speciate VOC emissions to individual species. We follow the approach of McDonald et al. (28). For mobile source fuels, we speciate VOCs using literature values for gasoline fuel, gasoline exhaust, and diesel exhaust (34). The VOC composition of pipeline natural gas can be found at: http://www.1line.williams.com/Transco/index.html. For VCPs, we update speciation profiles utilizing more recent CARB surveys of consumer products (35) and architectural coatings (36)

shown in Fig. S8. Note that the CARB surveys do not include industrial VCPs; therefore, these speciation profiles are taken from the EPA SPECIATE Database (v4.4) (37). For industrial VCPs, we utilize the same speciation as in McDonald et al. (28).

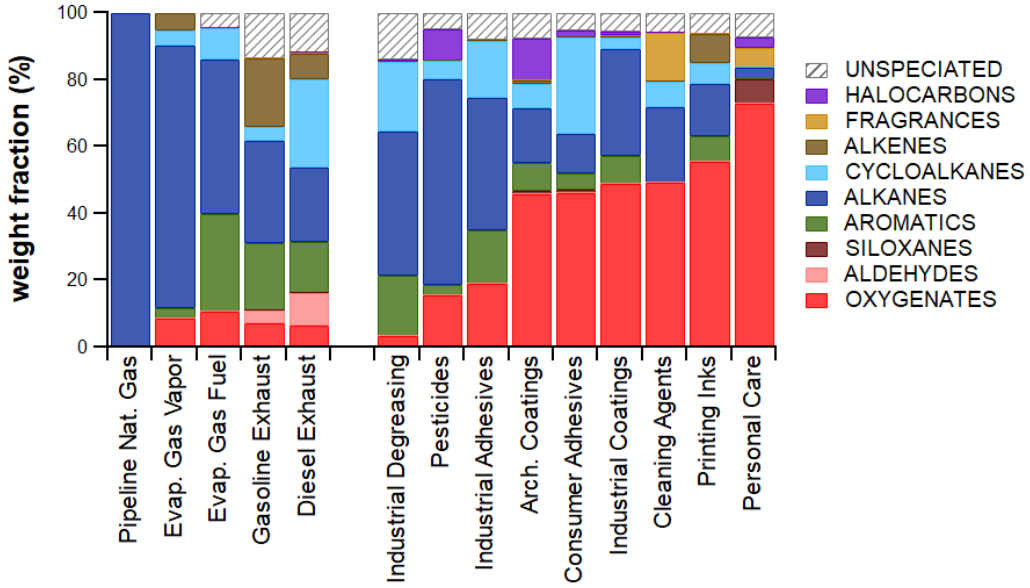

Fig. S8. VOC speciation profiles utilized in this study for fossil fuels and VCPs. Speciation profiles for VCPs have been updated to include the Consumer Product 2015 Survey from CARB (35).

Since the ambient VOC measurements are reported as enhancement ratios relative to CO (Table S2), we also evaluate the FIVE CO emissions (note that there are no primary CO emissions from VCPs). In 2015, the National Science Foundation and National Center for Atmospheric Research conducted a study aboard a C-130 aircraft over the Eastern US, the Wintertime Investigation of Transport, Emissions, and Reactivity (WINTER) field campaign. During WINTER, several of the flights targeted outflow from New York City (38). Additional flights were conducted over the Washington, DC and Baltimore region. We utilize both areas to evaluate the FIVE CO inventory here. Though the FIVE emissions were constructed for the year 2018, we do not expect significant changes in emissions between 2015 and 2018 as ambient decreases in urban CO have plateaued since around 2010 (5, 39).

On February 3, 2015 the C-130 measured downwind of NYC during westerly winds (Fig. S9A), data can be found at: https://data.eol.ucar.edu/master_lists/generated/winter/). Though other flights were conducted downwind of NYC, we choose this day since it is possible to derive CO emissions using the aircraft measurements and the mass balance technique. When winds are steady and the planetary boundary layer (PBL) depth is known, then an emissions flux can be derived using mass balance. Previously, mass balance techniques have been demonstrated in oil and gas fields (40-42) and urban areas (33, 43). Following the analysis of Peischl et al. (40), CO fluxes are calculated and compared to those from FIVE (Fig. S9A). Comparisons are limited to the hours estimated for the footprints shown, i.e., 15:00 to 17:00 LT for the smaller rectangular footprint, and 11:00 to 17:00 for the larger footprint. The latitudinal extent of the footprints is defined based on the CO enhancement plume and the wind direction. The longitudinal extent of the footprints is defined based on the average wind speed and back trajectories determined using the HYSPLIT model (44), which is plotted as a black trace in Fig. S9A. The footprints do not extend further to the east with the downwind transects because we assume the wintertime PBL is decoupled from the residual layer at 17:00. This decoupling would trap emissions from within

the footprints in the evening residual layer sampled by the C-130. For the mass balance legs, we estimate emissions of 52 ± 21 t hr^{-1} from the nearest transect, corresponding to the smaller footprint shown in Figure S9A, and 108 ± 42 t hr^{-1} and 127 ± 50 t hr^{-1} for the two transects further downwind, corresponding to the larger dashed and solid maroon footprint boxes. Uncertainties are estimated by quadrature addition of the following: PBL depth, ±300 m; wind speed, ± 1 m s^{-1}; and CO measurement uncertainty, ± 5%; and CO background uncertainty, ± 13%. In general, there is good agreement in the mean emissions from the footprint boxes between the FIVE inventory and aircraft-derived emissions, and differences within the uncertainties of the bottom-up inventory (6). In NYC, CO emissions are dominated by mobile source engines (~90% of the total).

Over the DC/Baltimore region, we evaluate FIVE against mass balance estimates of CO reported by Salmon et al. (43). In total, mass balance estimates were derived from five research aircraft flights from the NSF/NCAR C130, Purdue Airborne Laboratory for Atmospheric Research, and University of Maryland Experimental Cessna. FIVE emissions are consistent with the top-down mass balance estimates, though there is large variability in the top-down emissions. Outside urbanized areas, emissions from wood smoke are also an important source of regional CO and aerosols (38), and whose emissions are likely more variable day-to-day than mobile source engines. In short, FIVE is consistent with aircraft measurements over two major Eastern US urban regions (within 5-30%). This is in contrast to emissions from the NEI 2011 and NEI 2014, which have been suggested to be high by a factor of ~2 (6, 43). By using the FIVE-VCP emissions inventory in this study, it is unlikely that uncertainties in CO emissions inventories affect our VOC/CO comparisons described next.

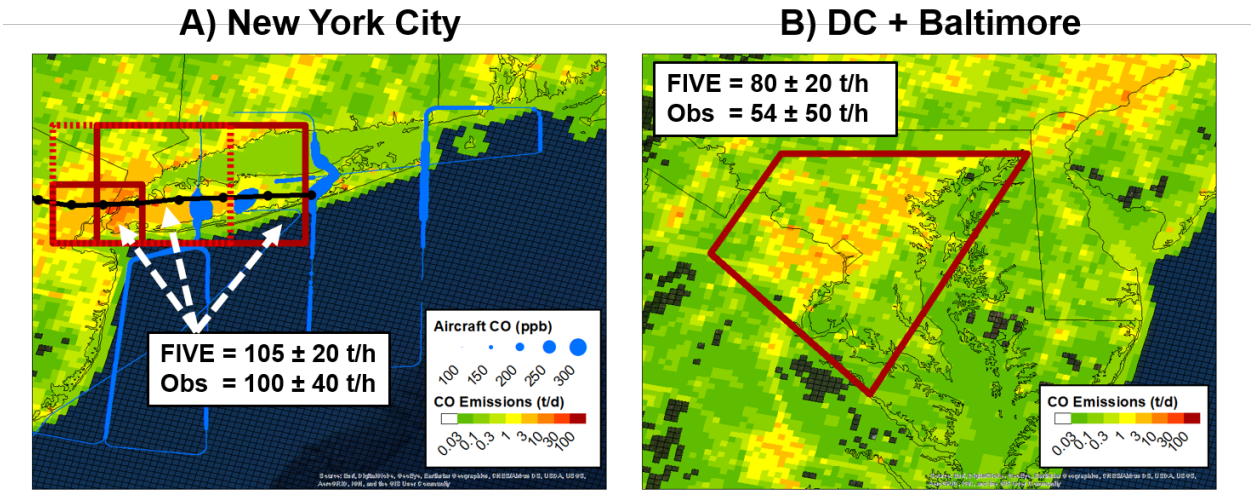

Fig. S9. (A) Flight path over New York City on February 3, 2015 during the WINTER campaign (blue dots). The flight path is sized by measured CO mixing ratios (in ppb). CO emissions from FIVE are colored on a logarithmic scale. Red boxes show the footprint over which the bottom-up FIVE inventory is compared with aircraft-derived emissions. Comparisons are limited to afternoon hours (11:00 to 17:00 local time). Uncertainties in the FIVE inventory are estimated at ~20% (6) and ~40% for mass balance emissions (42). (B) Same as panel A, except for the Washington, DC and Baltimore region during the same campaign. Aircraft-derived emissions have been previously reported by Salmon et al. (43) and shown here. The red box shows the footprint of the five research aircraft flights with mass balance estimates of CO emissions.

Combining petrochemical product sales and VOC emission factors (Tables S3-S4), and VOC speciation profiles (Fig. S8), along with our FIVE CO emissions (Fig. S9), we are able to estimate VOC/CO emission ratios from our bottom-up inventory (Fig. S10). We compare the bottom-up

VOC/CO emission ratios with those measured at the CCNY ground site averaged between wintertime and summertime. By only considering fossil fuel sources of emissions, the inventory significantly under-predicts ambient levels of VOCs by a factor of ~3 (Fig. S10A). Only when VCP emissions are included can we reconcile the inventory and ambient observations of VOC/CO ratios (Fig. S10B). These results for NYC are similar to the findings of McDonald et al. (28) for Los Angeles.

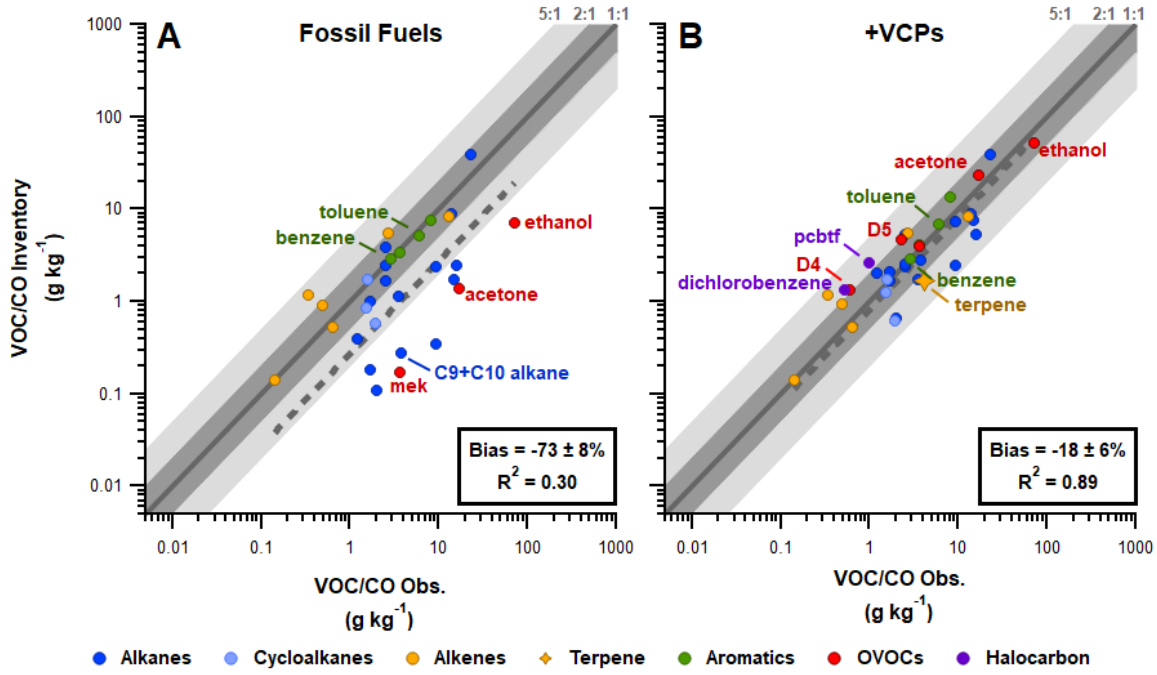

Fig. S10. Comparison of VOC/CO ratios from the FIVE-VCP inventory to ambient VOC/CO ratios measured at the CCNY ground site during winter, 2018. Comparisons between the inventory-observations are made for (A) fossil fuels only and (B) with VCPs added. The dashed line is a regression through the points shown, which is used to calculate the bias and R^2 values.

4. Description of WRF-Chem model simulations

In this study, we utilize a three-dimensional chemical transport model to assess the influence of anthropogenic VOC emissions on ozone exceedances in the Long Island Sound region. We utilize a mesoscale model, the Weather Research and Forecasting with Chemistry (WRF-Chem) model, where chemistry is fully coupled with meteorology (45). In the summer of 2018, a significant heatwave impacted the Eastern US. Figure S11 illustrates hourly ozone measured at CCNY. During the early July episode (yellow band), ozone regularly exceeded 100 ppb in Manhattan, and values were higher downwind. For reference, the current National Ambient Air Quality Standard (NAAQS) of 70 ppb MDA8 ozone is shown. Though we simulate ~1 month in WRF-Chem (gray band, 6/25 to 7/31), we focus on modeling results for July 2, 2018. This was the peak of the air pollution episode and widespread ozone exceedances were seen along the Eastern seaboard. We utilize this episode as a case study to assess the sensitivity of anthropogenic VOCs on ozone formation under policy-relevant conditions. The duration of the WRF-Chem simulation allows for sufficient spin-up time to fully model the early July heatwave, as well as smaller ozone exceedance events that occurred later in the summer. We focus on gas-phase chemistry since the measurements utilized in this study did not measure aerosol species.

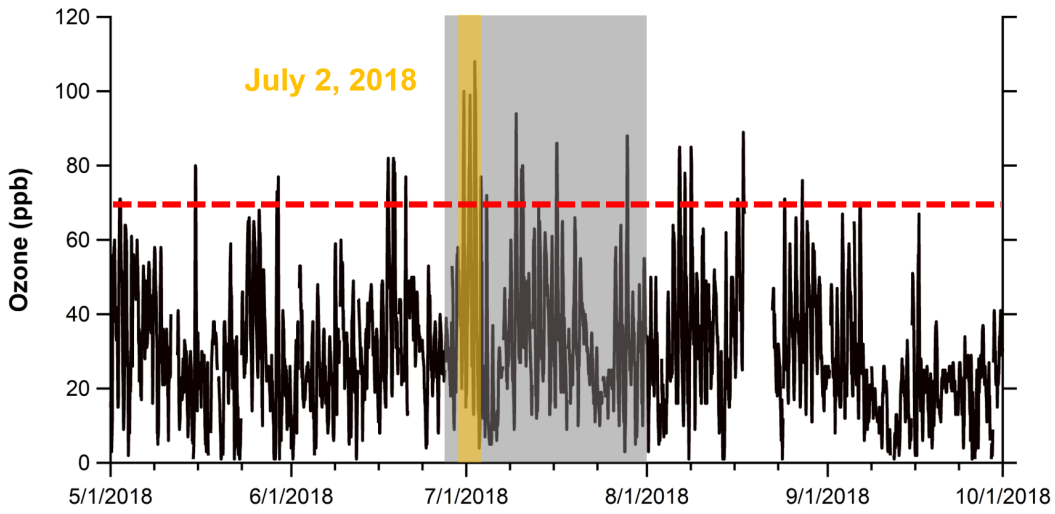

Fig. S11. Ozone mixing ratios measured at the CCNY site. Gray highlighted region shows the duration of the WRF-Chem simulation (6/27 to 7/31). The yellow band shows that the highest ozone values measured in the summer of 2018 were in early July, and the peak occurred on 7/2. The red dotted line illustrates the current MDA8 ozone standard (70 ppb).

4.1 WRF-Chem model setup

Here, we use WRF-Chem version 4.1 to simulate the Continental US at 12 km x 12 km horizontal resolution with 50 vertical levels (up to 50 hPa). The continental run provides initial and boundary conditions for the nested Eastern US domain at 4 km x 4 km horizontal resolution. We make the nested domain sufficiently large to reduce potential effects of complex terrain, due to the Appalachian Mountains, on our nested meteorological simulations. Domains are illustrated in Fig. S12.

WRF-Chem settings are provided in Table S5, many of which were used in a previous modeling study over the Southeastern US (6). For meteorology, we initialize with the North American Mesoscale (NAM) model. We utilize the Noah Land Surface Model and Mellor-Yamada Nakanishi and Niino (MYNN) planetary boundary layer scheme. For chemistry, we utilized the Madronich Photolysis (TUV) scheme, the RACM-ESRL chemical mechanism described by Kim et al. (46), and a modified chemical mechanism that accounts for the chemistry of key oxygenated VCP emissions (termed RACM-ESRL-VCP, see Section 4.3).

Model-ready anthropogenic emissions were prepared based on what was described in Section 3. Point source emissions are from the NEI 2014, except for power plants which have been updated to 2018 with stack monitoring data. Mobile source emissions are from FIVE and are mapped for the CONUS and Eastern US domains, including for CO, NO_x, and VOCs. Other mobile source species are taken from the NEI 2014. VCP emissions are estimated similarly to McDonald et al. (28) and mapped spatially by population density across the CONUS and Eastern US domains, except for agricultural pesticides and industrial VCPs. Agricultural pesticides are mapped spatially and temporally according to the NEI 2014. Point source emissions of VCPs are allocated to individual facilities according to the NEI 2014. All other area and point source emissions are mapped from the NEI 2014. The anthropogenic emission files are available at: https://www.esrl.noaa.gov/csd/groups/csd7/measurements/2018nyice/.

For biogenic emissions we utilize the Model of Emissions of Gases and Aerosols from Nature (MEGAN) model, version 2.1 (47), with adjusted isoprene emissions based on mobile van measurements (green dots shown in Fig. S12, sized by isoprene concentrations). A further description of how biogenic isoprene emissions are adjusted is provided in Section 4.3.3.

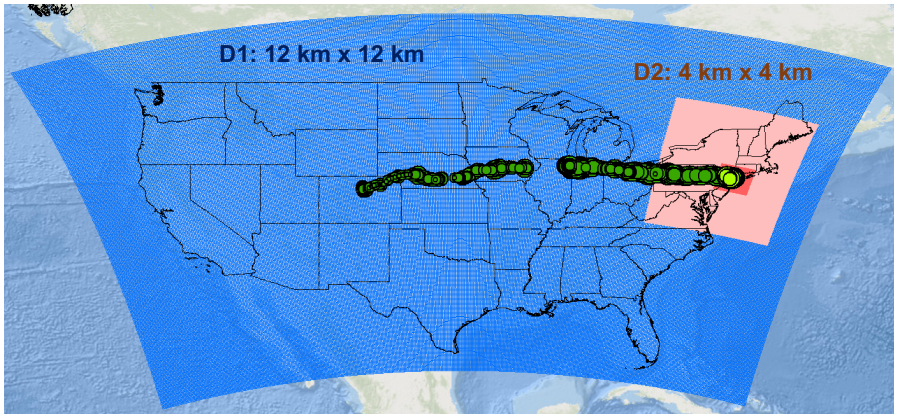

Fig. S12. The continental US (CONUS) is modeled at 12 km x 12 km resolution, which feeds a nested Eastern US domain at 4 km x 4 km resolution. The dark pink area denotes the New York City region where we calculate model-observation statistics of surface ozone. The mobile van drive track across the US (green circles, sized by isoprene mixing ratios) are used to assess biogenic emission inventories.

Table S5. WRF-Chem Model Configuration Used in This Study.[a]

Settings	Description
Horizontal Resolution	12 km x 12 km + nested Eastern US 4 km x 4km domain
Vertical Resolution	50 levels (up to 50 hPa)
Meteorology	North American Mesoscale Model
Surface Layer	Mellor-Yamada Nakanishi and Niino
Planetary Boundary Layer	Mellor-Yamada Nakanishi and Niino Level 2.5
Cumulus Scheme	Grell-Devenyi (GD) Ensemble Cumulus
Land Surface	Noah Land Surface Model
Microphysics	WRF Single Moment 5-Class
Short- and Long-Wave Radiation	Rapid Radiative Transfer Model for General Circulation Models
Gas-Phase Chemistry	RACM_ESRL (base case), RACM-ESRL-VCP (updated oVCP chemistry)
Photolysis	Madronich Photolysis (TUV)

a. See http://www2.mmm.ucar.edu/wrf/users/docs/user_guide_V3/contents.html for full description of model options.

4.2 Chemical Mechanism

A challenge for three-dimensional chemical transport models (CTMs) is whether current condensed mechanisms are able to represent the chemistry of oxygenated VCP emissions. As Fig. S8 illustrates, oxygenated VCPs (oVCPs) including alcohols, ketones, and esters are a large fraction of total VCP emissions. Traditionally, oVCP emissions are mapped to surrogate alkane bins, which is also the case for the RACM-ESRL chemical mechanism. Oxygenated VCPs, such as alcohols and glycols, are more reactive towards atmospheric oxidants than their alkane counterparts(48). Furthermore, the differences in functionality lead to the formation of secondary products at different rates and yields. For example, ethanol (the dominant oVCP) is lumped to HC3 in RACM_ESRL, which represents alkanes, alkynes, and esters with OH rate constants less than $3.4x10^{-12}$ cm^3 s^{-1} (46, 49). The resulting high-NO_x pathways lead to a mix of aldehydes and ketones at comparable yields. In reality, ethanol is expected to react with OH to primarily form acetaldehyde(48), which leads directly to peroxyacetyl nitrate (PAN), the most important temporary NO_x reservoir.

In this study, we account for the chemistry of major oxygenated VCP emissions by incorporating known oVCP oxidation mechanisms into RACM-ESRL. We focus on including the chemistry of methanol, ethanol, isopropanol, ethylene glycol, propylene glycol, glycerol, and acetone. Ethanol and isopropanol are common solvents used in most VCP sectors. Glycerol and propylene glycol are predominantly used in personal care and cleaning products. Ethylene glycol is mostly used in non-fragranced products, such as coatings and adhesives. In total, these species account for ~90% (mol/mol) of the oVCP emissions represented in FIVE-VCP inventory. Furthermore, these species represent >50% the total OH reactivity attributable to VCP emissions (see Section 9 in the Supplemental Discussion).

The directly emitted OVOCs are added as new species to the RACM-ESRL-VCP mechanism and their oxidation products are mapped to surrogates already included in RACM-ESRL. This approach accounts for the reactivity and oxidation chemistry of these OVOCs while also limiting the number of additional surrogates, which keeps the computational cost in the three-dimensional model manageable.

The atmospheric degradation of ethanol (EOH), methanol (MOH), acetone (ACT), and ethylene glycol (ETEG) are represented in reduced mechanisms, such as RACM2 (49). We incorporate these reactions into RACM-ESRL directly, and update the reaction rate coefficients based on the 2019 Jet Propulsion Laboratory Evaluation (50). Table S6 summarizes the reactions that are added to RACM-ESRL. We refer to the resulting mechanism as RACM-ESRL-VCP.

Isopropanol, propylene glycol, and glycerol are not included in RACM2. While these species could be lumped to surrogate bins (e.g., ethylene glycol), we choose to treat these species separately due to their structural differences from other species represented by RACM2. For example, propylene glycol could be lumped to ethylene glycol; however, ethylene glycol is a diol where both hydroxyl groups are linked to primary carbons, whereas propylene glycol contains one primary hydroxyl group, and one secondary hydroxyl group. The resulting chemistry is different between these two species: ethylene glycol will react with OH to predominantly form an aldehyde, whereas propylene glycol will form a mixture of aldehydes and ketones(48). Similar differences exist between isopropanol (a secondary alcohol) and ethanol (a primary alcohol).

Propylene glycol (PROG) is represented in explicit mechanisms, such as the Master Chemical Mechanism (MCM, http://mcm.leeds.ac.uk/MCM/). In the MCM, propylene glycol reacts with the OH radical to form hydroxyacetone (61%) and 2-hydroxypropanal (39%). In this study,

we incorporate the OH chemistry of propylene glycol represented in the MCM assuming the same OH rate constant and product branching ratios. Hydroxyacetone is represented as HACE in RACM_ESRL. We treat 2-hydroxypropanal as an aldehyde (ALD).

Isopropanol (IPOH) is also represented in the MCM, and predominantly forms acetone (~86%) and a smaller yield of a hydroxy RO_2 radical (~14%). To account for this oxygenated radical, we lump the RO_2 to the peroxy radical formed from reaction of OH with acetone (ACTP). Under high-NO_x conditions, the ACTP radical predominantly forms formaldehyde and the acetyl peroxy radical (ACO3). In the MCM, the hydroxy RO_2 reacts with NO to form formaldehyde and acetaldehyde.

Glycerol (GLYC) is not represented in the MCM; however, its reaction with OH is expected to be similar to propylene glycol(48). We treat glycerol separately due to its high abundance in personal care products and higher reactivity resulting from the additional primary hydroxyl group. We estimate the reaction rate coefficient and branching ratios of aldehyde and ketone formation using GECKO-A (51). The resulting ketone is lumped to the hydroxyketone surrogate (HKET), while the aldehyde is lumped to ALD.

Table S6. Reactions of key VCP emissions included in RACM-ESRL-VCP.

Species	Reaction	Rate Constant	Refs[a]
Methanol	MOH + OH = HCHO + HO2	2.9e-12 exp(-345/T)	(49, 50)
Ethanol	EOH + OH = ALD + HO2	3.35E-12	50)
Isopropanol	IPOH + OH = 0.861 ACT + 0.139 ACTP + 0.861 HO2	2.1e-12 exp(270/T)	(50, 52)
Ethylene glycol	ETEG + OH = ALD + HO2	1.47E-11	(49)
Propylene glycol	PROG + OH = 0.387 ALD + 0.614 HACE + HO2	2.15E-11	(52)
Glycerol	GLYC + OH = 0.45 ALD + 0.55 HKET + HO2	5.45E-11	(51)
Acetone	ACT + OH = ACTP + H2O	1.33e-13+3.82e-11 exp(-2000/T)	(49, 50)
	ACTP + NO = ACO3 + NO2 + HCHO	2.9e-12 exp(300/T)	(49)
	ACTP + HO2 = 0.15 OH + 0.15 ACO3 + 0.15 HCHO + 0.85 OP2	8.6e-13 exp(700/T)	(49)
	ACTP + NO3 = ACO3 + NO2 + HCHO	2.30E-12	(49)
	ACTP + ACO3 = ACO3 + HCHO + CO2 + MO2	2e-12 exp(500/T)	(49)
	ACTP + MO2 = 0.5 MOH + 0.8 HCHO + 0.3 HO2 + 0.3 ACO3 + 0.5 MGLY + 0.2 HACE	7.5e-13 exp(500/T)	(49)
	ACT + hv = MO2 + ACO	JPL Recommendations	(49, 50)
	HACE + hv = HCHO + HO2 + ACO_3	jACT	

[a] Reactions for methanol, ethanol, and acetone are adapted from RACM2 (49), with updates to the rate constants based on the 2019 JPL kinetic evaluation (50). The reaction and rate constant for ethylene glycol are from RACM2 (49). The reactions for propylene glycol and isopropanol are adapted from the MCM (52), with updates to the rate coefficient for isopropanol (50). The reaction and rate coefficient for glycerol is adapted from GECKO-A (51).

WRF-Chem and box model simulations employ both RACM-ESRL and RACM-ESRL-VCP. For simulations using RACM_ESRL, we lump oxygenated VCP emissions to traditional alkane surrogates. For simulations using RACM-ESRL-VCP, we model the key VOCs described in Table S6, and lump lesser-abundant species to the oxygenated surrogates based on structural similarities. Glycols and glycol ethers containing two primary hydroxy groups are lumped to ETEG. Glycols and glycol ethers with a single primary hydroxyl and one or more secondary hydroxyl groups are lumped to PROG. Secondary alcohols are lumped to IPOH, whereas primary alcohols are lumped to EOH.

Siloxanes are not included in the current RACM-ESRL or RACM-ESRL-VCP mechanisms, and limited studies have characterized their gas-phase oxidation chemistry. In this study, we map siloxane emissions to benzene given their similar reactivity with the hydroxyl radical (53, 54). Lastly, we speciate "fragrances" as terpenes (50% limonene and 50% a-pinene based on mobile laboratory measurements) and the balance as propylene glycol (which is then mapped to the HC8 alkane bin for RACM_ESRL, and PROG for RACM-ESRL-VCP). As described in Section 3.1, fragrances are a mixture of terpenes, esters, and glycols.

4.3 WRF-Chem model evaluation

We evaluate the WRF-Chem model for meteorology and key precursors contributing to high ozone during the early July, 2018 heatwave, including assessing anthropogenic NO_x emissions, biogenic isoprene emissions, and anthropogenic terpene emissions. Many of the measurements described below were made as part of the LISTOS 2018 study and data available at the NASA Langley Research Center data archive: https://www-air.larc.nasa.gov/missions/listos/index.html.

4.3.1 Comparison to urban meteorology measurements

Figure S13 shows comparisons of the WRF-Chem model with the CCNY Leosphere 200S Windcube Doppler Wind lidar, which measures three-dimensional wind profiles. The wind profiles are retrieved from the lidar using a technique referred to as Doppler Bean Steering (DBS). The lidar operates at 20 kHz repetition rate. The scan pattern includes one zenith measurement (averaged over approximately 2 sec) and four measurements at 25 degree zenith angle and 0, 90, 180, and 270 Deg azimuth angle (averaged over ~4 seconds each). Wind speed profiles along the line-of-sight are obtained from each of these observations, and then used to retrieve reconstructed wind vector profiles assuming homogeneity for each range over the measurement volume.

During the early July ozone episode (denoted by the black boxes), stagnant wind conditions (<5 m/s) are observed by the wind lidar (panel A) and simulated by the model (panel B). The stagnant winds are also accompanied by a consistent land-sea breeze where offshore winds blow from the north at night (red/purple shading in panel C) and switch around noon to on-shore winds from the south (yellow/green shading in panel C). The model also captures this general wind pattern (panel D), which along with stagnant winds allows for multi-day aging of the New York City plume. After the episode, the winds are consistently from the south and blowing the urban plume further afield.

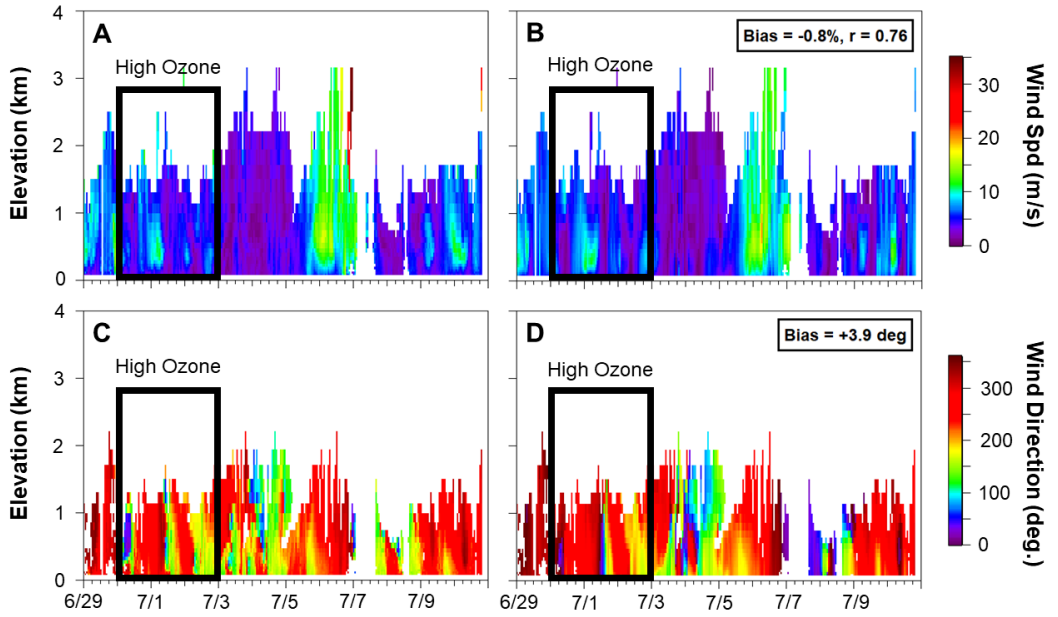

Fig. S13. Top row shows comparison of horizontal wind speeds within the planetary boundary layer for (a) Doppler Wind lidar data collected at CCNY with (b) WRF-Chem model. Bottom row shows the same, except for wind direction for (c) wind lidar and (d) WRF-Chem model. Normalized mean bias of the model and Pierson correlation coefficient shown.

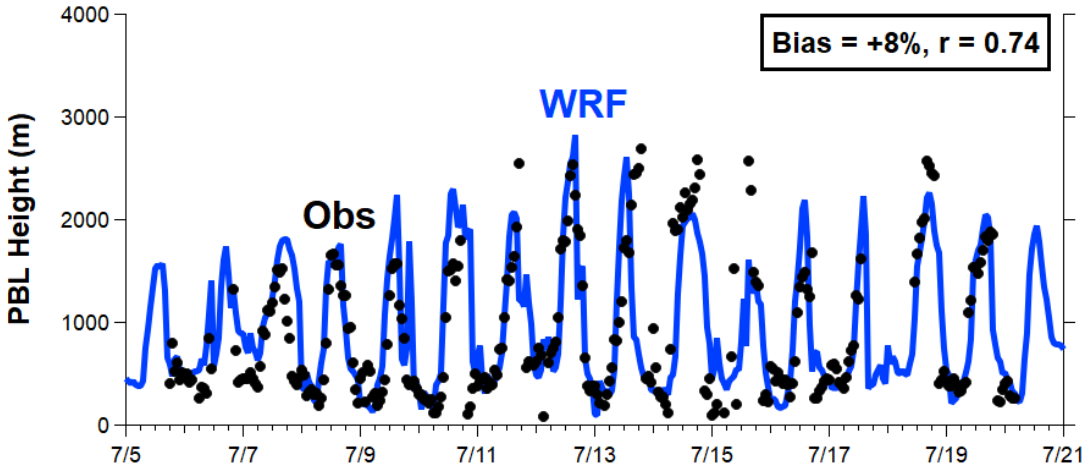

Fig. S14. Time series of planetary boundary layer height as measured by the CCNY ceilometer lidar (black dots) and as simulated by the WRF-Chem model (blue line). Normalized mean bias of the model and Pierson correlation coefficient are shown.

Figure S14 shows the comparisons of the WRF-Chem model with the CCNY Vaisala CL51 ceilometer lidar when data is available, which provides planetary boundary layer (PBL) height (55). PBL height is retrieved from attenuated backscatter profiles obtained from the ceilometer. For data from January to March, the retrieval method was through application of a covariance wavelet transform to the ceilometer profiles (55, 56). For the data in June and July, we used the propriety Vaisala Boundary Layer View software package (BL-VIEW, https://www.vaisala.com/en/products/software/bl-view). We had tested BL-VIEW and find the results to be consistent

to the wavelet method. In general, the model appears to capture the PBL height on average with typical values of 1.5 to 3 km in the summertime.

4.3.2 Comparison to urban NO_x measurements

During the LISTOS 2018 study, there were 8 Pandora spectrometers measuring total nitrogen dioxide (NO_2) columns and located around the Long Island Sound region. Here we use data for the following sites: Branford (CT), Bronx (NY), Madison (CT), New Brunswick (NJ), New Haven (CT), New York City (NY), Old Field (NY), and Westport (CT). Together these 8 sites span both upwind, urban core, and downwind areas of New York City. The Pandora data are available at: http://lb3.pandonia.net/. Pandora spectrometers are direct sun measurements that report total column NO_2 (i.e., stratosphere + troposphere), as well as other species (57). During the day, the spectrometer tracks the sun and an algorithm converts the slant columns into vertical columns with a clear-sky precision of 2.7 x 10^{14} molecules/cm^2. Previously, Pandora spectrometers have been used to validate satellite and aircraft-based retrievals of NO_2 (58-60).

Since our WRF-Chem model does not fully resolve the stratosphere, we add 3 x 10^{15} molecules/cm^2 of stratospheric NO_2 for Northern mid-latitudes, based on global stratospheric modeling (61). Figure S15 shows the comparison of WRF-Chem with the Pandora NO_2 data. For each hour of observations, which are limited to daytime values, we take an average across all sites (up to 8) in the model and for the Pandora spectrometers. To first order, the model predicts the total NO_2 column within ~10% of the Pandora observations, and within the emissions uncertainty of the bottom-up fuel-based inventory of NO_x (6, 39).

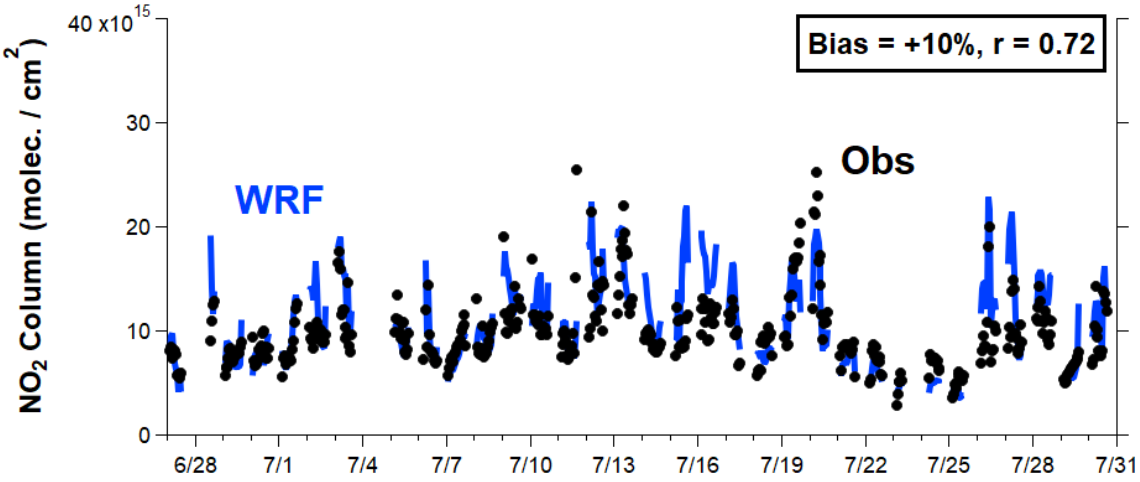

Fig. S15. Comparison of column Pandora measurements of NO_2 (black dots) with WRF Chem (blue line). Values shown are averaged across all sites for each hour (up to 8 sites total). Normalized mean bias of the model and Pierson correlation coefficient are shown.

4.3.3 Comparison to mobile laboratory measurements of biogenic emissions

During the summertime, biogenic isoprene is the dominant VOC emitted in the Eastern US(62, 63). However, previous studies have identified factor of ~2 uncertainties in biogenic inventories (64, 65). Here we utilize the MEGAN model (version 2.1) for biogenic emissions as our starting point. We constrain the inventory with mobile laboratory measurements on the drive back from New York City to Boulder, Colorado (green dots in Fig. S12 on 7/24/18 to 7/26/18). To facilitate model-observation comparisons we consider a more conserved tracer of isoprene

emissions that includes its first generation oxidation products of methacrolein (MACR) and methyl vinyl ketone (MVK) (65). The mobile laboratory measurements are binned by longitude at 0.5 degrees and the median value taken to reduce the effect of outlier observations on the comparison. We also perform a sensitivity test where we halve the isoprene emissions in WRF-Chem. In general, the mobile laboratory measurements of our isoprene emissions tracer are in between the full isoprene and half isoprene model cases (Fig. S16). This is consistent with prior modeling of the Southeastern US by McDonald et al. (6), which found that isoprene emissions from the MEGAN inventory were high relative to NOAA P3 aircraft measurements but that the BEIS inventory was low, whose isoprene emissions are a factor of ~2 lower than MEGAN.

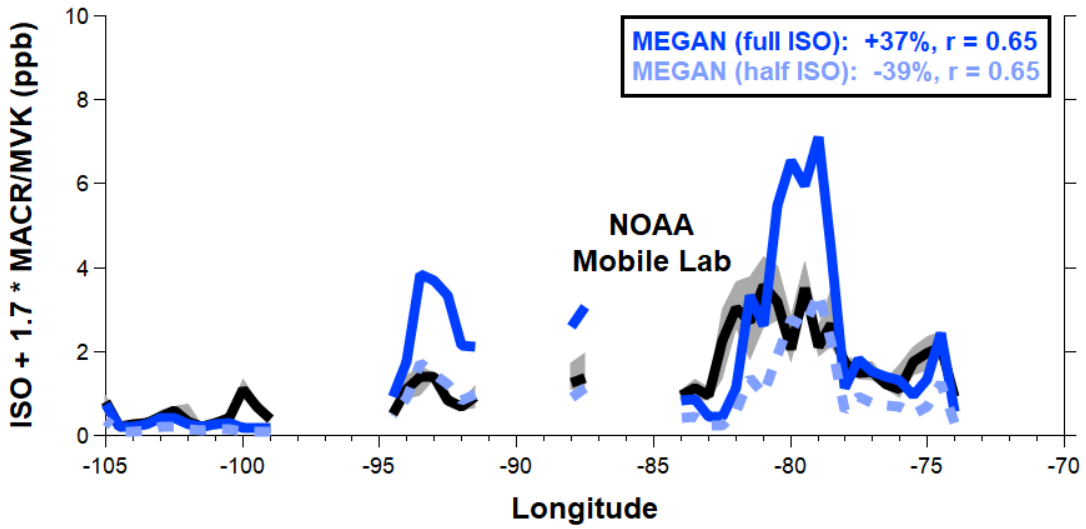

Fig. S16. Comparison of mobile laboratory measurements (black line) of isoprene + first generation isoprene oxidation product (MACR + MVK) with WRF-Chem (blue lines). Dark blue line represents simulating unadjusted isoprene emissions from MEGAN, and light blue line represents simulating half of the isoprene emissions from MEGAN. The scaling factor of 1.7 is taken from Warneke et al. (65). The bands of the mobile laboratory measurements reflect 25th and 75th percentiles of the observations, and the black line the median. Normalized mean bias of the model and Pierson correlation coefficient are shown.

We also perform an analysis of the biogenic inventory with local drives across the New York City region shown in Fig. S17. Here it is clear that both isoprene and its first-generation oxidation products (MACR + MVK) are 60-70% higher than the mobile laboratory measurements, suggesting that the biogenic isoprene emissions are high under the full isoprene case. When we halve isoprene emissions in MEGAN, the results for isoprene (Fig. S17A) and MACR + MVK (Fig. S17B) improve. Since the focus of our modeling is on the New York City region, we utilize the half isoprene case more consistent with the observations in our base simulation of ozone. Unlike isoprene and methacrolein + MVK, monoterpene concentrations exhibit a local maximum in the mobile laboratory measurements in Manhattan. This local peak can only be accounted for when including anthropogenic terpene emissions equivalent to 860 mg person^{-1} d^{-1}. Even if there are biogenic terpenes emitted outside the city, they react away before reaching the city center, as shown by the model simulation where no anthropogenic terpenes were included (Fig. S17C).

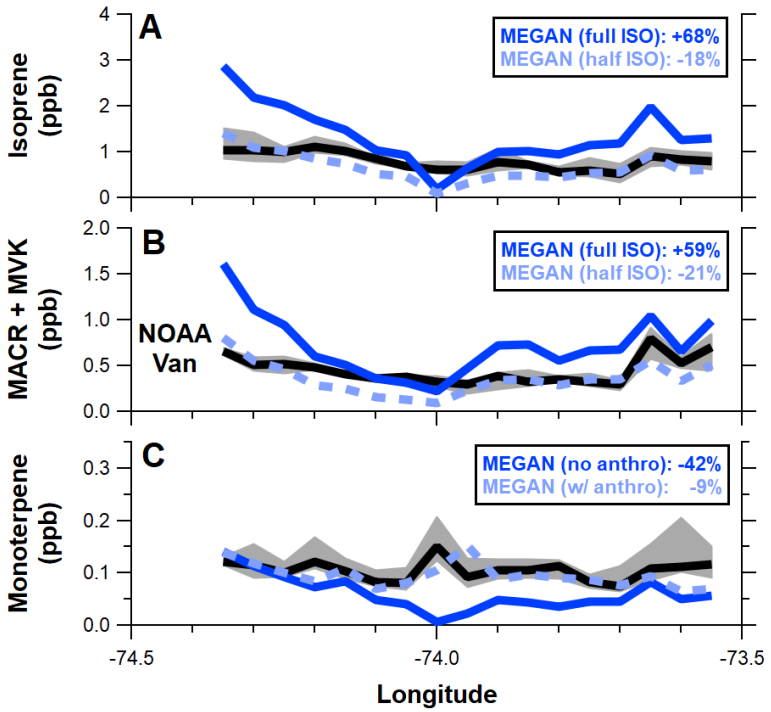

Fig. S17. (A) Comparison of mobile laboratory measurements (black line) of isoprene with WRF-Chem (blue lines). Dark blue line represents simulating unadjusted isoprene emissions from MEGAN, and light blue line represents simulating half of the isoprene emissions from MEGAN. The bands of the mobile laboratory measurements reflect 25th and 75th percentiles of the observations, and the black line the median. Normalized mean bias of the model are shown. (B) Same as panel A, but for MACR + MVK. (C) Same as panel A, but for monoterpenes. Here the dark blue line reflects simulating MEGAN biogenic emissions without anthropogenic terpene emissions. The light blue line reflects WRF-Chem simulations with MEGAN + anthropogenic terpene emissions.

4.3.4 Comparison to ozone measurements

During the LISTOS 2018 campaign, the NASA Langley mobile ozone lidar (LMOL) was deployed at Westport, CT which is located on the coast of the Long Island Sound. The LMOL is a ground-based tropospheric profiling ozone lidar system housed in a mobile trailer (66, 67). LMOL relies on ultraviolet (UV) pulsed laser source that produces two wavelengths allowing for calculation of O_3 concentration profiles from atmospheric differential absorption (DA). The laser transmitter consists of a custom-built Ce:LiCAF tunable UV oscillator that is pumped by a frequency-doubled (527 nm) commercially available Nd:YLF laser operating at a 1 kHz repetition rate. Pulsed laser light was transmitted in a fixed zenith orientation into the atmosphere from a window opening on the trailer roof, alternating pulse to pulse between the on- and offline wavelengths (500 Hz each).

Backscattered light from the atmosphere was collected by two co-aligned fiber-optic coupled telescopes, one designed for 1-8 km atmospheric backscatter and a second designed for near-range .1 to1 km atmospheric signals (68). The fiber outputs from the telescopes were connected to a light-tight enclosure containing UV band-pass filters integrated with photo-multiplier tube (PMT) detectors. A Licel data system provided simultaneous analog and photon-counting outputs that were synchronously gated with the alternating wavelength pulses, to separate on and offline data, and subsequently recorded by the instrument computer system for processing of raw signals into calibrated ozone profiles.

The processing of profiles was implemented following the standard DA lidar technique (69). Analog and photon-counting from the multiple telescopes are merged together to provide a single optimized profile for range and signal-to-noise performance. Ozone cross sections along with pressure and temperature information are used as part of the process to extract ozone mixing ratio as a function of altitude. The process is repeated for each new profile on a 5–10 min temporally averaged basis, to provide a continuous curtain display on the evolution of ozone vertical distribution during the course of a day. A real-time data display was also available, allowing for display of the system-generated ozone curtain profiles as they are collected, for immediate feedback on atmospheric observations. Uncertainty estimates for LMOL follow the procedure described in Leblanc et al (70). The optimization of vertical resolution with altitude follows Gronoff et al. (67). The LMOL is part of NASA's Tropospheric Ozone Lidar Network (TOLNet), and has been validated against other TOLNET lidar and ozonesondes (71). Validation against ozonesondes were performed during the LISTOS campaign.

The lidar was operated to target high air pollution episodes, with ozone concentrations exceeding 70 ppb at the surface for several days in July (Fig. S18A). In panel B, we show vertical ozone profiles simulated by the WRF-Chem model. The model captures the temporal evolution and vertical structure of the ozone plume (r = 0.79), on both polluted and clean days. The model performance is better when limited to the surface (height < 2500 m, r = 0.84). The model tends to under-predict ozone in the upper troposphere, but strong mixing down to the surface is not evident. Overall, the model exhibits a slight under-calculation in ozone.

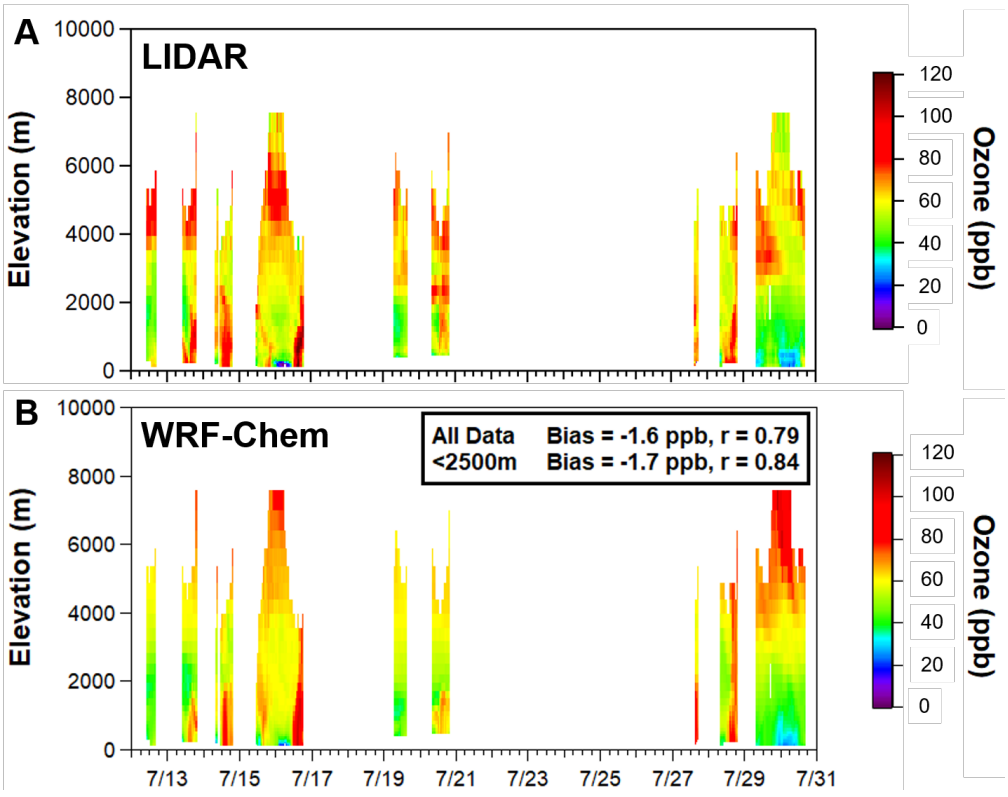

Fig. S18. (A) Hourly time series of ozone lidar measuring vertically-resolved ozone. Lidar data has been averaged to the vertical resolution of the WRF-Chem model. (B) Same as panel A, except with results from the WRF-Chem model base simulation. Normalized mean bias of the model and Pearson correlation coefficient are shown for all data shown and values less than 2500 m, which approximates the daytime PBL max.

We also evaluate the WRF-Chem model with routine air quality stations located in the NYC region (dark pink area shown in Fig. S12). Across this region are ~40 monitoring locations, which are able to provide an observational constraint on the spatial extent of the ozone plume. Figure S19 shows the hourly mean ozone value across the NYC region in the WRF-Chem model and observations. On average, the model tends to over-predict ozone by -3 ppb, though captures the spatial extent and evolution of the ozone plume well (r = 0.91). Much of the high bias in the model occurs at night, when the meteorological performance is expected to be poorer relative to daytime hours. When we limit the comparison to daytime hours (8 AM to 8 PM local time), the high model bias reduces to ~0.5 ppb of ozone. Based on the model evaluations with the ozone lidar and surface monitors, the WRF-Chem simulation is capturing the spatial, temporal, and vertical evolution of ozone pollution in the NYC region well.

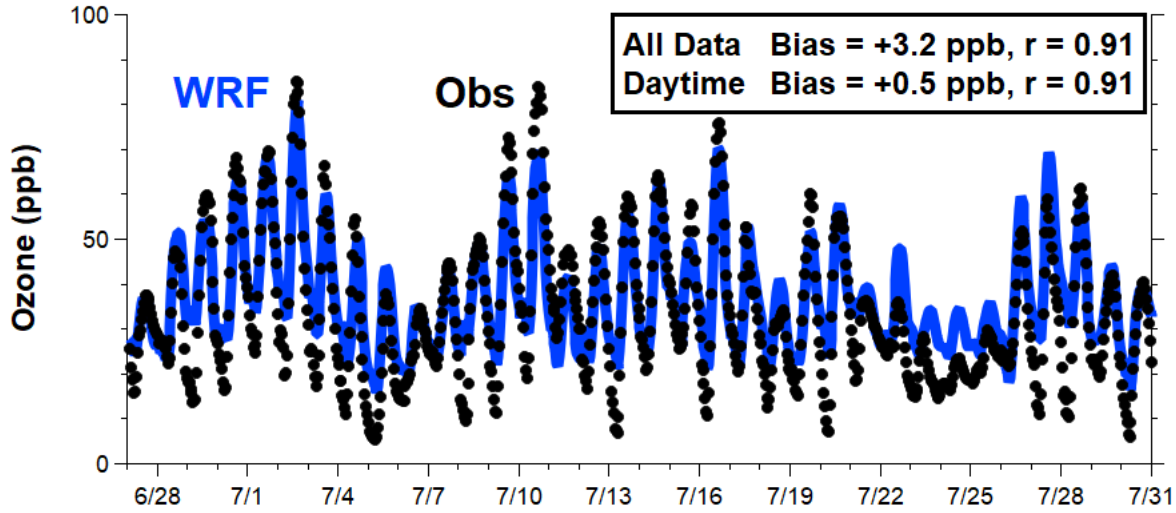

Fig S19. Hourly time series of surface ozone (black dots) and corresponding WRF-Chem simulations (blue trace) at ground sites located in New York City region (see dark pink area in Fig. S12). Values shown have been averaged across all sites for a given hour (28-40 sites across the region). Normalized mean bias of the model and Pearson correlation coefficient are shown for all data shown and daytime values (8 AM to 8 PM local time).

4.3.5 Comparison to measurements of other secondary products

In addition to ozone, we evaluate WRF-Chem simulations of other secondary products, such as formaldehyde. Formaldehyde is produced by the reaction of biogenic and anthropogenic VOC precursors and is an important secondary VOC that can contribute to OH production through photolysis. In NYC, formaldehyde is predominantly formed by secondary processes, and may contribute upwards of 20% to the OH + HO_2 budget during summertime oxidation (72). Lin et al. (72) found that isoprene is the dominant formaldehyde precursor in the NYC area (~50%), followed by anthropogenic sources of methane and propene.

During the LISTOS campaign, formaldehyde was measured downwind of NYC in Westport, CT using an Aerodyne Mini Quantum Cascade Laser (QCL) trace gas monitor. The instrument measures formaldehyde, formic acid, and water vapor at 1765 cm-1 using a room temperature continuous wave QCL, and is based on the earlier pulsed QCL system described by Herndon et al. (73). Sample gas is pulled through a heated (30 ℃) glass inertial impactor inlet that removes particles above 100 nm and contains a critical orifice to control sample flow into the sample cell.

A 1 meter heated Teflon transfer line transfers gas from the inlet to the cell, a 76 m pathlength, 0.5 L multipass absorption cell. An Agilent Triscroll 600 vacuum pump is used to control cell pressure, which is around 35 to 45 torr during normal operating conditions.

Frequent background spectra of formaldehyde-free zero air, measured through the same inlet as the sample, are taken every for 30 seconds every 5 minutes. A Teledyne API T701H High Performance Zero Air Generator with a heated catalytic hydrocarbon scrubber is used to produce the formaldehyde-free zero air on demand, and produces a formaldehyde blank as good or better than Ultra Grade zero air cylinders. Sample spectra are normalized to the background spectra and the resulting differential spectra are fit using a non-linear least squares fitting algorithm assuming a Voigt absorption profile. Fitting parameters are taken from the HITRAN database (74), and three species (water vapor, formaldehyde, and formic acid) are fit simultaneously to account for minor spectral overlap of these species in this spectral region (discussed in detail in Herndon et al., 2007). The accuracy of the measurements is anchored to the spectroscopic line parameters in the HITRAN database (74) and is estimated to be on the order of 5%. Comparison with certified formaldehyde reference gas cylinders or permeation tubes on multiple occasions were within the combined uncertainties of the Aerodyne instrument (5%) and the gas cylinder certification (generally also 5%). The precision of the measurements, computed as the Allan-Werle deviation (75) for a 5-minute measurement cycle, is better than 20 pptv.

Figure S20 shows the model comparison to measured formaldehyde mixing ratios. The model generally captures the temporal evolution and magnitude of formaldehyde downwind of NYC. Over the entire simulation, the model under-predicts formaldehyde by ~ 18%. When comparing to daytime measurements, we find that the model over-predicts by ~16%. The correlation between modeled and measured formaldehyde is lower than for ozone, but comparable to the correlation for Pandora NO_2 measurements. This lower correlation could be associated with a model comparison to a single site, as well as the uncertainties associated with the model's ability to resolve coastal boundary layer dynamics on any given day.

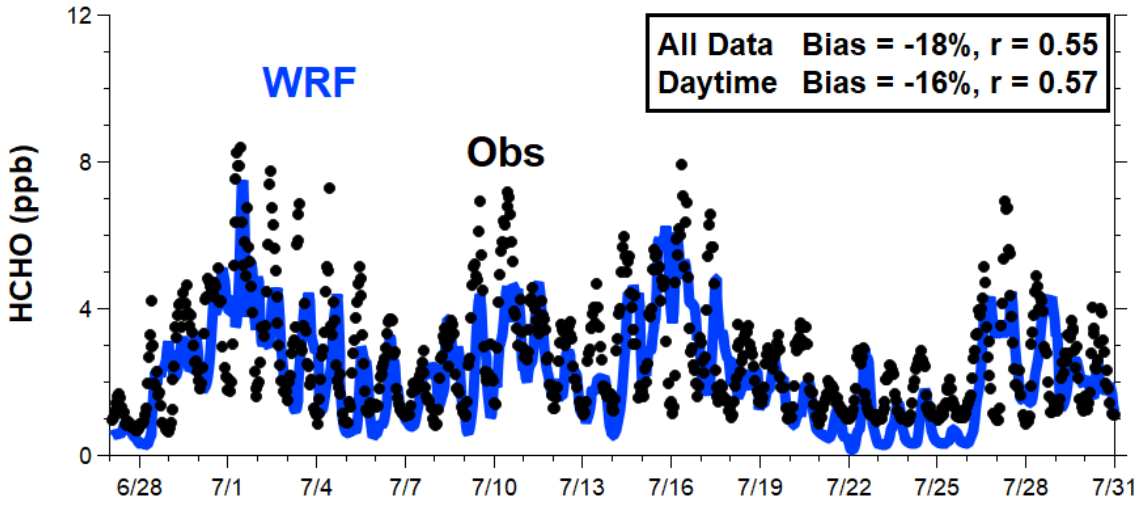

Fig. S20. Hourly time series of surface formaldehyde (black dots) and corresponding WRF-Chem simulations (blue trace) at a ground site located in Westport, CT. Normalized mean bias of the model and Pearson correlation coefficient are shown for all data shown and daytime values (8 AM to 8 PM local time).

4.3.6 Comparison of WRF-Chem model to aircraft data collected during the July 1 – 3 heat wave.

Finally, we evaluate WRF-Chem output against aircraft data collected during the heat wave event described in the main text. On July 1-2, the University of Maryland (UMD) Cessna 402B flew over NYC to sample trace gasses as part of the LISTOS campaign. The aircraft conducted four 3-hr flights – two on July 1 (9:00 AM – 12:30 PM and 4:40 PM – 7:30 PM EDT) and two on July 2 (9:00 AM – 12:30 PM, 3:00 PM – 6:30 PM, EDT). We report measurements of CO, O_3, and NO_2. CO was measured by a Picarro Model G2401-m cavity ringdown spectrometer. Ozone was measured by a Thermo Electron Model 49 UV absorption O_3 analyzer. NO_2 was measured by a Los Gatos Research Model RMT-200 NO_2 analyzer based on cavity enhanced absorption spectroscopy. The Picarro analyzer and NO_2 analyzer were calibrated with NIST-traceable standards. The O_3 analyzer was calibrated with a primary O_3 calibrator that was calibrated with a standard reference photometer at NIST (76).

Figure S21 summarizes the UMD Cessna 402B flight tracks. On July 1, the winds predominantly pushed the NYC plume offshore towards Long Island, and ozone in the plume reached mixing ratios > 120 ppb downwind of Manhattan. On July 2, the plume was transported over land to the north of the city and reached mixing ratios > 130 ppb. On both days, the aircraft predominantly sampled at altitudes < 1.5 km. Over land, measurements were predominantly sampled within the boundary layer, while measurements over water were influenced by marine boundary layer dynamics. Here, we compare model output to all measurements, but focus on comparisons during the afternoon during peak ozone production.

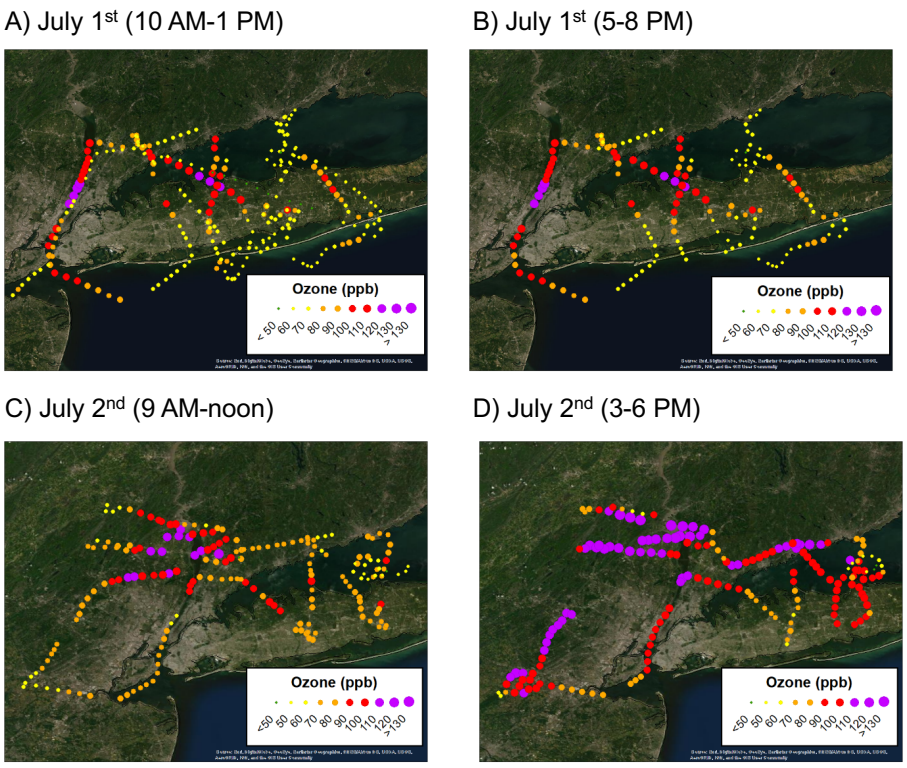

Fig. S21. UMD Cessna 402B flight tracks over the NYC region during the July 1-2, 2018 heat wave event. Flight tracks are colored by ozone mixing ratios.

Figure S22 compares WRF-Chem output to CO and NO_2. Overall, WRF-Chem describes these measurements to within 20%. During peak ozone production on the highest ozone exceedance (column D, July 2, 3:00 PM – 6:00 PM), both CO and NO_2 are described to within 10%. The agreement for CO illustrates that the CO emission inventory used in this study generally captures anthropogenic emissions, and further supports that the anthropogenic VOC inventory, constrained by VOC/CO ratios measured from CCNY (Fig. S10), is well represented by WRF-Chem.

Over the entire event, WRF-Chem under-predicts ozone by ~11 ppb. This difference is largely driven by the underprediction in morning ozone mixing ratios on July 2 (column C, 9:00 AM – 12:00 PM), which is also the period where CO and NO_2 mixing ratios are also most underpredicted. This underprediction is most likely related to difficulties for WRF-Chem in simulating urban and coastal meteorological dynamics during early morning hours when the PBL rapidly develops between 9:00 AM – 11:00 AM (Fig. S27A). WRF-Chem model output are better simulated in the afternoon sampling period (column D, 3:00 PM – 6:00 PM, bias < 2%), after the PBL has fully developed. During the afternoon of July 2, 2018, which is the period analyzed by 3D and box models (Figures 3, 4, and 5, main text), WRF-Chem simulations reasonably capture the emissions and resulting chemistry of the NYC region.

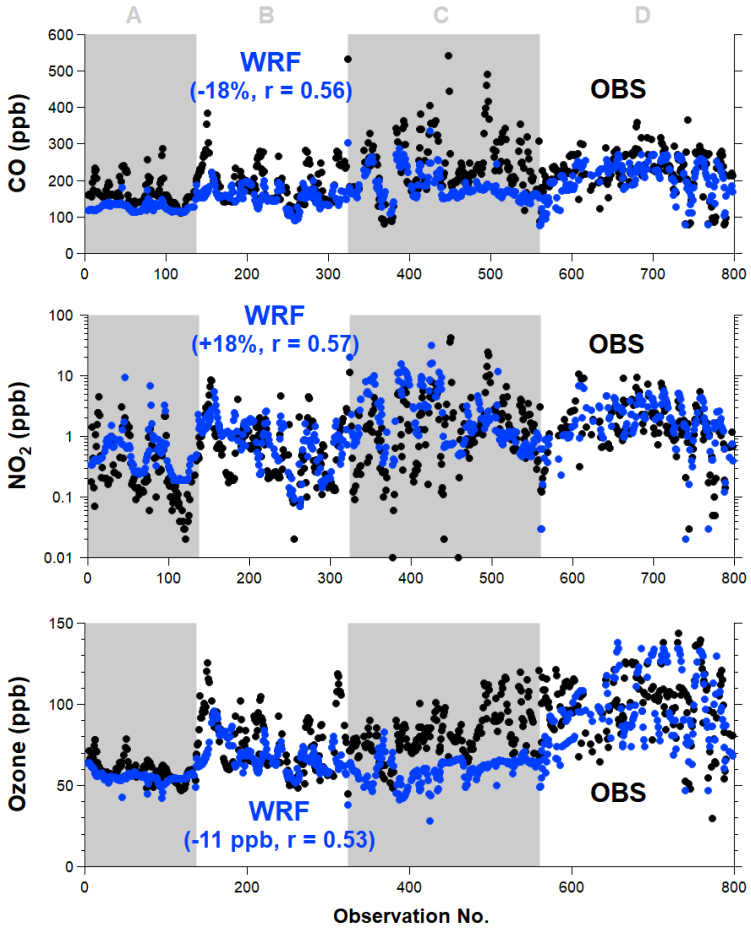

Fig. S22. Comparison between the UMD Cessna 402B observations of CO, NO_2, and ozone and WRF-Chem simulations during (A) July 1, 10:00 AM – 1:00 PM, (B) July 1, 5:00 PM – 8:00 PM, (C) July 2, 9:00 AM – 12:00 PM, and (D) July 2, 3:00 PM – 6:00 PM.

4.3.7 MDA8 ozone simulations over the entire July 2 heat wave.

Figure 3 in the main text shows WRF-Chem simulations for July 2, 2018, which was the highest ozone exceedance observed over a 3-day heat wave (July 1 -3, 2018). Figure S23 shows the same sensitivity analyses, but for MDA8 ozone averaged over the entire heat wave. Panel (A) shows ozone produced from the reactions of biogenic VOCs (BVOCs) along with NO_x, panel (B) shows the results from (A), but with fossil fuel VOCs include, and panel (C) shows the results from (B), but with VCP VOCs included. Panels (A-B) show WRF-Chem simulations using RACM-ESRL (hydrocarbon chemistry), while panel (D) shows simulations using RACM-ESRL-VCP (oVCP chemistry).

On July 2, peak ozone was formed downwind of NYC; however, over a 3-day average, ozone is distributed more broadly across the metropolitan area. The MDA8 ozone calculated from surface monitors show that all 5 boroughs of NYC and parts of northern New Jersey exceeded the 70 ppb NAAQS over the 3-day period. As was shown in Fig. 3, most of the ozone is attributed to BVOCs reacting alongside NO_x. Panel (A) shows that BVOCs were responsible for 66 ppb of the ozone simulated over NYC, and 73 ppb of the maximum ozone simulated within the modeling domain. Panel (B) shows that fossil fuel VOCs enhance ozone to 69 ppb in NYC (an increase of 3 ppb) and 75 ppb at the ozone maximum (an increase of 2 ppb). Inclusion of VCP emissions (panel C) pushes ozone to 73 ppb in NYC (an increase of 4 ppb) and 80 ppb at the ozone maximum (an increase of 5 ppb).

Fig. S23 shows that anthropogenic VOCs contribute 7 ppb of ozone to NYC and the domain maximum. The contribution of VCPs to ozone derived from anthropogenic sources is ~60%, which is consistent with the amount estimated for the July 2 exceedance (60%, Fig. 3). These results show that the ozone attribution estimated for July 2 generally applies for the broader heat wave event. Finally, panel (D) shows the impact of oVCP chemistry on ozone simulations. The increase in ozone is modest (~1 ppb), which is consistent with the results shown in Fig 3.

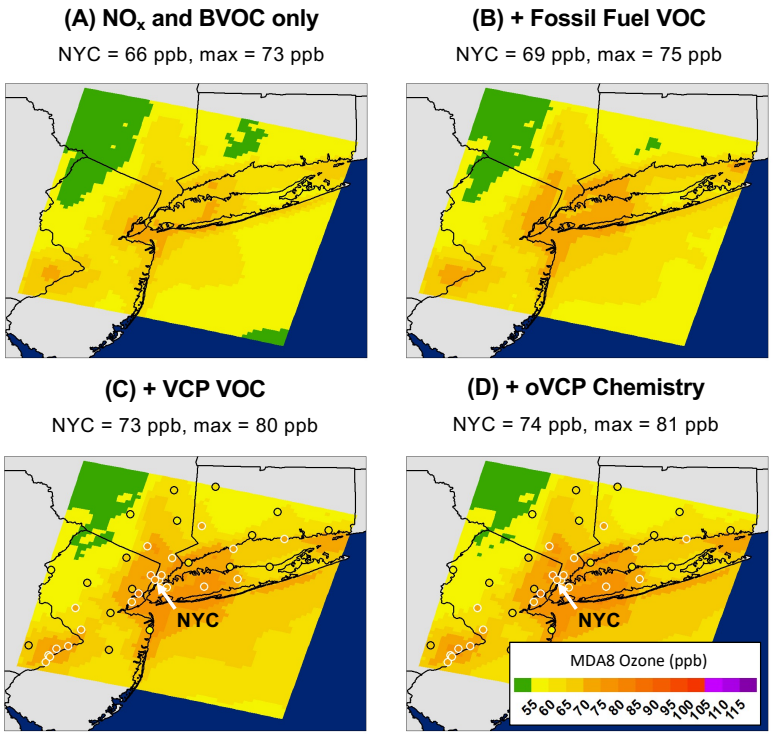

Fig. S23. WRF-Chem simulations of maximum MDA8 ozone averaged over the 3-day heat wave from July 1 - 3, 2018. Shown are simulations for (A) global background + NO_x and BVOCs, (B) results from (A) with mobile source VOCs added, and (C) results from (B) with VOCs from VCPs added. Panels A-C show ozone produced under the assumption of hydrocarbon chemistry. Panel (D) shows the simulation using full emissions, but under the assumption of oVCP chemistry. Circles show ozone mixing ratios measured at monitoring stations in the NYC area; those bolded in white exceeded US NAAQS. The numbers above each panel show surface ozone simulated in NYC and at the location of the MDA8 ozone maximum downwind of NYC (max).

4.3.8 MDA8 ozone simulations during the July 16 exceedance

The exceedance on July 2, 2018 reflects a case study where onshore winds transported the NYC plume to the northwest (77). Previous studies have shown that pollution from NYC and upwind sources is often transported over coastal New England, which may result in ozone exceedances in Long Island, coastal Connecticut, and other states in the Northeast (78, 79). Such events were observed during LISTOS and serve as a contrast to the July 2, 2018 case study (77, 80).

Figure S24 shows WRF-Chem simulations for the ozone exceedance observed on July 16, 2018, which was characterized by transport along coastal New England. Surface monitors showed that MDA8 ozone reached 65-70 ppb in NYC, and as high as 85 ppb downwind at sites along the Long Island Sound. Downwind of NYC, MDA8 ozone peaked near Westport, CT (max in Fig. S24), which was coincidentally within a few kilometers of the LMOL measurements (see Section 4.3.4).

WRF-Chem generally reproduces the spatial pattern of ozone downwind of NYC. WRF-Chem underpredicts upwind ozone produced from the outflow of Philadelphia and other upwind urban centers, which is likely the result of an overprediction in the PBL in the Philadelphia region. Despite these challenges, the meteorology in the NYC region is reasonably captured by the

model. In WRF-Chem, the simulated PBL over NYC is within ~10% of the ceilometer measurements at CCNY (Fig S14). Ozone mixing ratios within the NYC plume are also well represented. At Westport, CT (the location of "max" within the modeling domain), the LMOL reported average ozone of ~84 ppb within 2.5 km of the surface during peak photochemistry (12:00 - 16:00 EST). WRF-chem ozone averaged over the same vertical extent was ~86 ppb.

We analyze the ozone produced within the NYC plume on July 16 in order to compare to the trends observed on July 2. On July 16, BVOCs + NO_x was the largest contributor to ozone produced within our modeling domain (Fig. S24, panel A), which is similar to the results presented for July 2. Between NYC and the MDA8 ozone maximum over Connecticut, biogenic VOCs reacted alongside NO_x to enhance ozone by 14 ppb. Panel (B) shows simulations when fossil fuel VOCs are included. In this case, ozone in NYC increases to 61 ppb in NYC (an increase of 3 ppb) and 75 ppb at the ozone maximum (an increase of 4 ppb). The addition of VCPs (panel C) increases ozone further to 63 ppb in NYC (an increase of 2 ppb) and 82 ppb at the ozone maximum (an increase of 6 ppb). In total, AVOCs contributed ~ 5 ppb to ozone produced in NYC, and ~10 ppb to ozone produced at the MDA8 ozone maximum over Connecticut. Of this anthropogenic fraction, VCPs were responsible for ~40% of the ozone produced in NYC, and ~60% of the ozone produced at the MDA8 ozone maximum.

The ozone attribution estimated for July 16 is similar to the modeled ozone distributions described for July 2. These results demonstrate that VCPs are likely to play an important role in ozone exceedances observed during outflow events that typically affect the air quality in coastal communities along the Northeast US.

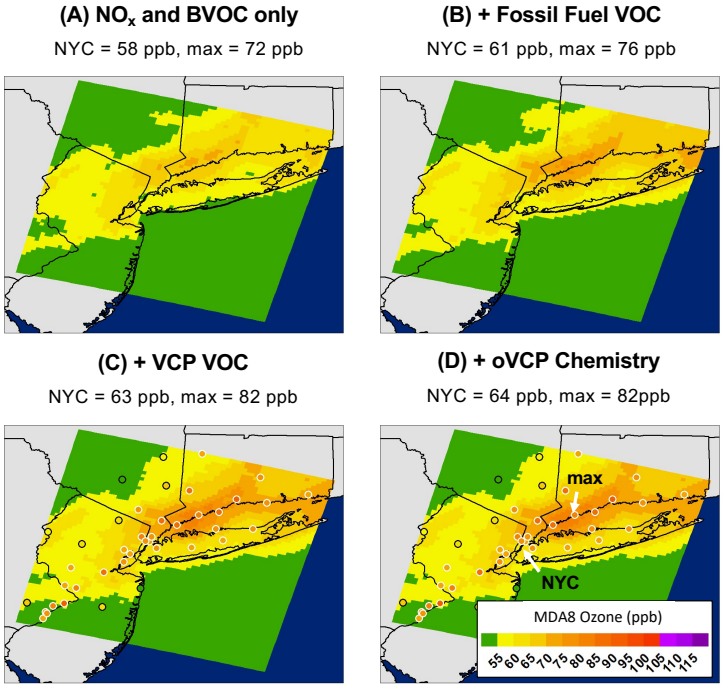

Fig. S24. WRF-Chem simulations of MDA8 ozone for the ozone exceedance on July 16, 2018. Shown are simulations for (A) global background + NO_x and BVOCs, (B) results from (A) with mobile source VOCs added, and (C) results from (B) with VOCs from VCPs added. Panels A-C show ozone produced under the assumption of hydrocarbon chemistry. Panel (D) shows the simulation using full emissions, but under the assumption of oVCP chemistry. Circles show ozone mixing ratios measured at monitoring stations in the NYC area; those bolded in white exceeded US NAAQS. The numbers above each panel show surface ozone simulated in NYC and at the location of the MDA8 ozone maximum downwind of NYC (max).

5. Description of Lagrangian box model

A 0-D box model, built and executed using the Framework for 0-D Atmospheric Modeling (F0AM, 81), is employed to complement the WF-Chem simulations. Box models require fewer computational resources and can provide insights into important chemical processes. Here, we develop a box model in order to estimate the contributions of VCPs and mobile source emissions to the anthropogenic ozone enhancements observed downwind of NYC. We also evaluate isopleths in order to assess ozone responses to changes in NO_x and total VOC emissions. In the following sections, we describe the box model, evaluate model performance against WRF-Chem, and describe simulations aimed at evaluating ozone sensitivities.

5.1 Box model setup

We construct the box model to represent NYC pollution as a Lagrangian plume, which generally agrees with the representation inferred from WRF-Chem simulations. Figure S25 shows WRF-Chem trajectories and demonstrates that air over Manhattan during the July 2, 2018 ozone episode was transported northward to the region of high ozone near Spring Valley, NY (hatched circle). A schematic of the box model framework is shown in Fig. S26. The box volume is assumed to be equivalent to the area of Manhattan (12 km x 5 km) with a height equivalent to the planetary boundary layer (PBL) measured by LIDAR over CCNY during the 2018 LISTOS campaign (Fig. S27). To simplify the model, the chemistry is evaluated during midday when the boundary layer is fully developed and dilution effects due to boundary layer expansion can be neglected. Here, the model is initialized at 11:00 AM when the boundary layer is expected to have grown to ~ 1.2 km. It is assumed that the box volume remains stable over the course of a 6-hour simulation, which is consistent with the lidar measurements conducted during LISTOS (Fig. S27).

It is assumed that the only processes contributing to the transformation of chemical species are by chemical reaction and dilution with background air, as described by Equation 2.

$$\frac{\mathrm{dC}}{\mathrm{dt}} = \mathrm{r}_{\mathrm{formation}} - \mathrm{r}_{\mathrm{consumption}} - \mathrm{k}_{\mathrm{dil}}(\mathrm{C} - \mathrm{C}_{\mathrm{b}}) \quad (2)$$

Where C is the concentration of given species, r is the set of reactions that describe chemical transformation, k_{dil} is the plume dilution rate, and C_b is a regional background concentration. The plume dilution rate is estimated based on the evolution of CO observed in WRF-Chem trajectories 5 and 6 (Fig. S25). For base case simulations, the dilution rate is estimated to be 0.02 - 0.03 hr^{-1}, which is lower than dilution rates observed in other cities 0.1 - 0.2 hr^{-1}, (82) and likely reflects the stagnant conditions observed during the July 2 ozone event.

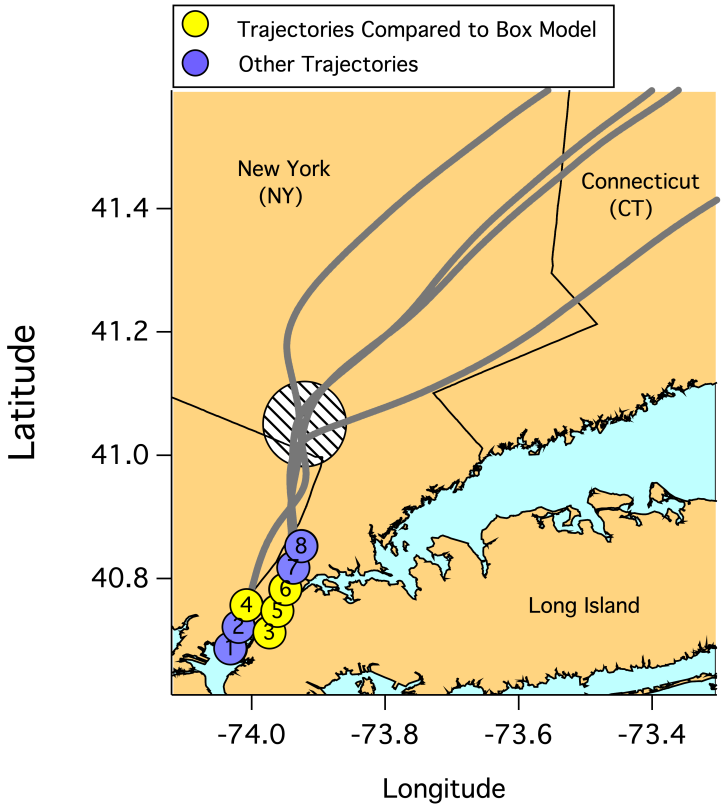

Fig. S25. WRF-Chem trajectories initialized at grid cells located over Manhattan. The trajectories begin at 11:00 AM on July 2, 2018 and project forward over 8 hours. The hatched circle shows the region of peak ozone production simulated by WRF-Chem (Fig. 3, main text). Shown are the trajectories that are compared to box model results (originating from the yellow circles).

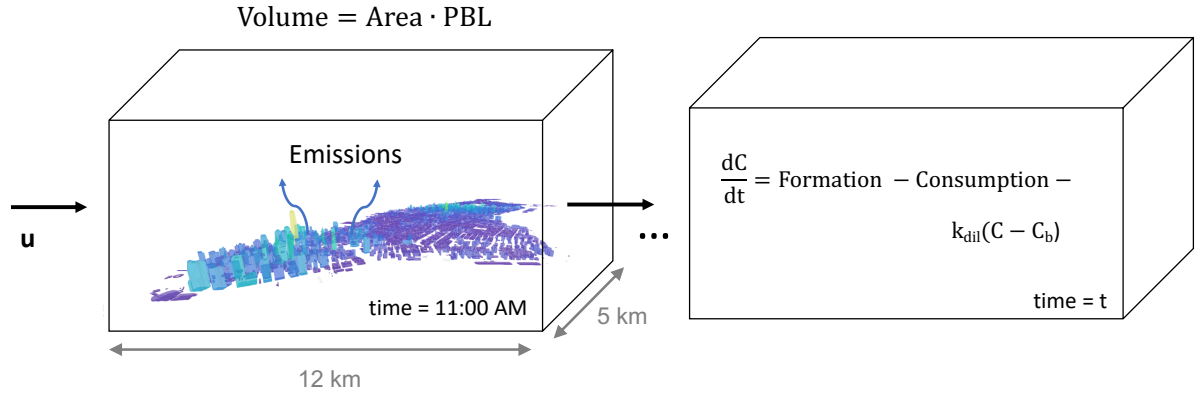

Fig. S26. Schematic showing the basic setup of the Lagrangian box model analysis. The chemical mechanism for this analysis is assumed to be RACM-ESRL (46), and the emissions are based on the inventory described in Section 3.

Reaction rates are determined based on the chemical mechanisms used in WRF-Chem simulations (i.e., RACM-ESRL and RACM-ESRL-VCP). The photolysis rate constants, temperature, pressure, and relatively humidity are constrained based on hourly WRF-Chem output at 750 m over the CCNY ground site. Initial mixing ratios of VOCs, NO_x, and CO are calculated using the emissions inventory described in Section 3. It is assumed that the emissions are injected into the box, then fully mixed within the volume over Manhattan. In order to represent

the urban VOC and NO_x mixture at 11:00 AM, the emissions are scaled by the diurnal patterns employed in WRF-Chem and presented in Fig. S27. For most source categories, it is assumed that VOC emissions follow a weekday diurnal pattern that peaks during working hours. In contrast, weekday emissions of personal care products have been shown to peak in the morning (6:00 - 7:00 AM) and decrease exponentially over the course of a day (30). The same assumptions are applied to the personal care product emissions used for NYC simulations.

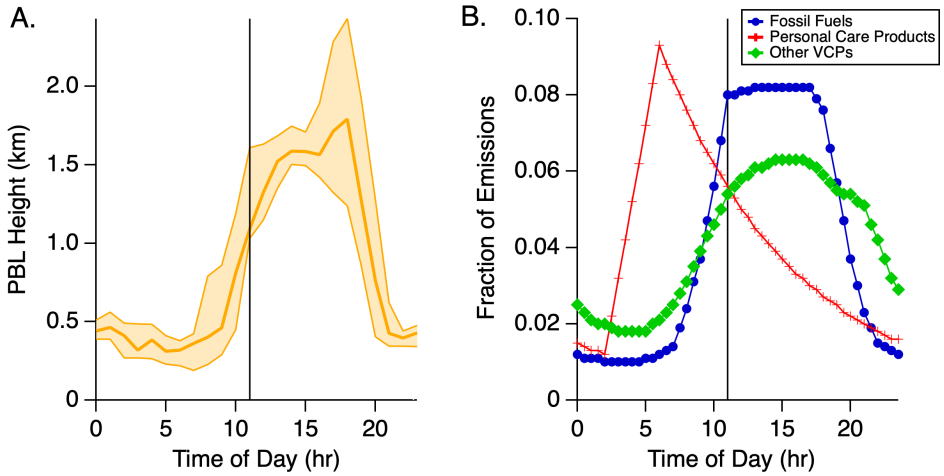

Fig. S27. (A) LIDAR measurements of planetary boundary layer height during the 2018 LISTOS campaign. (B) Diurnal emission profiles applied to the box model for fossil fuels (gasoline exhaust, gasoline evaporation, diesel exhaust, and other fossil fuels), personal care products, and other VCP categories (cleaning, pesticides, and coatings). The black line shows the time when the Lagrangian box model is initialized (11:00 AM).

NO_x emissions are injected into the box then partitioned to NO and NO_2 assuming that both species are at pseudo-steady state with ozone. The initial NO_x mixture is 80% NO_2 and 20% NO. Initial ozone concentrations are prescribed based on July 2, 2018 observations at 11:00 AM (70 ppb). OH concentrations are initialized to 6 x 10^6 molecules cm^{-3}, which is the approximate concentration produced shortly after initializing the simulation.

Biogenic emissions have an important impact on ozone production downwind of NYC and other eastern U.S. cities (83). Mobile drives across the NYC metropolitan area show that isoprene is relatively constant at ~ 0.75 – 1 ppb (Fig. S17A). To account for biogenic contributions to ozone production and plume reactivity, we constrain isoprene mixing ratios to 750 ppt for the entire box model simulation. This differs from WRF-Chem simulations which spatially distribute isoprene emissions based on biogenic emission inventories. Despite this simplification, the box model constraint reasonably accounts for ozone produced from biogenic sources. Panel F in Fig. S28 shows WRF-Chem and box model output when anthropogenic VOCs are turned off and isoprene is constrained to 750 ppt ± 10% ("No Anthro."). Between both models, ozone formed from isoprene + NO_x chemistry agrees to within 20%. We note that biogenic monoterpene emissions are also present downwind of NYC; however, we ignore these emissions since they represent a small fraction of total biogenic emissions (< 10%).

The box model is diluted with background air as described by Equation 2. For most species, it is assumed that regional background mixing ratios are negligible compared to the NYC plume. Exceptions include CO, formaldehyde, and small hydrocarbons (e.g., ethanol, methanol,

propane). For these species, we estimate background mixing ratios based on WRF-Chem output outside the NYC plume.

5.2 Box model comparisons to WRF-Chem trajectories

Figure S28 shows a comparison between the box model and WRF-Chem output along the trajectories presented in Fig. S25. Here, we compare simulations employing RACM-ESRL-VCP. Shown are the four WRF-Chem trajectories that passed through the region of maximum ozone downwind of the NYC. The WRF-Chem trajectories were initialized at 11:00 AM in order to compare with the box model results.

The two models agree to within 10% for ozone and NO_x. Initial CO and NO_x mixing ratios differ among the various trajectories, in part because WRF-Chem emissions are distributed throughout Manhattan based on traffic and population density. For some WRF-Chem trajectories, CO, VOCs, and NO_x increase shortly following initialization. For example, CO mixing ratios increase in trajectories 3 and 4, likely due to the accumulation of combustion emissions while moving northward. We note that trajectories 5 and 6 generally pass through regions of relatively low population density downwind of Manhattan. As mentioned previously, the model dilution rate was adjusted to match these profiles.

Also shown are the profiles for several hydrocarbon categories - HC3, HC8, TOL, EOH, and PROG. HC3 is predominantly influenced by mobile source alkanes, HC8 includes a wide range of hydrocarbon emissions from both mobile and VCP sectors, TOL predominantly reflects fossil fuel aromatics, and EOH and PROG describe ethanol and glycols. In general, the two models agree to within 30% for HC8, HC3, TOL, and PROG, and within 40% for EOH. Similar to CO and NO_x, VOC mixing ratios increase along WRF-Chem trajectories 3 and 4, which may reflect accumulation of VCP or mobile emissions while moving northward.

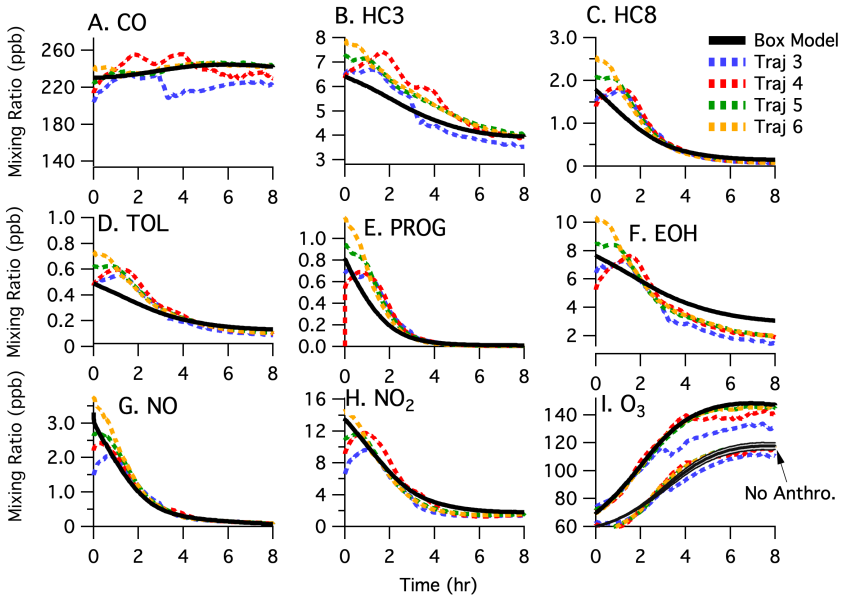

Fig. S28. Comparison of box model simulations to the WRF-Chem output along the trajectories presented in Fig. S25. Shown are comparisons for simulations conducted with biogenic and anthropogenic emissions. For ozone (panel F), simulations conducted with ("Full Emissions") and without ("No Anthro.") anthropogenic VOC emissions are shown. The "No Anthro." box model simulation assumes a constant isoprene concentration of 1±0.1 ppb.

5.3 Box model evaluation of VOC contributions to anthropogenic ozone formation

Fig. S28 demonstrates that box model and WRF-Chem are in good agreement. In the following discussion, we leverage the box model to evaluate ozone sensitivities to total VOC, NO_x, and speciated VOC emissions.

Simulations were conducted to assess the amount of ozone produced from each VOC in the emission inventory (total = 1600). For each simulation, emissions of a single species were set to zero, and the resulting change in ozone was compared to the base case simulation. The impacts of VOC emissions from a single source category were assessed by decoupling VOC contributions from multiple sources. For example, ethanol associated with VCPs was turned off independently from ethanol resulting from gasoline exhaust, gasoline evaporation, and diesel exhaust. The total sum of ozone changes is defined as "anthropogenic ozone", as described by Equation 3.

$$\text{Anthropogenic Ozone} = \sum_i^{1600} \text{Ozone}_{\text{Base Case}} - \text{Ozone}_{\text{Species}_i=0} \qquad \text{Equation 3}$$

In this study, we evaluate the yield of anthropogenic ozone and other secondary pollutants (e.g., formaldehyde, PAN, and organic nitrates) from fossil fuels, VCP emissions, and sub-categories within VCPs (Fig. 4, main text). The yield of a secondary pollutant (X) is calculated following Equation 4.

$$\text{Yield} = \frac{\Delta X}{\Delta VOC} \quad \text{or} \quad \frac{\sum_i \Delta X_i}{\sum_i \Delta VOC_i} \qquad \text{Equation 4}$$

Where the first equation represents the yield for a single ozone precursor, and the second represents the yield associated with an entire emission category. The change in mass of species X is calculated as the amount produced when the NYC plume reaches the location of the MDA8 ozone maximum highlighted in Fig. S25. The change in VOC is calculated as the mass that was reacted away once the plume reaches the MDA8 ozone maximum.

Several sensitivity studies were conducted to assess the extent to which meteorology, dilution, biogenic emissions, and NO_x/VOC ratios impact the relative distribution of anthropogenic ozone production (Table S7). Broadly, the contribution of emission sectors to anthropogenic ozone formation varied by less than 5%.

Table S7. Summary of analyses conducted to evaluate box model sensitivity to meteorology, dilution, biogenic emissions, NO_X/VOC ratios, and fragrance emissions.

Sensitivity Case	Range of values tested
k_{dil}	0.025 s^{-1} (base), 0.1 s^{-1}
PBL	1200 m (base), 1800 m, 900 m
NO_x Emissions	base, base/2
VOC Emissions	base, base/2
Isoprene Constraint	0.75 ppb (base), ±10%, ±50%

5.4 Box model evaluation of ozone sensitivities towards NO_x and VOC emissions

WRF-Chem sensitivity analyses shown in Fig. 3 (main text) suggest that ozone production downwind of NYC was, in part, sensitive to the concentration of anthropogenic VOCs. Ozone production is strongly dependent on NO_x emissions, but the relative balance between anthropogenic VOCs, biogenic VOCs, and NO_x can lead to differences in NO_x and VOC-sensitivity. Here, we leverage the box model to calculate changes in ozone downwind of NYC assuming a 50% decrease in NO_x or VOC emissions. This analysis is intended to assess the extent to which photochemical ozone production downwind of NYC was NO_x or VOC-limited.

The ozone sensitivity analysis for the July 2 ozone episode is shown in Fig. 5 (main text). The background colors show when ozone production transitions from NO_x-saturated and VOC-limited ($\frac{dO_3}{dNO_x} < 0$) to NO_x-limited ($\frac{dO_3}{dNO_x} > 0$). Shown is the base case assuming a constant isoprene mixing ratio of 750 ppt. Additional calculations were performed assuming 10% and 50% changes to the isoprene constraint. in Fig. 5. All calculations were performed for a box model time of 2.5 hr, which corresponds to the time that the NYC plumes passed over the WRF-Chem MDA8 maximum.

Supplemental Discussion

6. Evaluation of anthropogenic monoterpene emissions

In the main text, we show that monoterpenes measured in Manhattan during winter and summer were emitted from anthropogenic sources (Fig. 2). Anthropogenic monoterpenes are a significant source of reactive carbon in urban environments and are shown to be emitted at significant rates. Below, we show that the monoterpene distributions measured in Manhattan most resemble those from fragranced consumer products and indoor air, and that the anthropogenic monoterpene budget is best described by emissions from fragranced VCPs, pine oils, and emissions from building materials.

6.1 Comparison of urban monoterpene distributions to VCP headspaces, indoor air, and biogenic monoterpene measurements

Figure S29 shows the speciation of monoterpenes in major classes of fragranced consumer products, including personal care products, laundry detergents, cleaning agents, and air fresheners. A key feature of VCPs is that limonene is the dominant monoterpene (~55%), followed by other terpenes/terpenoids (~30%) and pinenes (~15%).

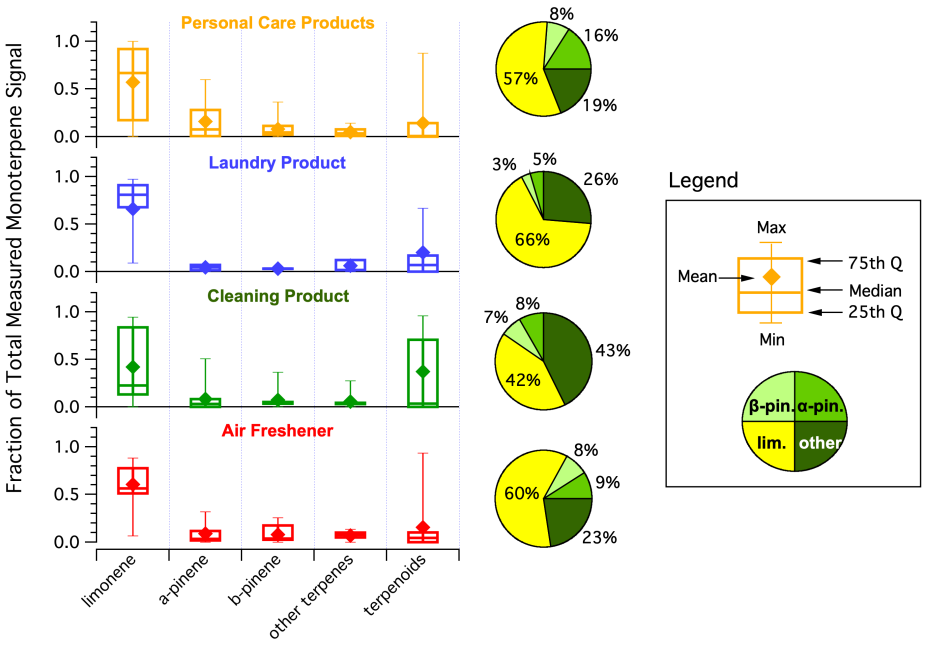

Fig. S29. Head space monoterpene distributions reported by Steinemann et al. *(84, 85)* for personal care products, laundry products, cleaning products, and air fresheners.

The monoterpene distribution measured in Manhattan (Fig 2) is similar to those shown in Fig. S29. Likewise, the Manhattan distribution also resembles those observed in indoor air (Fig. S30) (86-88). Indoor mixing ratios of monoterpenes largely result from emissions from VCPs and building material off-gassing (e.g., wood structures) (86-88). VCPs emitted indoors will exchange with outdoor air and contribute to ambient VOC mixing ratios(28, 30). The high proportion of limonene in Manhattan suggests that the emissions primarily result from anthropogenic sources.

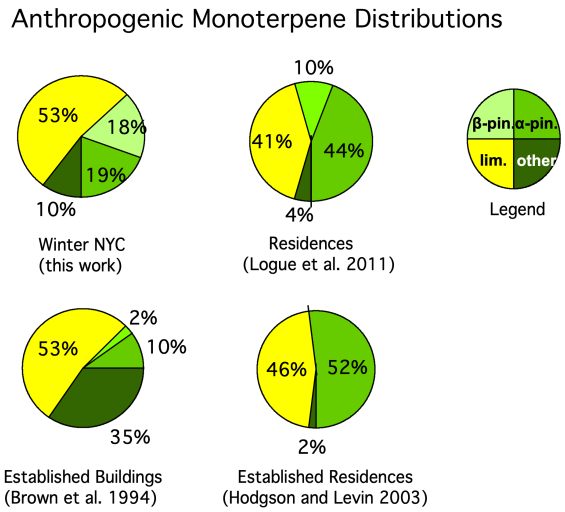

Fig. S30. Monoterpene distribution measured in NYC during winter (top left) compared to the monoterpene distributions measured from indoor air of a variety of building types *(86-88)*. Limonene is enriched in NYC, which is consistent with the monoterpene distributions measured in indoor air.

In contrast to the VCP distributions, biogenic sources of monoterpenes are dominated by pinenes. Figure S31 shows the speciation of terpenes measured by the mobile laboratory in northern New Jersey, as well as the distribution expected from pitch pine, a common monoterpene-emitting tree found in the Eastern US. The dominance of pinenes is confirmed by our mobile laboratory measurements in outlying suburbs located in New Jersey. The contrast between the biogenic distribution measured outside of NYC with those measured in Manhattan again point to the significant influence of anthropogenic emissions on urban monoterpene mixing ratios.

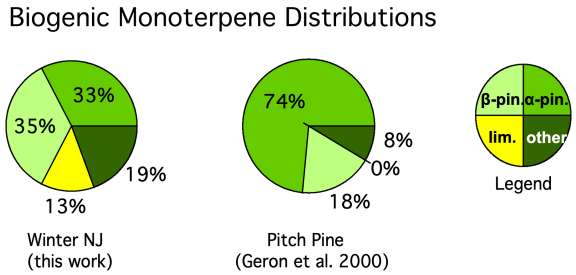

Fig. S31. Monoterpene distribution measured in New Jersey during winter compared to the monoterpene speciation reported for the dominant tree species in northern New Jersey (89). In forested regions, limonene is only a small fraction of the total monoterpene emissions.

6.2 Estimation of total anthropogenic monoterpene emissions in Manhattan

Anthropogenic monoterpene emission rates are not readily reported in the literature. To estimate monoterpene emissions in Manhattan, we apply two methodologies. First, we use FIVE-VCP inventory estimates of CO and multiply these emissions against the monoterpene/CO ratios measured in Manhattan during winter. Second, we scale monoterpene emissions represented in WRF-Chem to match the mobile laboratory measurements of monoterpenes sampled across NYC during summer. These two methods provide an estimate in the range of emissions that can

be compared against speciated FIVE-VCP estimates of fragrances (described further in Section 6.3).

During a wintertime stagnation event, monoterpenes and CO were highly correlated (Fig. S5), and we calculate a monoterpene/CO enhancement ratio of 4.2 g/kg (Table S2). This ratio accounts for the differences in reactivity between monoterpenes and CO under modeled wintertime oxidation conditions (see Section 3.1). In Section 3, we validated the FIVE-VCP inventory against CO fluxes measured by aircraft during winter (Fig. S9) and VOC/CO ratios measured at the CCNY ground site by PTR-ToF-MS and GC-MS (Fig. S10). We multiply the CO emissions calculated over Manhattan (212 t d^{-1}) by the monoterpene/CO enhancement ratio (4.2 g/kg) and normalize this to the population of Manhattan (~1.7 million people) to estimate a total monoterpene flux of 520 mg $person^{-1}$ d^{-1}.

This estimate applies to anthropogenic monoterpene emissions during winter when biogenic emissions are at a minimum. To estimate monoterpenes during summer, we leverage our WRF-Chem simulations, which accounts for greater biogenic emissions during summer and greater losses of monoterpenes to atmospheric oxidation. We tune WRF-Chem simulations to include anthropogenic monoterpene emissions and compare model results to mobile laboratory transects across the NYC region. Figure S17C shows model sensitivity analyses in the presence and absence of anthropogenic monoterpenes. Even during summertime, biogenic sources cannot explain the peak monoterpene emissions observed in the densely populated regions of NYC. The observations are reproduced in simulations that include anthropogenic monoterpene emissions equivalent to 860 mg $person^{-1}$ d^{-1}.

While this emission rate is higher than that estimated for winter, these differences may reflect seasonality in the emissions of fragranced VCPs, or uncertainties due to the losses of monoterpenes to OH and ozone. Gkatzelis et al. (90) investigated the seasonality of VCP tracers in Manhattan, including D5-siloxane and monoterpenes. D5-siloxane enhancement ratios were higher in summer than in winter, suggesting greater use of personal care products during warmer months. D5-siloxane is predominantly removed from the atmosphere by reaction with OH and has an atmospheric lifetime that is significantly longer than the ventilation rate in NYC (atmospheric lifetime ~4 days under typical OH concentrations (30, 91, 92)). Consequently, the differences observed in Manhattan reflect changes in emissions rather than seasonality in OH oxidation. Gkatzelis et al. (90) reported higher monoterpene enhancement ratios in winter than in summer, but attributed this to differences in chemical lifetime. Our box modeling results described in Section 3.1 show that monoterpene losses are significant during winter (~50% loss) and greatest during summer (70-90% loss) under typical air exchange rates in NYC (Fig. S6). These results agree with the conclusions drawn by Gkatzelis et al. (90), and demonstrate that oxidation processes can significantly alter emission rate estimates for highly reactive VCP emissions.

Here, we bound our estimates of anthropogenic monoterpenes emissions to 520 - 860 mg $person^{-1}$ d^{-1} based on our winter and summertime estimates.

6.3 Inventory estimates of monoterpene emissions from fragranced VCPs

Monoterpenes from VCPs are commonly associated with fragrance mixtures (84, 85), air fresheners (93), and pine oils (93) in personal care products and cleaning agents. Here, we refer to monoterpenes found in consumer products collectively as “fragrances”. Minimal fragrances are found in coatings, inks, adhesives, and pesticides. McDonald et al. (28) estimated that per capita

use of fragrances in the US is ~1.4 g/d. Here, we perform a more detailed accounting of the amount and distribution of monoterpenes in fragrances.

In emissions inventories, VCP sources of monoterpenes are listed explicitly as d-limonene and α-pinene (~30 mg/person/d), as "pine oil" (~60 mg/person/d), or mainly as "fragrances" (~1300 mg/person/d). For an emissions inventory of Los Angeles, McDonald et al. (28) treated fragrances as predominantly composed of monoterpenes. However, the California Air Resources Board (CARB) recently conducted an industry survey of fragrance mixtures (94). Of the speciated mass, lower vapor pressure VOCs (e.g., glycols) were the largest fraction (~55%), followed by monoterpenes (~15%), esters (~15%), and other aldehydes and ketones. However, a significant fraction of the mass remains unresolved. To augment the CARB survey, we have performed gas chromatographic analyses of five commercially available fragrance mixtures (VOC composition summarized in Table S8).

For identification of fragrance components, 1 μL aliquots of 50,000x diluted fragrances (~20 ng/μL in dichloromethane) were injected manually into the into the heated inlet of a GC-MS. Analytes were separated on a non-polar column (DB-5, 30m x 0.25 mm x 0.25 μm) and detected using a unit-mass resolution electron ionization quadrupole mass spectrometer. All listed analytes had mass spectra that agreed with the NIST mass spectral library with a match value greater than 850 indicating a high probability of accurate identification. In addition, an *n*-alkane standard was run to corroborate identifications based on retention indices. The density of each fragrance was also determined gravimetrically, with an average of 1030 g/L for these five fragrances. Any siloxanes observed were attributed to column bleed and were not documented or quantified.

Identified components were quantified by separate analysis using a GC with a flame ionization detector (FID), with which detector response can be accurately (within ~10%) estimated for any component with a known structure. For quantification, each fragrance was diluted in dichloromethane separately (i.e., not serially) to three concentrations (nominally 10, 25, and 50 ng/μL), each of which was analyzed in triplicate by GC-FID using an autosampler for injection of 1 μL aliquots (i.e., 9 samples per fragrance, representing three different concentrations). GC operating parameters were the same as those used for identification, allowing analytes to be robustly identified by their retention times. Detector response was calibrated using an *n*-alkane standard, with each identified analyte quantified based on the nearest eluting alkane, then corrected based on its expected FID detector response calculated by the structure-activity relationship of Scanlon and Willis (95). To test the validity of this quantification method, a tracking mixture with known amounts of analytes (e.g., limonene, toluene, diethyl phthalate, etc.) was injected and the experimental quantification matched injected amounts to within 10%, except for high-volatility oxygenates such as hydroxyacetone (for which uncertainty is around 30%). All data analysis was performed using the freely available TERN chromatographic software package (96) in the Igor Pro programming environment (Wavemetrics, Inc.) Mixing ratios for the observed compounds are expected to be accurate to within 15% based on propagated error from calibrations, uncertainty in FID response factors, and uncertainty in dilution ratios.

On average, ~10% of the fragrance mixture mass is classified as monoterpenes or terpenoids with the largest species being limonene. These results are generally consistent with the CARB fragrance survey (94). Assuming fragrance mixtures are ~10% monoterpenes, and adding inventory contributions from limonene, α-pinene, and pine oil, we estimate overall terpene emissions from VCPs at 220 mg/person/d.

Table S8. Summary of five fragrance mixtures analyzed by GC-MS.

Compound	Mix 1 (g/L)	Mix 2 (g/L)	Mix 3 (g/L)	Mix 4 (g/L)	Mix 5 (g/L)	Avg (g/L)
diethyl phthalate	--	316	--	47	667	206
triethyl citrate	--	--	625	--	--	125
benzyl benzoate	--	--	--	385	--	77
hedione	83	244	--	32	--	72
d-limonene	65	--	105	85	50	61
galaxolide	22	159	--	14	--	39
linalool	61	--	--	--	27	18
peach lactone	--	--	--	84	--	17
linalyl acetate	73	--	--	--	--	15
hexyl acetate	--	--	--	42	--	8
benzyl salicylate	--	--	--	40	--	8
vertenex	--	--	--	--	18	4
dihydromyrcenol	--	--	--	--	16	3
β -pinene	--	--	--	--	--	1
∑(terpenes) =	126	0	105	85	77	95

Note: Underlined and bolded compounds are classified as monoterpenes or terpenoids.

The estimated flux of monoterpenes from fragranced VCPs is lower than the total emissions of anthropogenic monoterpenes estimated for Manhattan (520–860 mg person^{-1} d^{-1}). The remaining mass is likely associated with other anthropogenic sources, including food consumption (cooking + citrus use) or off-gassing of building materials. Wood combustion could contribute to monoterpene emissions, especially during winter. However, monoterpene emission factors from wood combustion are small (97) and monoterpenes measured in NYC do not exhibit a strong correlation with compounds largely associated with residential wood burning (e.g., furfural, R2 ~ 0.3, 98). In NYC, most heating of residential/commercial buildings is by natural gas. Therefore, monoterpene emissions from wood burning are likely negligible.

Building materials can be a significant source of α- and β-pinene (99) and indoor concentrations of monoterpenes in occupied or unoccupied homes can range between 15 - 40 μg/m^3 (88). If we treat lower bound observations as representative of monoterpene concentrations of unoccupied homes, and use the Manhattan building volume (1.1 x 10^7 m^3, found at: https://www1.nyc.gov/site/doitt/residents/gis-3d-data.page), a typical air exchange rate of ~1 per hour (or ~24 per day) (100), and a population of ~1.7 million people, we estimate a 1st-order monoterpene emission rate of ~240 mg person^{-1} d^{-1} from building materials. While further work is needed to evaluate the exchange between indoor and outdoor air, this emission rate could be comparable to monoterpene emissions from fragranced VCPs.

7. Spatial distribution of ethanol in NYC and across the US

Ethanol was one of the most abundant VOCs measured in NYC and other cities across the US (> 10 ppb in NYC). In the US, gasoline is enriched with ethanol to 10% by volume, resulting in large fossil fuel emission factors (25, 34). The large burden of ethanol in the US has been

traditionally linked to emissions from fossil fuels (101). Recently, it has been shown that VCP emissions significantly contribute to ethanol mixing ratios in Los Angeles(28). In this study, the FIVE-VCP shows that 70% of the ethanol emitted in NYC is due to VCP emissions, while 30% comes from fossil fuels (Fig. S10).

The spatial distribution of ethanol across the NYC metropolitan area also points to the significant influence of VCP emissions on urban ethanol mixing ratios. Figure 31A shows NOAA mobile laboratory measurements throughout the NYC region. The drive tracks are colored by ethanol, and the bars show median mixing ratios measured in binned longitudinal segments. Also shown is the average population density in census tracts located along the mobile laboratory path. The population density data are available at: https://www.census.gov/geographies/mapping-files/time-series/geo/tiger-data.2010.html (last accessed September 2019).

Ethanol is generally enhanced by > 5 ppb in the densely populated regions of NYC compared to lesser populated areas of New Jersey and Long Island. Furthermore, ethanol is well-correlated with the local population density in regions sampled by the mobile laboratory (R^2 = 0.72). The correlation of ethanol with population density is similar to the correlation observed for D5-siloxane (Fig. 2, main text), and significantly higher than for mobile source emissions (Fig. S32, R^2 < 0.05).

As described in the main text, we calculate VOC enhancement ratios to benzene to evaluate the relationship between VCPs, traffic emissions, and urban population density. Figure S32B demonstrates that ethanol enhancement ratios are well-correlated with urban population density for cities across the US. In Section 8, we show that enhancement ratios of mobile source VOCs, such as toluene and C8-aromatics, do not correlate with urban population density. The difference between these relationships further illustrates the significant impact of VCPs on urban emissions of ethanol.

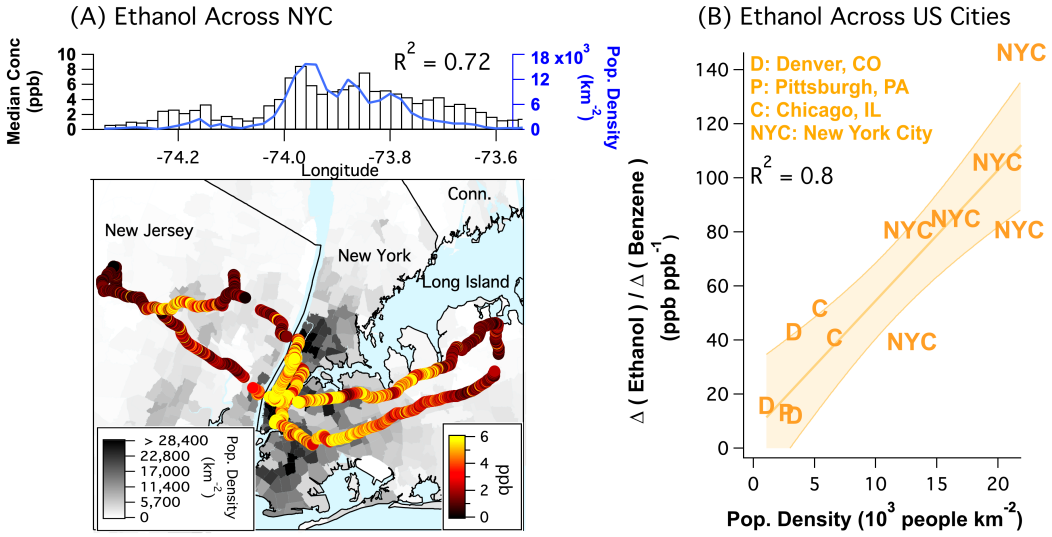

Fig. S32. (A) Drive track through NYC colored by ethanol in winter 2018 on top of a population density map. The bars above the map show the median concentrations of ethanol longitudinal bins, together with the average population density (blue trace). (B) Ethanol/benzene enhancement ratios measured in cities across the US.

8. Spatial distributions of mobile source VOCs in NYC and across the US

Benzene is a known marker for traffic emissions (102). Unlike monoterpenes, D5-siloxane, and ethanol, benzene and other traffic markers, such as CO, did not exhibit a strong correlation with population density in NYC. Figure S33 shows the spatial distribution of benzene and CO measured by the NOAA mobile laboratory across the NYC metropolitan area. The drive tracks are colored by benzene and CO mixing ratios, and the bars at the top of each panel show median mixing ratios measured in binned longitudinal segments. The blue trace shows the population density in the regions sampled by the mobile laboratory, also binned into longitudinal segments.

While mobile and combustion sources are ubiquitous across the NYC metropolitan area, there is not a strong correlation between population density and median mixing ratios of benzene and CO (R^2 < 0.05). This is in contrast with the spatial distribution observed for D5-siloxane, anthropogenic monoterpenes, and ethanol (Figures 2 and S32), which were strongly correlated to population density during winter (R^2 > 0.6). As described in the main text, these observations are consistent with the expectation that VCP usage should scale with the population, whereas mobile emissions will be limited by road volume capacity (103-105).

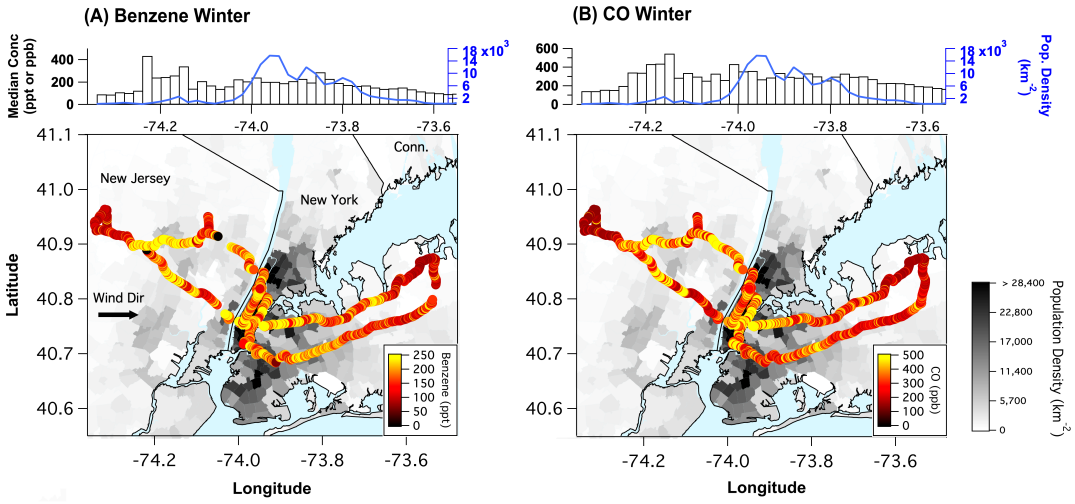

Fig. S33. Drive track through NYC colored by benzene (mobile source tracer) and CO (combustion marker) in winter 2018 on top of a population density map. The bars above each map show the median concentrations of benzene and CO over longitudinal bins, together with the average population density (blue trace).

In contrast to the VCP tracers described in the main text, urban enhancement ratios for aromatic compounds were poorly correlated with population density (R^2 < 0.11, Fig. S34). Toluene and C8-aromatics (mostly m,p,o-xylene) are primarily emitted from mobile sources; thus, ratios to benzene are expected to be similar across US cities. C9-aromatics have a relatively larger influence from VCPs and exhibit a weak, but positive, relationship with population density. The contrast between aromatic ERs and those of VCP tracers demonstrate that VOCs emitted from VCPs could be identified in other cities by the relationship with population density.

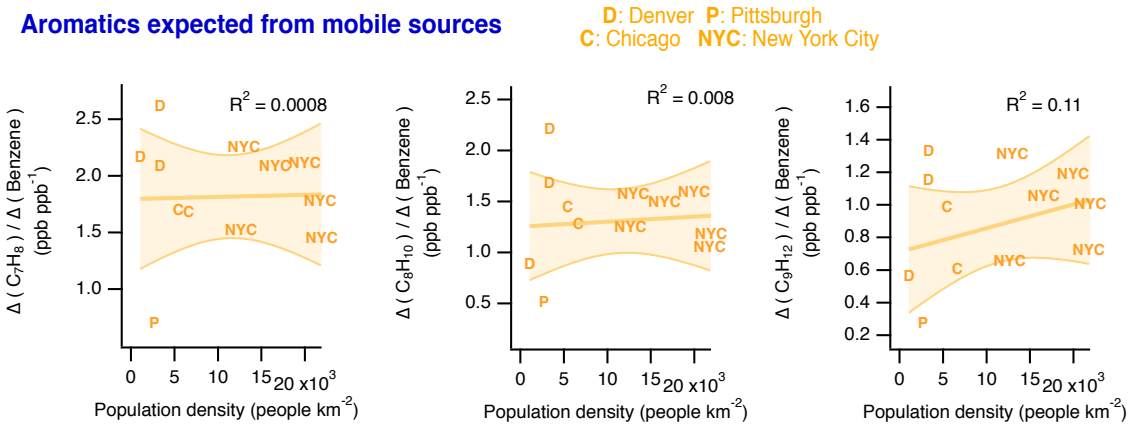

Fig. S34. Population density dependence of aromatic compounds that are co-emitted with benzene from traffic.

9. Evaluation of RACM-ESRL-VCP representation of oVCP emissions and OH reactivity

As described in Section 4.2, oVCP chemistry was added to RACM-ESRL to account for the chemical oxidation of key alcohols and glycols. The resulting mechanism, RACM-ESRL-VCP, explicitly represents the majority of the OH reactivity attributable to oVCP emissions. Figure S35 shows a breakdown of VCP OH reactivity by functional group. Here, we evaluate VCP contributions to OH reactivity following Equation 1.

$$\text{Fraction of VCP OH Reactivity} = \frac{k_{OH} \cdot E_{VCP}}{\sum k_{OH} \cdot E_{VCP}} \quad (1)$$

Where k_{OH} is the reaction rate constant for a given VCP component and E_{VCP} are the daily molar emissions estimated from FIVE-VCP. We evaluate all VCP emissions, but focus on the relative contribution from oVCPs. When available, we utilize published OH rate constants listed in the NIST Chemical Webbook (https://webbook.nist.gov/chemistry/). For oVCPs without published rate constants, we estimate k_{OH} using GECKO-A (http://geckoa.lisa.u-pec.fr/). For non-oxygenated VOCs (e.g., alkanes, alkenes, and aromatics), we use kOH values represented by corresponding surrogates in RACM_ESRL.

Fig. S35 shows that the key species identified in this study (specifically, ethanol, glycerol, propylene glycol, ethylene glycol, and isopropanol) represent ~45% of the molar emissions and > 50% of the OH reactivity attributable to all VCP emission. Of the oxygenated fraction (dark line), which includes fragrances due to the high proportion of glycol solvents, the identified species represent ~70% of the emissions and ~75% of the reactivity.

The glycols represent a large fraction of the VCP emissions (>10%) and OH reactivity (>30%). The CARB 2015 consumer product survey shows that glycerol and propylene glycol are the second and third most commonly used solvents in current consumer product formulations (35). These ingredients are used in personal care products as moisturizers and formulation stabilizers (35), and are also present in many cleaning products. These species are treated as low vapor pressure (LVP) VOCs by CARB (compounds or mixtures with vapor pressure less than 0.1 millimeter of mercury at 20°C), which exempts these compounds from regulatory VOC limits.

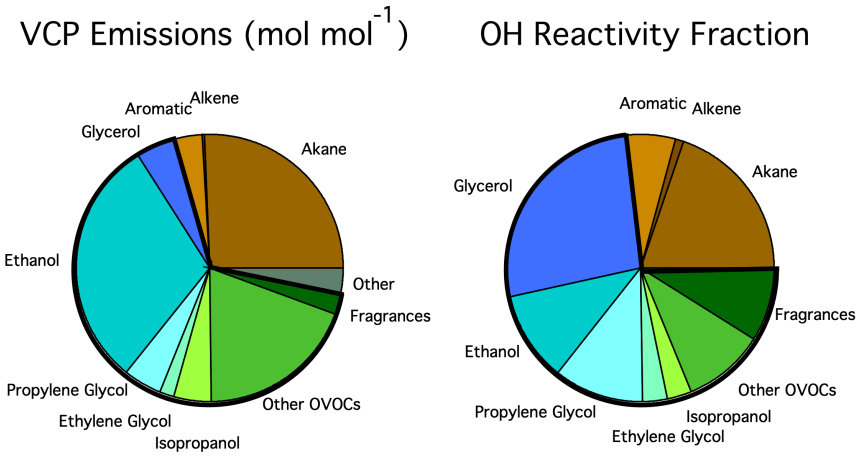

Fig. S35. Breakdown of molar emissions and OH reactivity associated with VCPs in the FIVE-VCP inventory. The dark line highlights the oxygenated emissions from VCPs.

While the atmospheric chemistry of glycols and glycol ethers have been assessed in laboratory chamber experiments (106-109), measurements constraining their emissions are limited. Glycols and glycol ethers are prevalent in indoor air due to the use of cleaning and personal care products (93, 110) and the persistent evaporation from water-based coatings (111, 112). Glycols and glycol ethers have been measured in indoor air at average mixing ratios > 1 ppb (87, 93, 110), which demonstrates that these compounds are volatile and may exchange with outdoor air to contribute to ambient VOC mixing ratios. Given the degree to which glycols contribute to the emissions and reactivity of VCPs, more work is needed to constrain these emissions in ambient air.

10. Comparing hydrocarbon and oVCP OH oxidation mechanisms

In the following discussion, we evaluate the extent to which the chemistry updated in RACM-ESRL-VCP impacts the modeled oxidation of key oVCPs. As discussed in Section 4.2, oxygenates, such as glycols, react differently from their alkane surrogate and can lead to different yields of ozone, as well as other important secondary pollutants, such as PAN, formaldehyde, and organic nitrates. Formaldehyde is observed by satellite remote sensing instruments and is often used as a tool to evaluate OH production and ozone formation processes in remote and urban regions (113, 114), while PAN and organic nitrates are important NO_x reservoirs that can influence ozone sensitivity to changes in chemical regimes (e.g., Fig. 5, main text).

Table S9 summarizes yields (ppb/ppb) of ozone, PAN, formaldehyde, and organic nitrates from the oxidation of ethanol, isopropanol, propylene glycol, and glycerol calculated from box model simulations. These yields are calculated at the MDA8 ozone maximum during the July 2, 2018 ozone episode following Equation 4. Those reported for RACM-ESRL correspond to simulations where the oVCP is treated as its alkane surrogate, while those for RACM-ESRL-VCP correspond to simulations where the oVCP reacts through more complex chemistry that accounts for the reactivity and mechanistic details of the OVOC. We focus on ethanol (EOH), isopropanol (IPOH), propylene glycol (PROG), and glycerol (GLYC) due to the structural differences in the alcohol groups.

Table S9. Yields (ppb/ppb) of ozone, PAN, and formaldehyde calculated at the MDA8 ozone maximum downwind of NYC from box model simulations employing RACM-ESRL and RACM-ESRL-VCP. The ratio of yields (VCP/RACM) are shown to compare yields assuming VCP chemistry (RACM-ESRL-VCP) and hydrocarbon chemistry (RACM_ESRL).

	Ethanol				*Isopropanol*			
	Ozone	PAN	HCHO	ONIT	Ozone	PAN	HCHO	ONIT
RACM-ESRL	1.10	0.05	0.08	0.022	1.22	0.04	0.023	0.05
RACM-ESRL-VCP	1.22	0.12	0.15	<0.001	0.8	0.04	0.12	<0.001
Ratio (VCP/RACM)	1.1	2.5	1.9	---	0.65	1	14.7	---

	Propylene Glycol				*Glycerol*			
	Ozone	PAN	HCHO	ONIT	Ozone	PAN	HCHO	ONIT
RACM-ESRL	1.2	0.03	<0.001	0.18	1.2	0.03	<0.001	0.18
RACM-ESRL-VCP	1.4	0.07	0.1	<0.001	1.76	0.09	0.13	<0.001
Ratio (VCP/RACM)	1.16	3.5	---	---	1.46	4.3	---	---

Ozone yields between the two mechanisms differ, at most, by 50%. These modest changes reflect that ozone production is buffered by a suite of reactions that depend on the rate of RO_2 and HO_2 formation, the reaction of radicals with NO, and NO_y partitioning. The differences are mostly reflected in the rate constants assumed for each species. For example, at 298 K, isopropanol is represented as HC5 in RACM-ESRL with an OH rate constant of 7.7×10^{-12} cm^3 $molec^{-1}$ s^{-1}. However, in RACM-ESRL-VCP, isopropanol is represented by an OH rate constant of 5.2e-12 cm^3 $molec^{-1}$ s^{-1}. This difference in reaction rate results in a ~30% decrease in the rate of peroxy radical production from isopropanol, which is proportional to the decrease in ozone yield between RACM-ESRL and RACM-ESRL-VCP. Other variations in ozone yield are likely due to differences in NO_y partitioning, as described below.

The largest differences between the two mechanisms are reflected by the yields of PAN, formaldehyde (HCHO), and organic nitrates (ONIT). For ethanol, propylene glycol, and glycerol, PAN formation increases by a factor >2 between RACM-ESRL and RACM-ESRL-VCP. HCHO yields are also higher in RACM-ESRL-VCP and vary depending on the species. HCHO yields from glycols are negligible under the assumption of hydrocarbon chemistry (HC8), but are similar to other alcohols when glycol chemistry is represented directly. ONIT yields are highest when treating oVCPs as hydrocarbon surrogates, but are negligible when employing oVCP chemistry.

The differences in formaldehyde between the two mechanisms is largely reflected by the differences in multi-generation chemistry. For example, the ethanol surrogate in RACM-ESRL (HC3) reacts with OH to form a mix of products (primarily ketones and aldehydes), which further oxidize to form formaldehyde at different yields. However, in RACM-ESRL-VCP, ethanol reacts

with OH to form acetaldehyde (ALD), which primarily oxidizes under high-NO_x conditions to yield formaldehyde and PAN. For ethanol, the fate of the first-generation product largely impacts the yield of formaldehyde. This is similar for the other oVCPs represented in RACM-ESRL-VCP.

The differences in PAN and ONIT yields reflect fundamental differences in the OH oxidation of hydrocarbons and oVCPs. For alcohols with primary hydroxyl groups (e.g. ethanol, propylene glycol, and glycerol), reaction with the OH radical will result in the formation of aldehydes and hydroxy ketones(48). Aldehydes react with OH to form peroxyacyl radicals, which readily react with NO_2 to form peroxyacyl nitrates (e.g., PAN). In contrast, OH oxidation of hydrocarbons will primarily result in the formation of ketones or secondary alcohols, which do not react along pathways that lead to the fast formation of PAN. Long-chain alkanes (represented by the HC8 category) form alkyl nitrates (represented by ONIT) at significant yields owing to RO_2 reactions with NO (115). When glycols are treated separately, ONIT yields are negligible since aldehydes and hydroxy ketones do not follow pathways that lead to ONIT formation.

Isopropanol, a secondary alcohol, does not yield significant PAN or ONIT. Isopropanol reacts with OH to form acetone, which slowly oxidizes and does not result in fast PAN formation. These differences in yields highlight the importance of treating species with primary and secondary hydroxyl groups separately to account for differences in aldehyde and ketone formation

11. Evaluation of oVCP chemistry on the modeled budget of formaldehyde, PAN, and organic nitrates

Table S9 demonstrates that the OH chemistries represented by RACM-ESRL and RACM-ESRL-VCP result in different secondary product distributions. In this section, we evaluate the extent to which these chemistries impact the budget of ozone, formaldehyde, PAN, and organic nitrate formation from VCP and mobile source emissions in WRF-Chem and box modeling analyses.

11.1 Box model

We first evaluate the impacts of oVCP chemistry on secondary product distributions using box model simulations. Figures S36 - S39 show ozone, HCHO, PAN, and ONIT yields (gm/gm) calculated at the MDA8 ozone maximum for each emission category represented in the FIVE-VCP inventory. These yields are calculated as described in Equation 4. Solid bars indicate yields calculated using RACM-ESRL chemistry, while checkered bars show yields using RAMC_ESRL_VCP. The bars are colored to show the fraction of each compound produced from different VOC functionalities (e.g., oxygenates, ethanol, fragrances, alkanes, aromatics, and alkenes). The pie charts show the fraction of each compound that is attributable to different emission sectors. We note that this analysis focuses on secondary production of ozone, formaldehyde, PAN, and ONIT from anthropogenic VOCs (AVOCs). Isoprene chemistry significantly contributes to ozone and formaldehyde in the Eastern US (72), and mobile source emissions can be a significant source of primary formaldehyde in urban regions(116, 117).

Figure S36 is analogous to Fig. 4 (main text) and summarizes ozone yields and distributions at the MDA8 ozone maximum. In general, gasoline exhaust is the emission sector that is most efficient at producing ozone, followed by other mobile sources and VCP emissions from inks. These sectors are characterized by VOC profiles with a high content of alkyl aromatics and alkenes. Reactivity scales, such as maximum incremental reactivity (i.e., the mass ozone formed under VOC-limited chemistry per mass of emitted VOC), routinely rank these molecules among the most important ozone precursors to impact urban air (118). In contrast, VCPs are

characterized by a high contribution from alcohol and glycol emissions, which typically rank lower on ozone reactivity scales (118). Despite these lower ozone yields, the mass of VCP emissions, particularly from personal care (18.6 t/d), cleaning (8 t/d), and coatings (12.9 t/d), lead to ozone production that is comparable to that from mobile source VOCs (Figures 3 and 4, main text).

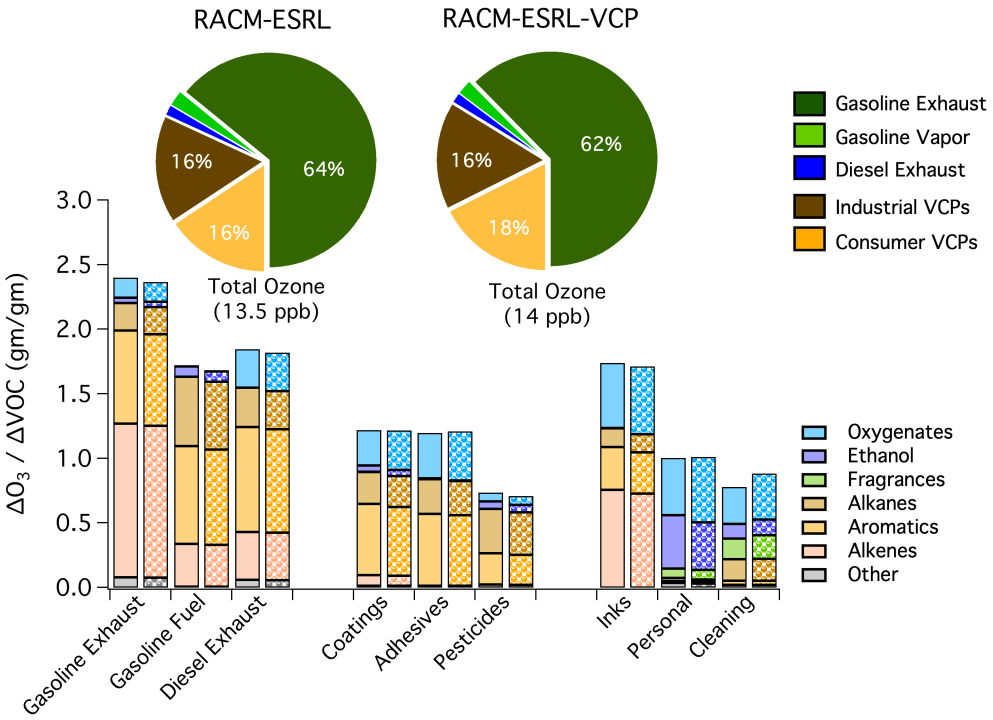

Fig. S36. Yield (bars) and total budget (pie charts) of ozone formed from mobile source and VCP emissions. Solid bars show modeled ozone yields calculated at the MDA8 ozone maximum using RACM-ESRL, while checkered bars show those using RACM-ESRL-VCP. Each bar is colored to show the fraction of ozone resulting from different chemical classes. The pie charts show the fraction of ozone modeled at the MDA8 ozone maximum that results from different emission sources. The numbers below each pie show the total ozone formed from RACM-ESRL (left) and RACM-ESRL-VCP chemistry (right).

Exchanging RACM-ESRL for RACM-ESRL-VCP does not significantly alter ozone yields or the budget of ozone produced at the MDA8 maximum. Total ozone increases by ~0.5 ppb, and the split between mobile sources and VCPs varies by < 2%. As discussed in Section 10, the production of ozone from key oVCPs is largely insensitive to the assumed chemical mechanism (i.e., RACM-ESRL or RACM-ESRL-VCP), in part because the primary OH reactivity is reasonably represented by both mechanisms. This modest difference between the two mechanisms is also reflected in WRF-Chem simulations shown in the main text (Fig. 4).

Figure S37 summarizes the yields and distribution of formaldehyde. Formaldehyde yields are highest for mobile source emissions, such as gasoline and diesel exhaust. Formaldehyde produced from these sectors largely results from the chemistry of light alkenes. VCP emissions with high alkene content (e.g., Inks) also exhibit high formaldehyde yields. In general, emissions sectors with significant oVCP content (e.g., personal care and cleaning) or alkane emissions (e.g., coatings) are among the least efficient at producing formaldehyde.

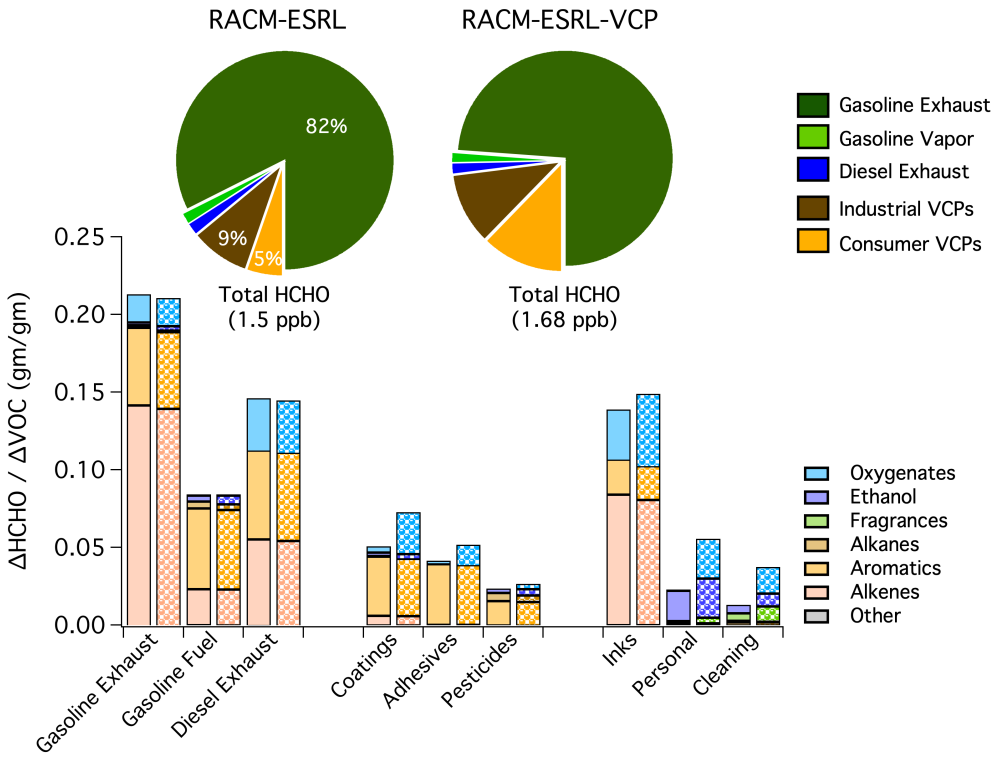

Fig. S37. Yield (bars) and total budget (pie charts) of formaldehyde formed from mobile source and VCP emissions. Solid bars show modeled formaldehyde yields calculated at the MDA8 ozone maximum using RACM-ESRL, while checkered bars show those using RACM-ESRL-VCP. Each bar is colored to show the fraction of formaldehyde resulting from different chemical classes. The pie charts show the fraction of formaldehyde modeled at the MDA8 ozone maximum that results from different emission sources. The numbers below each pie show the total formaldehyde formed from RACM-ESRL (left) and RACM-ESRL-VCP chemistry (right).

The change in chemistry between RACM-ESRL and RACM-ESRL-VCP has the biggest effect on formaldehyde yields from personal care and cleaning products. Both sectors are characterized by significant emissions of glycols and ethanol. When treated as alkanes in RACM_ESRL, these species do not yield significant formaldehyde (Table S9). When these species are represented in RACM-ESRL-VCP, formaldehyde yields from personal care and cleaning products increase by a factor > 2.

In RACM_ESRL, mobile sources dominate the budget of formaldehyde formed from AVOCs (~80%). When we employ RACM-ESRL-VCP, the distribution shifts to a higher contribution from VCPs, with the largest change associated with personal care and cleaning products. Total formaldehyde increases by ~15% (1.5 to 1.68 ppb) when shifting from RACM-ESRL to RACM-ESRL-VCP.

PAN yields from oxygenated VCPs increase by a factor > 2 when implementing RACM-ESRL-VCP (Fig S38). This increase is almost entirely due to the representation of alcohols with primary hydroxyl groups, such as ethanol, glycerol, propylene glycol, and ethylene glycol (Table S9). Mobile source VOCs have the largest yield owing to high alkene and alkyl aromatic content; however, when oVCPs are represented in RACM-ESRL-VCP, PAN yields from highly oxygenated sectors (e.g., personal care products) become as important as mobile sources.

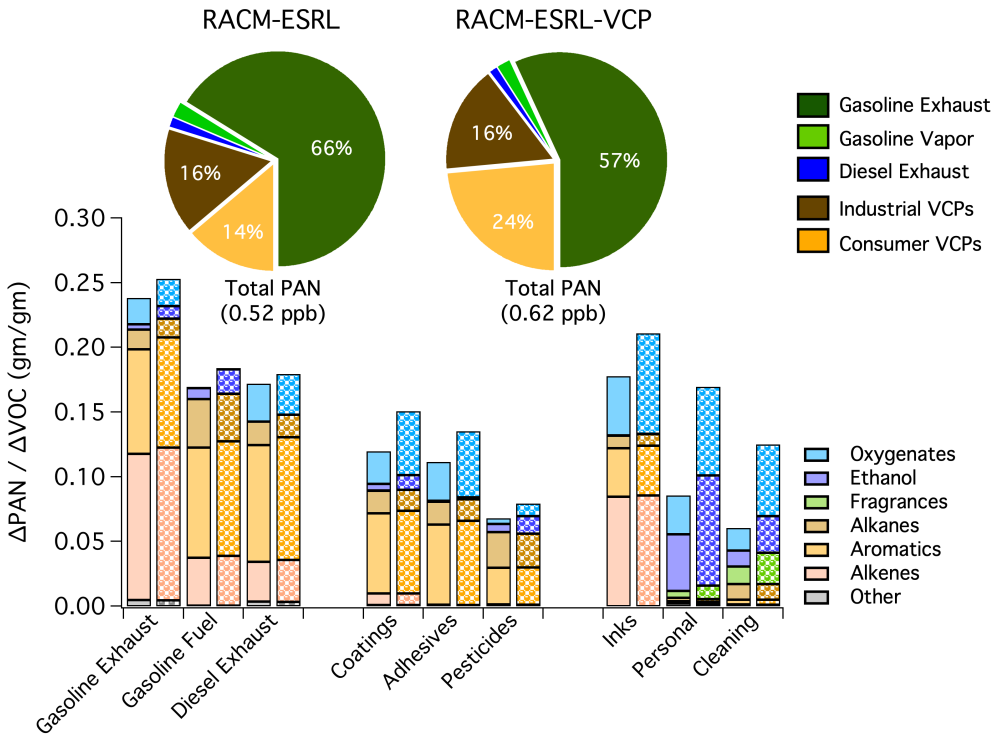

Fig. S38. Yield (bars) and total budget (pie charts) of PAN formed from mobile source and VCP emissions. Solid bars show modeled PAN yields calculated at the MDA8 ozone maximum using RACM-ESRL, while checkered bars show those using RACM-ESRL-VCP. Each bar is colored to show the fraction of PAN resulting from different chemical classes. The pie charts show the fraction of PAN modeled at the MDA8 ozone maximum that results from different emission sources. The numbers below each pie show the total PAN formed from RACM-ESRL (left) and RACM-ESRL-VCP chemistry (right).

With RACM_ESRL, total PAN production at the MDA8 ozone maximum is dominated by mobile sources (66%). In RACM-ESRL-VCP, total PAN is more evenly distributed between VCPs and mobile sources. At the MDA8 ozone maximum, PAN formed downwind of NYC increases by ~20% from 0.52 ppb in RACM-ESRL to 0.62 ppb in RACM-ESRL-VCP.

In contrast to formaldehyde and PAN, organic nitrates (ONIT) decrease by 40% when switching from RACM-ESRL to RACM-ESRL-VCP (Fig. S39). Glycol and glycol ethers are lumped to HC8, which mirrors the chemistry of octane and higher carbon alkanes. Upon OH oxidation in the presence of high NO_x mixing ratios, HC8 reacts to form ONIT at yields of ~30%. When represented in RACM-ESRL-VCP, oVCPs do not form organic nitrates, but instead follow pathways that lead to PAN formation.

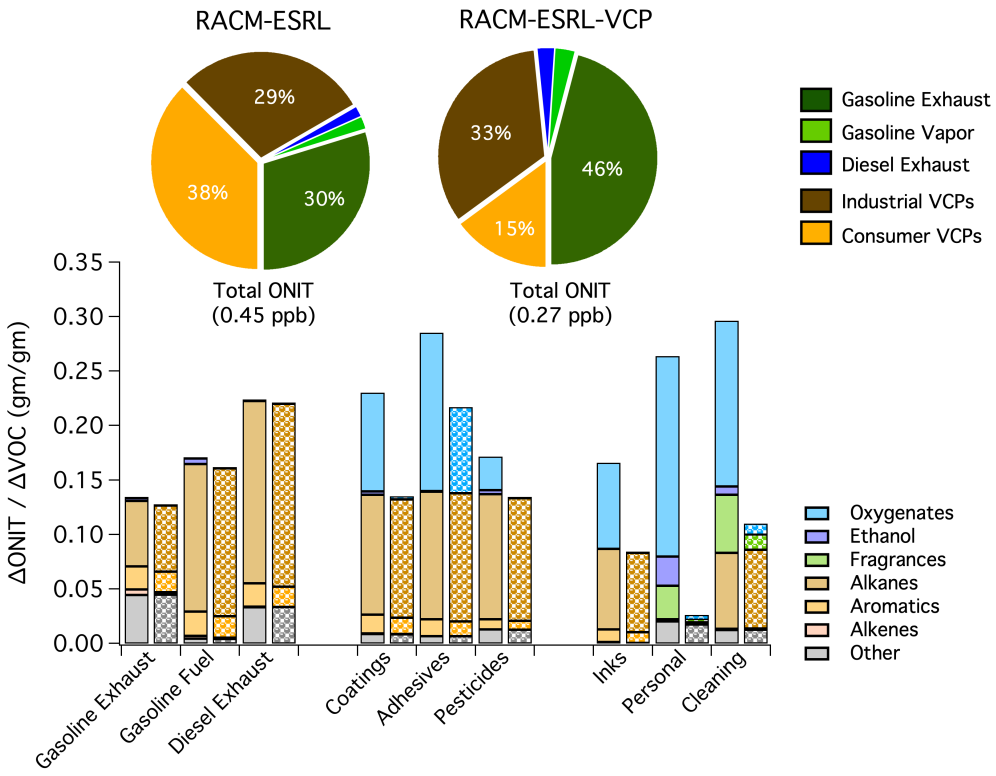

Fig. S39. Yield (bars) and total budget (pie charts) of organic nitrates (ONIT) formed from mobile source and VCP emissions. Solid bars show modeled ONIT yields calculated at the MDA8 ozone maximum using RACM-ESRL, while checkered bars show those using RACM-ESRL-VCP. Each bar is colored to show the fraction of ONIT resulting from different chemical classes. The pie charts show the fraction of ONIT modeled at the MDA8 ozone maximum that results from different emission sources. The numbers below each pie show the total ONIT formed from RACM-ESRL (left) and RACM-ESRL-VCP chemistry (right).

11.2 WRF-Chem

The box model results described in Section 11.1 show how the changes from RACM-ESRL to RACM-ESRL-VCP effect secondary product yields from AVOC emission sectors. In the following discussion, we show how AVOC emissions and oVCP chemistry impact the spatial distribution of ozone, formaldehyde and PAN modeled in WRF-Chem during the July 2, 2018 ozone event.

The surface ozone budget simulated in WRF-Chem is discussed in the main text (Fig. 3, panels A-D). Briefly, AVOCs from fossil fuel source and VCP emissions enhance photochemical ozone production in the NYC area. While the budget of ozone is largely influenced by the contributions from biogenic VOCs (Panel A), AVOC emissions are needed to explain the MDA8 ozone maximum observed downwind of Manhattan (Panels B and C). The production of ozone is largely insensitive to the chemical mechanism used to model urban ozone formation (i.e., RACM-ESRL or RACM-ESRL-VCP, Panel D). This is consistent with the modest changes in ozone yields and ozone distribution simulated using the box model (Fig S36).

Fig.3 shows analogous sensitivity cases for PAN (Panels E-H). We present PAN columns to complement previous studies that have evaluated PAN formation from satellite (119). Unlike ozone, regional mixing ratios of PAN resulting from the reaction of BVOCs + NO_x are low (panel

A). Furthermore, the emissions from VCPs (30% increase, panel C) tend to have a larger impact on PAN mixing ratios than from fossil fuels (20% increase, panel B), especially downwind of NYC.

The change from RACM-ESRL to RACM-ESRL-VCP markedly increases maximum PAN formation by ~20% (panel D). The higher formation of PAN is reflected by the substantial increase in PAN yields from alcohols, such as ethanol, when oVCPs are modeled using RACM-ESRL-VCP (Fig. S38). As discussed in Sections 10, the OH chemistry of primary alcohols, which ultimately leads to PAN formation via aldehyde oxidation, is misrepresented by the hydrocarbon chemistry described by RACM_ESRL. Consequently, the shift from RACM-ESRL to RACM-ESRL-VCP results in apparent contrasts in modeled PAN mixing ratios.

Figure S40 shows formaldehyde columns, which are important products from satellite remote sensing instruments that are used to infer VOC oxidation processes(116, 117). Each panel shows different sensitivity case, analogous to those presented in Fig. 3. Panels A-C show the impact of different VOC emission sectors on formaldehyde columns under the assumption of RACM-ESRL chemistry, while panel D shows the impact of exchanging chemical mechanisms from RACM-ESRL to RACM-ESRL-VCP.

Biogenic emissions dominate the formaldehyde budget on regional scales, and also result in a formaldehyde maximum downwind of NYC (panel A). This maximum is the approximate location of the ozone maximum shown in Fig. 3. When fossil fuel VOCs are included (panel B), formaldehyde columns increase by 7% over NYC, and 9% at the downwind maximum. The addition of VCP emissions increase formaldehyde over NYC and the downwind maximum by an additional 6 and 5%, respectively (panel C). When RACM-ESRL is exchanged for RACM-ESRL-VCP (oVCP chemistry, panel D), the change in formaldehyde is modest (< 3%).

Generally, fossil fuel emissions increase secondary formaldehyde to a greater extent than VCPs. This difference is largely attributed to the significantly higher yield of formaldehyde from tailpipe emissions of light alkenes, as shown in Fig. S37. The shift from RACM-ESRL to RACM-ESRL-VCP results in higher formaldehyde columns due to the increase in yield from oxygenates, such as ethanol. Despite this change, formaldehyde produced from gasoline remain 3-4 times greater than from VCPs (Fig. S37), and therefore the increase associated with oVCP chemistry is modest.

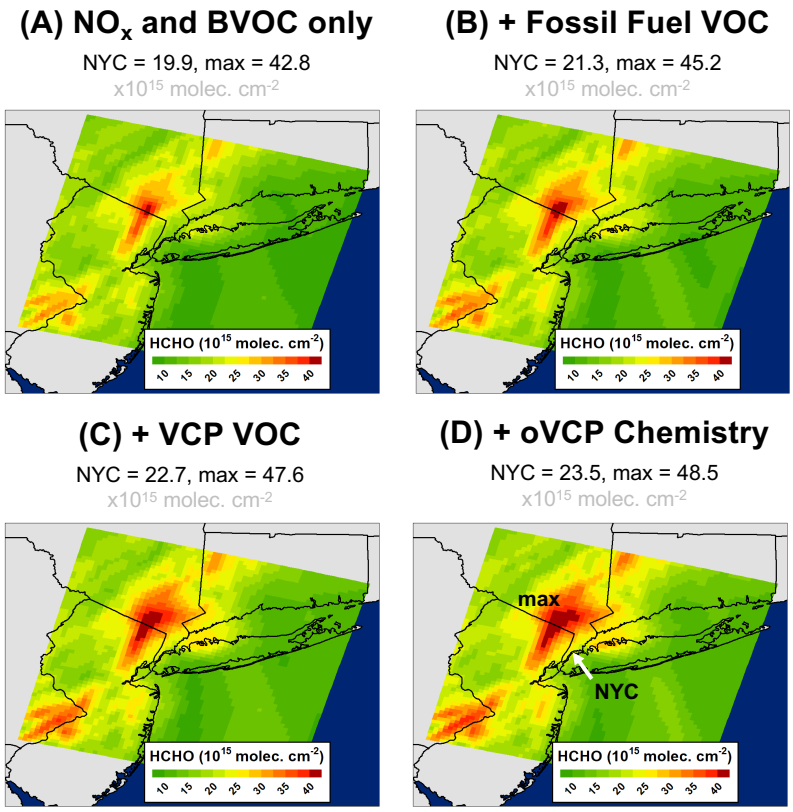

Fig. S40. WRF-Chem simulations of formaldehyde columns at 18:00 UTC. Shown are simulations for (A) regional background + formaldehyde produced from NO_x + BVOCs, (B) results from (A) with mobile source VOCs added, and (C) results from (B) with VOCs from VCPs added. Panels (A)-(C) show formaldehyde produced under the assumption of hydrocarbon chemistry (RACM_ESRL). Panel (D) shows the simulation using full emissions, but under the assumption of oVCP chemistry (RACM-ESRL-VCP).

12. Implications of oVCP chemistry on urban atmosphere chemistry

The PAN, ONIT, and formaldehyde distributions highlight the implications of oVCP chemistry on interpretations of urban ozone formation. Formaldehyde, which is measured by satellite, is used to assess ozone sensitivities to changes in NO_X and VOC chemical regimes(116, 117). However, as shown in Figures S37 and S40, secondary formaldehyde is dominated by the chemistry of isoprene, followed by light alkenes from gasoline. Consequently, interpretations of the ozone formation processes downwind of cities based on formaldehyde enhancements may be weighted towards hydrocarbon-rich sources, such as gasoline exhaust. This does not reflect the modeled distribution of ozone from AVOCs, which is more evenly distributed between mobile source and VCP emissions (Figures 3 and 4, main text).

In contrast, the distribution of PAN formed from the chemistry of AVOCs more closely mirrors the distribution of ozone from AVOC sources (Figures S36 and S38). When oVCPs are treated as hydrocarbons, PAN is dominated by mobile sources, and key oVCPs follow chemical pathways that misrepresent the chemistry of primary alcohols. With oVCP chemistry, PAN yields from oVCPs increase and lead to a distribution that is more evenly split between mobile sources and VCPs. Furthermore, Fig. S40 shows that oVCP emissions and chemistry strongly impact the spatial distribution of PAN, suggesting that PAN could be a useful diagnostic to constrain oVCP impacts on urban ozone formation. Measurements of PAN from satellite-borne infrared sounding

instruments are feasible(119) and such measurements, along with formaldehyde, may provide better constraints on AVOC impacts on ozone in regions where VCPs and traffic significantly contribute to urban emissions.

Figures S38 and S39 also demonstrate that when oVCP chemistry is prescribed, the modeled pool of reactive nitrogen (NO_y) shifts away from organic nitrate formation, which may represent a permanent sink of NO_x through deposition or aerosol partitioning(120), to PAN formation, which represents a transport mechanism of NO_x that can impact ozone formation on greater spatial and temporal scales(121). Depending on the direction, PAN transport from the urban region to rural / biogenic rich areas with high VOC reactivity serves to release NOx in regions where it can efficiently form more ozone, effectively extending scale over which the urban emissions produce ozone. Modeling of this effect is beyond the scope of this paper, but would be an important direction for additional modeling studies. To do so, air quality models should consider the impacts on oVCP emissions and chemistry on NO_y partitioning.

References

1. K. Sekimoto *et al.*, Calculation of the sensitivity of proton-transfer-reaction mass spectrometry (PTR-MS) for organic trace gases using molecular properties. *International Journal of Mass Spectrometry* **421**, 71-94 (2017).
2. B. M. Lerner *et al.*, An improved, automated whole air sampler and gas chromatography mass spectrometry analysis system for volatile organic compounds in the atmosphere. *Atmos. Meas. Tech.* **10**, 291-313 (2017).
3. A. Borbon *et al.*, Emission ratios of anthropogenic volatile organic compounds in northern mid-latitude megacities: Observations versus emission inventories in Los Angeles and Paris. *J. Geophys. Res. -Atmos.* **118**, 2041-2057 (2013).
4. B. C. McDonald, T. R. Dallmann, E. W. Martin, R. A. Harley, Long-term trends in nitrogen oxide emissions from motor vehicles at national, state, and air basin scales. *J. Geophys. Res.* **117** (2012).
5. B. C. McDonald, D. R. Gentner, A. H. Goldstein, R. A. Harley, Long-term trends in motor vehicle emissions in u.s. urban areas. *Environ. Sci. Technol.* **47**, 10022-10031 (2013).
6. B. C. McDonald *et al.*, Modeling Ozone in the Eastern U.S. using a Fuel-Based Mobile Source Emissions Inventory. *Environ. Sci. Technol.* **52**, 7360-7370 (2018).
7. FHWA (2018) Highway Statistics 2017, Table MF-2: Motor-Fuel Volume Taxed by States. (Office of Highway Policy Information, Federal Highway Administration, U.S. Department of Transportation, Washington, DC).
8. FHWA (2018) Highway Statistics 2017, Table MF-24: Non-highway use of gasoline. (Office of Highway Policy Information, Federal Highway Administration, U.S. Department of Transportation, Washington, DC).
9. EIA (2018) Fuel Oil and Kerosene Sales, 2017. (Energy Information Administration, U.S. Department of Energy, Washington, DC).
10. EIA (2018) Refined Motor Gasoline Sales. (Energy Information Administration, U.S. Department of Energy, Washington, DC).
11. EIA (2018) Refined Sales Volumes of Other Petroleum Products. (Energy Information Administration, U.S. Department of Energy, Washington, DC).

12. G. A. Bishop, M. J. Haugen, The Story of Ever Diminishing Vehicle Tailpipe Emissions as Observed in the Chicago, Illinois Area. *Environ. Sci. Technol.* **52**, 7587-7593 (2018).
13. G. A. Bishop, M. J. Haugen (2018) On-Road Remote Sensing of Automobile Emissions in the Denver Area: Winter 2017, Prepared for Coordinating Research Council, Inc. (Contract No. E-123). (Alpharetta, GA).
14. G. A. Bishop, D. H. Stedman (2016) On-Road Remote Sensing of Automobile Emissions in the Tulsa Area: Fall 2015, Prepared for Coordinating Research Council, Inc. (Contract No. E-106). (Alpharetta, GA).
15. M. J. Haugen, G. A. Bishop, A. Thiruvengadam, D. K. Carder, Evaluation of Heavy- and Medium-Duty On-Road Vehicle Emissions in California's South Coast Air Basin. *Environ Sci Technol* **52**, 13298-13305 (2018).
16. M. J. Haugen, G. A. Bishop, Long-Term Fuel-Specific NO x and Particle Emission Trends for In-Use Heavy-Duty Vehicles in California. *Environ. Sci. Technol.* **52**, 6070-6076 (2018).
17. EPA (2015) MOVES2014a (Motor Vehicle Emission Simulator). (Office of Transportation and Air Quality, U.S. Environmental Protection Agency).
18. B. C. McDonald, A. H. Goldstein, R. A. Harley, Long-term trends in California mobile source emissions and ambient concentrations of black carbon and organic aerosol. *Environ. Sci. Technol.* **49**, 5178-5188 (2015).
19. T. D. Gordon *et al.*, Primary gas- and particle-phase emissions and secondary organic aerosol production from gasoline and diesel off-road engines. *Environ. Sci. Technol.* **47**, 14137-14146 (2013).
20. J. Volckens, J. Braddock, R. F. Snow, W. Crews, Emissions profile from new and in-use handheld, 2-stroke engines. *Atmos. Environ.* **41**, 640-649 (2007).
21. D. A. Burgard, C. R. Bria, J. A. Berenbeim, Remote sensing of emissions from in-use small engine marine vessels. *Environ. Sci. Technol.* **45**, 2894-2901 (2011).
22. EPA (2010) NONROAD2008a Model. (Office of Transportation and Air Quality, U.S. Environmental Protection Agency).
23. EPA (2017) National Emissions Inventory (NEI) 2014, version 2. (Office of Air Quality Planning and Standards, U.S. Environmental Protection Agency, Research Triangle Park, N.C.).
24. J. I. Rubin, A. J. Kean, R. A. Harley, D. B. Millet, A. H. Goldstein, Temperature dependence of volatile organic compound evaporative emissions from motor vehicles. *J. Geophs. Res.* **111**, 1-7 (2006).
25. D. R. Gentner, R. A. Harley, A. M. Miller, A. H. Goldstein, Diurnal and seasonal variability of gasoline-related volatile organic compound emissions in Riverside, California. *Environ. Sci. Technol.* **43**, 4247-4252 (2009).
26. W. R. Pierson *et al.*, Assessment of Nontailpipe Hydrocarbon Emissions from Motor Vehicles. *J. Air Waste Manag. Assoc.* **49**, 498-519 (1999).
27. J. Yanowitz, M. S. Graboski, L. B. A. Ryan, T. L. Alleman, R. L. McCormick, Chassis Dynamometer Study of Emissions from 21 In-Use Heavy-Duty Diesel Vehicles. *Environ. Sci. Technol.* **33**, 209-216 (1999).
28. B. C. McDonald *et al.*, Volatile chemical products emerging as largest petrochemical source of urban organic emissions. *Science* **359**, 760-764 (2018).

29. DEC (2011) Official Compilation of Codes, Rules, and Regulations of the State of New York (Title 6, Chapter 3, Subchapter A, Part 205): Architectural and Industrial Maintenance (AIM) Coatings. (Department of Environmental Conservation, Albany, NY).
30. M. M. Coggon *et al.*, Diurnal Variability and Emission Pattern of Decamethylcyclopentasiloxane (D5) from the Application of Personal Care Products in Two North American Cities. *Environ. Sci. Technol.* **52**, 5610-5618 (2018).
31. AQMD (2016) Rule 1113 - Architectural Coatings. (South Coast Air Quality Managment District).
32. DEC (2013) Official Compilation of Codes, Rules, and Regulations of the State of New York (Title 6, Chapter 3, Subchapter A, Part 228): Surface Coating Processes, Commercial and Industrial Adhesives, Sealants and Primers. (Department of Environmental Conservation, Albany, NY).
33. G. Plant *et al.*, Large Fugitive Methane Emissions From Urban Centers Along the U.S. East Coast. *Geophys. Res. Lett.* **46**, 8500-8507 (2019).
34. D. R. Gentner *et al.*, Chemical composition of gas-phase organic carbon emissions from motor vehicles and implications for ozone production. *Environ. Sci. Technol.* **47**, 11837-11848 (2013).
35. CARB (2019) 2013-2015 Consumer and Commercial Products Survey. (California Air Resources Board, Sacramento, CA).
36. CARB (2018) 2014 Architectural Coatins Survey. (California Air Resources Board, Sacramento, CA).
37. U. S. EPA (2014) SPECIATE (version 4.4). (U.S. Environmental Protection Agency).
38. J. C. Schroder *et al.*, Sources and Secondary Production of Organic Aerosols in the Northeastern United States during WINTER. *J Geophys Res-Atmos*, 7771– 7796 (2018).
39. Z. Jiang *et al.*, Unexpected slowdown of US pollutant emission reduction in the past decade. *Proc. Natl. Acad. Sci. U.S.A.* **115**, 5099-5104 (2018).
40. J. Peischl *et al.*, Quantifying Methane and Ethane Emissions to the Atmosphere From Central and Western U.S. Oil and Natural Gas Production Regions. *J Geophys Res-Atmos* 10.1029/2018jd028622, 7725– 7740 (2018).
41. J. Peischl *et al.*, Quantifying atmospheric methane emissions from oil and natural gas production in the Bakken shale region of North Dakota. *J Geophys Res-Atmos* **121**, 6101-6111 (2016).
42. J. Peischl *et al.*, Quantifying atmospheric methane emissions from the Haynesville, Fayetteville, and northeastern Marcellus shale gas production regions. *J Geophys Res-Atmos* **120**, 2119-2139 (2015).
43. O. E. Salmon *et al.*, Top-Down Estimates of NOx and CO Emissions From Washington, D.C.-Baltimore During the WINTER Campaign. *J Geophys Res-Atmos* 10.1029/2018jd028539, 7705– 7724 (2018).
44. A. F. Stein *et al.*, NOAA's HYSPLIT Atmospheric Transport and Dispersion Modeling System. *B. Am. Meteorol. Soc.* **96**, 2059-2077 (2015).
45. G. A. Grell *et al.*, Fully coupled "online" chemistry within the WRF model. *Atmos. Environ.* **39**, 6957-6975 (2005).

46. S. W. Kim *et al.*, NO2 columns in the western United States observed from space and simulated by a regional chemistry model and their implications for NOx emissions. *J. Geophys. Res.* **114** (2009).
47. A. Guenther *et al.*, Estimates of global terrestrial isoprene emissions using MEGAN (Model of Emissions of Gases and Aerosols from Nature). *Atmos Chem Phys* **6**, 3181-3210 (2006).
48. J. Calvert, A. Mellouki, J. Orlando, M. Pilling, T. Wallington, *Mechanisms of Atmospheric Oxidation of the Oxygenates* (Oxford University Press, 2011), pp. 1619.
49. W. S. Goliff, W. R. Stockwell, C. V. Lawson, The regional atmospheric chemistry mechanism, version 2. *Atmospheric Environment* **68**, 174-185 (2013).
50. J. B. Burkholder *et al.* (2019) Chemical Kinetics and Photochemical Data for Use in Atmospheric Studies, Evaluation No. 19. (Jet Propulsion Laboratory, Pasadena, CA).
51. B. Aumont, S. Szopa, S. Madronich, Modelling the evolution of organic carbon during its gas-phase tropospheric oxidation: development of an explicit model based on a self generating approach. *Atmos Chem Phys* **5**, 2497-2517 (2005).
52. S. M. Saunders, M. E. Jenkin, R. G. Derwent, M. J. Pilling, Protocol for the development of the Master Chemical Mechanism, MCM v3 (Part A): tropospheric degradation of non-aromatic volatile organic compounds. *Atmos Chem Phys* **3**, 161-180 (2003).
53. R. Atkinson, J. Arey, Atmospheric degradation of volatile organic compounds. *Chem. Rev.* **103**, 4605-4638 (2003).
54. R. Atkinson, Kinetics of the gas-phase reactions of a series of organosilicon compounds with hydroxyl and nitrate(NO3) radicals and ozone at 297 .+-. 2 K. *Environ. Sci. Technol.* **25**, 863-866 (1991).
55. C.-M. Gan, Y. Wu, B. L. Madhavan, B. Gross, F. Moshary, Application of active optical sensors to probe the vertical structure of the urban boundary layer and assess anomalies in air quality model PM2.5 forecasts. *Atmos. Environ.* **45**, 6613-6621 (2011).
56. I. M. Brooks, Finding boundary layer top: Application of a wavelet covariance transform to lidar backscatter profiles. *J Atmos Ocean Tech* **20**, 1092-1105 (2003).
57. J. Herman *et al.*, NO2column amounts from ground-based Pandora and MFDOAS spectrometers using the direct-sun DOAS technique: Intercomparisons and application to OMI validation. *J. Geophs. Res.* **114** (2009).
58. L. N. Lamsal *et al.*, High-resolution NO2 observations from the Airborne Compact Atmospheric Mapper: Retrieval and validation. *J Geophys Res-Atmos* **122**, 1953-1970 (2017).
59. L. N. Lamsal *et al.*, Evaluation of OMI operational standard NO2 column retrievals using in situ and surface-based NO2 observations. *Atmos Chem Phys* **14**, 11587-11609 (2014).
60. C. R. Nowlan *et al.*, Nitrogen dioxide observations from the Geostationary Trace gas and Aerosol Sensor Optimization (GeoTASO) airborne instrument: Retrieval algorithm and measurements during DISCOVER-AQ Texas 2013. *Atmos. Meas. Tech.* **9**, 2647-2668 (2016).
61. R. J. Dirksen *et al.*, Evaluation of stratospheric NO2retrieved from the Ozone Monitoring Instrument: Intercomparison, diurnal cycle, and trending. *J. Geophs. Res.* **116**, 1-22 (2011).

62. W. L. Chameides, R. W. Lindsay, J. Richardson, C. S. Kiang, The role of biogenic hydrocarbons in urban photochemical smog: Atlanta as a case-study. *Science* **241**, 1473-1475 (1988).
63. M. Trainer *et al.*, Models and observations of the impact of natural hydrocarbons on rural ozone. *Nature* **392**, 705-707 (1987).
64. A. G. Carlton, K. R. Baker, Photochemical modeling of the Ozark isoprene volcano: MEGAN, BEIS, and their impacts on air quality predictions. *Environ. Sci. Technol.* **45**, 4438-4445 (2011).
65. C. Warneke *et al.*, Biogenic emission measurement and inventories determination of biogenic emissions in the eastern United States and Texas and comparison with biogenic emission inventories. *J. Geophys. Res.* **115**, 1-21 (2010).
66. R. De Young *et al.*, Langley mobile ozone lidar: ozone and aerosol atmospheric profiling for air quality research. *Appl. Opt.* **56**, 721-730 (2017).
67. G. Gronoff *et al.*, A method for quantifying near range point source induced O3 titration events using Co-located Lidar and Pandora measurements. *Atmos. Environ.* **204**, 43-52 (2019).
68. B. M. Farris *et al.*, Demonstration of an off-axis parabolic receiver for near-range retrieval of lidar ozone profiles. *Atmos. Meas. Tech.* **12**, 363-370 (2019).
69. E. V. Browell, S. Ismail, S. T. Shipley, Ultraviolet DIAL measurements of O3 profiles in regions of spatially inhomogeneous aerosols. *Appl. Opt.* **24**, 2827-2836 (1985).
70. T. Leblanc *et al.*, Proposed standardized definitions for vertical resolution and uncertainty in the NDACC lidar ozone and temperature algorithms – Part 2: Ozone DIAL uncertainty budget. *Atmos. Meas. Tech.* **9**, 4051-4078 (2016).
71. T. Leblanc *et al.*, Validation of the TOLNet lidars: the Southern California Ozone Observation Project (SCOOP). *Atmos. Meas. Tech.* **11**, 6137-6162 (2018).
72. Y. C. Lin *et al.*, Summertime formaldehyde observations in New York City: Ambient levels, sources and its contribution to HOx radicals. *J. Geophs. Res.* **117**, 1-14 (2012).
73. S. C. Herndon *et al.*, Airborne measurements of HCHO and HCOOH during the New England Air Quality Study 2004 using a pulsed quantum cascade laser spectrometer. *J. Geophys. Res.* **112**, 1-15 (2007).
74. I. E. Gordon *et al.*, The HITRAN2016 molecular spectroscopic database. *J. Quant. Spectrosc. Ra.* **203**, 3-69 (2017).
75. P. Werle, R. Mucke, F. Slemr, The Limits of Signal Averaging in Atmospheric Trace-Gas Monitoring by Tunable Diode-Laser Absorption-Spectroscopy (Tdlas). *Appl Phys B-Photo* **57**, 131-139 (1993).
76. X. Ren *et al.*, Methane Emissions From the Baltimore-Washington Area Based on Airborne Observations: Comparison to Emissions Inventories. *Journal of Geophysical Research: Atmospheres* **123**, 8869-8882 (2018).
77. J. Zhang *et al.*, Mobile Laboratory Measurements of High Surface Ozone Levels and Spatial Heterogeneity During LISTOS 2018: Evidence for Sea Breeze Influence. *Journal of Geophysical Research: Atmospheres* **125**, 1-12 (2020).
78. W. M. Angevine *et al.*, Coastal Boundary Layer Influence on Pollutant Transport in New England. *Journal of Applied Meteorology* **43**, 1425-1437 (2004).

79. S. H. Lee *et al.*, Modeling ozone plumes observed downwind of New York City over the North Atlantic Ocean during the ICARTT field campaign. *Atmospheric Chemistry and Physics* **11**, 7375-7397 (2011).
80. K. Zhao *et al.*, Variation of Ozone and PBL from the Lidar Observations and WRF-Chem Model in NYC Area During the 2018 Summer LISTOS Campaign. *EPJ Web of Conferences* **237** (2020).
81. G. M. Wolfe, M. R. Marvin, S. J. Roberts, K. R. Travis, J. Liao, The Framework for 0-D Atmospheric Modeling (F0AM) v3.1. *Geosci. Model Dev.* **9**, 3309-3319 (2016).
82. M. B. Dillon, M. S. Lamanna, G. W. Schade, A. H. Goldstein, R. C. Cohen, Chemical evolution of the Sacramento urban plume: Transport and oxidation. *J. Geophys. Res.* **107**, 1-15 (2002).
83. C. A. Cardelino, W. L. Chameides, Natural Hydrocarbons, Urbanization, and Urban Ozone. *J. Geophs. Res.* **95**, 13971-13979 (1990).
84. A. C. Steinemann *et al.*, Fragranced consumer products: Chemicals emitted, ingredients unlisted. *Environ. Impact. Asses.* **31**, 328-333 (2011).
85. A. Steinemann, Volatile emissions from common consumer products. *Air Qual. Atmos. Hlth.* **8**, 273-281 (2015).
86. S. K. Brown, M. R. Sim, M. J. Abramson, C. N. Gray, Concentrations of Volatile Organic Compounds in Indoor Air - A Review *Indoor Air* **4**, 123-134 (1994).
87. A. T. Hodgson, H. Levin (1993) Volatile Organic Compounds in Indoor Air: A Review of Concentrations Measured in North America Since 1990 (Lawrence Berkeley National Laboratory).
88. J. M. Logue, T. E. McKone, M. H. Sherman, B. C. Singer, Hazard assessment of chemical air contaminants measured in residences. *Indoor Air* **21**, 92-109 (2011).
89. C. Geron, R. Rasmussen, R. R. Arnts, A. Guenther, A review and synthesis of monoterpene speciation from forests in the United States. *Atmos. Environ.* **34**, 1761-1781 (2000).
90. G. I. Gkatzelis *et al.*, Identifying Volatile Chemical Product Tracer Compounds in U.S. Cities. *Environmental Science & Technology* **55**, 188-199 (2020).
91. M. W. Alton, E. C. Browne, Atmospheric Chemistry of Volatile Methyl Siloxanes: Kinetics and Products of Oxidation by OH Radicals and Cl Atoms. *Environ Sci Technol* **54**, 5992-5999 (2020).
92. M. S. McLachlan *et al.*, Concentrations and fate of decamethylcyclopentasiloxane (D(5)) in the atmosphere. *Environ Sci Technol* **44**, 5365-5370 (2010).
93. B. C. Singer, H. Destaillats, A. T. Hodgson, W. W. Nazaroff, Cleaning products and air fresheners: emissions and resulting concentrations of glycol ethers and terpenoids. *Indoor Air* **16**, 179-191 (2006).
94. CARB (2018) 2016 Fragrance Formulator Survey. (California Air Resources Board).
95. J. T. Scanlon, D. E. Willis, Calculation of Flame Ionization Detector Relative Response Factors Using the Effective Carbon Number Concept. *J. Chrom. Sci.* **23**, 333-340 (1985).
96. G. Isaacman-VanWertz *et al.*, Automated single-ion peak fitting as an efficient approach for analyzing complex chromatographic data. *J. Chromatogr. A.* **1529**, 81-92 (2017).

97. A. R. Koss *et al.*, Non-methane organic gas emissions from biomass burning: identification, quantification, and emission factors from PTR-ToF during the FIREX 2016 laboratory experiment. *Atmos Chem Phys* **18**, 3299-3319 (2018).
98. M. M. Coggon *et al.*, Emissions of nitrogen-containing organic compounds from the burning of herbaceous and arboraceous biomass: Fuel composition dependence and the variability of commonly used nitrile tracers. *Geophys. Res. Lett.* **43**, 9903-9912 (2016).
99. B. C. Singer, W. W. Delp, D. R. Black, H. Destaillats, I. S. Walker (2016) Reducing In-Home Exposure to Air Pollution. Final Report to California Air Resources Board for Contract 11-311. (Sacramento, CA).
100. N. Yamamoto, D. G. Shendell, A. M. Winer, J. Zhang, Residential air exchange rates in three major US metropolitan areas: results from the Relationship Among Indoor, Outdoor, and Personal Air Study 1999-2001. *Indoor Air* **20**, 85-90 (2010).
101. J. A. de Gouw *et al.*, Increasing atmospheric burden of ethanol in the United States. *Geophys. Res. Lett.* **39**, 1-6 (2012).
102. H. B. Singh, L. J. Salas, B. K. Cantrell, R. M. Redmond, Distribution of aromatic hydrocarbons in the ambient air. *Atmos. Environ.* **19**, 1911-1919 (1985).
103. L. M. Bettencourt, J. Lobo, D. Helbing, C. Kuhnert, G. B. West, Growth, innovation, scaling, and the pace of life in cities. *Proc. Natl. Acad. Sci. U.S.A.* **104**, 7301-7306 (2007).
104. C. K. Gately, L. R. Hutyra, I. Sue Wing, Cities, traffic, and CO2: A multidecadal assessment of trends, drivers, and scaling relationships. *Proc. Natl. Acad. Sci. U.S.A.* **112**, 4999-5004 (2015).
105. L. N. Lamsal, R. V. Martin, D. D. Parrish, N. A. Krotkov, Scaling relationship for NO2 pollution and urban population size: a satellite perspective. *Environ. Sci. Technol.* **47**, 7855-7861 (2013).
106. S. M. Aschmann, R. Atkinson, Kinetics of the gas-phase reactions of the OH radical with selected glycol ethers, glycols, and alcohols. *Int J Chem Kinet* **30**, 533-540 (1998).
107. S. M. Aschmann, P. Martin, E. C. Tuazon, J. Arey, R. Atkinson, Kinetic and product studies of the reactions of selected glycol ethers with OH radicals. *Environ Sci Technol* **35**, 4080-4088 (2001).
108. H. L. Bethel, R. Atkinson, J. Arey, Kinetics and products of the reactions of selected diols with the OH radical. *International Journal of Chemical Kinetics* **33**, 310-316 (2001).
109. H. L. Bethel, R. Atkinson, J. Arey, Hydroxycarbonyl Products of the Reactions of Selected Diols with the OH Radical. *The Journal of Physical Chemistry A* **107**, 6200-6205 (2003).
110. H. Choi, N. Schmidbauer, J. Spengler, C. G. Bornehag, Sources of propylene glycol and glycol ethers in air at home. *Int J Environ Res Public Health* **7**, 4213-4237 (2010).
111. A. T. Hodgson, A. F. Rudd, D. Beal, S. Chandra, Volatile organic compound concentrations and emission rates in new manufactured and site-built houses. *Indoor Air* **10**, 178-192 (2000).
112. J. Zhu, Y. L. Feng, B. Aikawa, A positive chemical ionization GC/MS method for the determination of airborne ethylene glycol and propylene glycols in non-occupational environments. *J Environ Monit* **6**, 881-887 (2004).
113. B. N. Duncan *et al.*, Satellite data of atmospheric pollution for U.S. air quality applications: Examples of applications, summary of data end-user resources, answers to FAQs, and common mistakes to avoid. *Atmospheric Environment* **94**, 647-662 (2014).

114. G. M. Wolfe *et al.*, Mapping hydroxyl variability throughout the global remote troposphere via synthesis of airborne and satellite formaldehyde observations. *Proc Natl Acad Sci U S A* **116**, 13144 (2019).
115. G. K. Yeh, P. J. Ziemann, Alkyl nitrate formation from the reactions of C8-C14 n-alkanes with OH radicals in the presence of NO(x): measured yields with essential corrections for gas-wall partitioning. *J Phys Chem A* **118**, 8147-8157 (2014).
116. B. N. Duncan *et al.*, Application of OMI observations to a space-based indicator of NOx and VOC controls on surface ozone formation. *Atmospheric Environment* **44**, 2213-2223 (2010).
117. X. Jin, A. Fiore, K. F. Boersma, I. Smedt, L. Valin, Inferring Changes in Summertime Surface Ozone-NOx-VOC Chemistry over U.S. Urban Areas from Two Decades of Satellite and Ground-Based Observations. *Environ Sci Technol* **54**, 6518-6529 (2020).
118. W. Carter, Updated Maximum Incremental Reactivity Scale and Hydrocarbon Bin Reactivities for Regulatory Applications. *California Air Resources Board Contract 07-339* (2010).
119. V. H. Payne *et al.*, Spatial variability in tropospheric peroxyacetyl nitrate in the tropics from infrared satellite observations in 2005 and 2006. *Atmospheric Chemistry and Physics* **17**, 6341-6351 (2017).
120. J. A. Fisher *et al.*, Organic nitrate chemistry and its implications for nitrogen budgets in an isoprene- and monoterpene-rich atmosphere: constraints from aircraft (SEAC(4)RS) and ground-based (SOAS) observations in the Southeast US. *Atmos Chem Phys* **16**, 5969-5991 (2016).
121. E. V. Fischer *et al.*, Atmospheric peroxyacetyl nitrate (PAN): a global budget and source attribution. *Atmospheric Chemistry and Physics* **14**, 2679-2698 (2014).